

Advanced Silicon Solar Cell Device Physics and Design

Thesis by
Michael Gardner Deceglie

In Partial Fulfillment of the Requirements
for the Degree of
Doctor of Philosophy



California Institute of Technology
Pasadena, California

2013

(Defended February 11, 2013)

© 2013

Michael Gardner Deceglie

All Rights Reserved

To my parents,
for their unwavering support and encouragement

Acknowledgements

Reflecting on my time at Caltech, I feel an overwhelming sense of gratitude for the opportunity to work with such exceptionally talented and dedicated people. The people I have worked and interacted with during my time here have been absolutely essential to the work described in this thesis. The material and intellectual contributions of those I have worked with are so numerous it would be impossible to list them all here; please know that I am deeply grateful.

I must begin by thanking my advisor, Professor Harry Atwater. His enthusiasm and support has been instrumental in my growth as a researcher. He has been incredibly supportive not just of my growth as a scientist, but also of my professional growth, making sure that I met the right people and had chances to present my work publicly to influential audiences. I am also grateful for the balance of freedom and guidance Harry has given me during my time here. When I pitched new ideas to him, he never hesitated to support and encourage me. In fact, of all my accomplishments in my time here, I am most proud of the ability I have developed, with Harry's guidance and enthusiastic support, to identify and pursue opportunities for substantive and novel contributions to science and engineering.

I also thank the other members of my candidacy and thesis committees: Professors Oskar Painter, Nate Lewis, Andrei Faraon, and Brent Fultz, for their guidance and feedback on my work.

I am fortunate to have had the opportunity to work with the members of the Atwater and Lewis groups. To interact on a daily basis with an interdisciplinary group of such brilliant individuals has been an amazing experience. The expertise and creativity of these two groups has been instrumental to my work. Those I am particularly thankful to include Shane Ardo, Melissa Archer, Anna Beck, Matthew Bierman, Shannon Boettcher, Jeff Bosco, Ryan Briggs, Ana Brown, Stanley Burgos, Chris Chen, Rob Coridan, Naomi Coronel, Davis Darvish, Prof. Jennifer Dionne, Carissa Eisler, Matthew Escarra, Jim Fakonas, Prof. Michael Filler, Cristofer Flowers, Ron Grimm, Carrie Hofmann, Min Jang, Seokmin Jeon, Brendan Kayes, Seyoon Kim, Greg Kimball, Lise Lahourcade, Prof. Jiun-Haw Lee, Andrew Leenheer, Marina Leite, John Loyd, Gerald Miller, Prof. Jeremy Munday, Prof. Deirdre O'Carroll, Leslie O'Leary, Ragip Pala, Andrey Poletayev, Imogen Pryce, Bryce Sadtler, Elizabeth Santori, Matthew Shaner, Amanda Shing, Pierpaolo Spinelli, Josh Spurgeon, Prof. Nick Strandwitz, Luke Sweatlock, Faisal Tajdar, Emily Warmann, Kelsey Whitesell, and Samantha Wilson. To everyone who has helped me polish a presentation, trained me on equipment, helped me fix a vacuum pump, talked through a challenge with me, and everything in between, I am grateful. Softball was fun too.

I am particularly grateful to the officemates I have had during my time here. Matthew Dicken, Morgan Putnam, Kenneth Diest, Adele Tamboli, Dennis Callahan, Emily Kosten, Arian Kriesch, Matthew Sheldon, and Victor Brar. Watson 252 has been a stimulating and productive place to work. Thank you for the friendship, keeping things fun, and for all the science we talked.

A number of people have contributed directly to the work described here. Krista

Langeland was instrumental in helping me get my research started and she contributed prior work on the HWCVD of Si solar cells described in Chapter 2. I am also grateful for her mentorship as I learned how to battle the CVD cluster tool. Michael Kelzenberg's numerous contributions to the capabilities of the Atwater group will be felt for many years to come. I thank him for designing and building much of the instrumentation used to carry out J-V and LBIC measurements. He also wrote the code connecting optical and electrical simulations which enabled the work described in Chapter 4. Daniel Turner-Evans has also been a great help with solving technical and scientific challenges associated with the numerous simulations in this thesis. Hal Emmer has worked closely with me on the work described in Chapter 3; I thank him both for his technical contributions to instrumentation and sample fabrication and for his intellectual and scientific contributions to the project. Vivian Ferry was absolutely indispensable to the work described in Chapter 4. I thank her for the optical modeling she carried out and for all the technical and scientific insights she contributed to that work. I thank Jonathan Grandidier, Raymond Weitekamp, Colton Bukowski, and Corsin Battaglia for collaborating on light trapping in solar cells with nanospheres (Section 4.3). I am also grateful to the talented undergraduates who worked with me on templates for HWCVD growth, Clare Chen and Arianne Collopy.

I am grateful for the fruitful collaborations I have had with researchers at other institutions. I thank Zak Holman, Antoine Descoeur, Stefaan De Wolf, and Christoph Bailiff at École Polytechnique Fédérale de Lausanne for contributing their expertise in the science, fabrication, and operation of silicon heterojunction (SHJ) cells. They deposited the junctions studied experimentally in Chapter 3, and through numerous conversations, contributed to the scientific concepts described therein. I am also grateful for the collaboration I had with Sachit Grover, David Young, and Pauls Stradins at the National Renewable Energy Laboratory on the device physics of SHJ-based film Si photovoltaics. Our collaborative work is described in Section 3.4, and our insightful conversations helped shape my thinking about much of the work described in Chapter 3.

I would also like to thank those outside our group at Caltech who have supported this work. I am grateful to Professor George Rossman for the use of the Raman spectrometer in his lab, and Elizabeth Miura Boyd for her help in operating the instrument. I thank Ali Ghaffari for overseeing the shared applied physics facilities, and in particular the Watson SEM which I used heavily throughout my research. I thank Carol Garland for her help and guidance with transmission electron microscopy measurements and sample preparation. I am grateful to the entire technical staff in the Kalvi Nanoscience Institute, in particular Bophan Chhim and Melissa Melendes, for their help in training and keeping the cleanroom equipment running smoothly. I would like to thank Mike Roy and Steve Olson of the Instrument Shop for their help in designing, fabricating, and repairing numerous components.

My successful navigation of the graduate program here would not have been possible without the support of exceptional administrative staff. In the Atwater group, April Neidholdt, Lyra Haas, Jennifer Blankenship, and Tiffany Kimoto, have enriched my experience, not only by making sure everything runs smoothly and organizing our group retreats and events, but also for helping to make the Atwater

group a friendly and enjoyable place to work. I also thank the Applied Physics department administrative staff for their help; in particular, I thank Christy Jenstad, for the key role she played in ensuring that the logistics of my thesis submission and defense went smoothly.

I would not have had the opportunity to carry out the research described in this thesis without first completing a year and half of coursework. I thank Lisa Mauger for her friendship and work put in together on our problem sets.

My experience outside of the classroom and lab has been rich and filled with good friends. I am extremely grateful for the friendships I have made here. To my friends, thank you for all the great times: concerts, hikes, surf sessions, ski trips, and just time spent hanging out together. I am also deeply grateful to my family for helping to nurture my interest in the natural sciences and problem solving and for helping me navigate life with all of their love, support, and encouragement through the years. Finally, to Emily Warren, thank you for all your love and support, you are an amazing collaborator in both science and in life.

Michael G. Deceglie

February 2013

Pasadena, CA

Abstract

A fundamental challenge in the development and deployment of solar photovoltaic technology is a reduction in cost enabling direct competition with fossil-fuel-based energy sources. A key driver in this cost reduction is optimized device efficiency, because increased energy output leverages all photovoltaic system costs, from raw materials and module manufacturing to installation and maintenance. To continue progress toward higher conversion efficiencies, solar cells are being fabricated with increasingly complex designs, including engineered nanostructures, heterojunctions, and novel contacting and passivation schemes. Such advanced designs require a comprehensive and unified understanding of the optical and electrical device physics at the microscopic scale.

This thesis establishes a microscopic understanding of solar cell optoelectronic performance and its impact on cell optimization. We consider this in three solar cell platforms: thin-film crystalline silicon, amorphous/crystalline silicon heterojunctions, and thin-film cells with nanophotonic light trapping. For thin-film crystalline silicon, we discuss experimental investigations of devices based on a crystalline silicon absorber layer grown with low-temperature hot-wire chemical vapor deposition. Such a low-temperature process enables the use of large-grain crystal material on inexpensive substrates. In addition, we discuss device physics simulations describing the impact of grain boundaries in such devices.

We also consider a solar cell design based on a p/n heterojunction between crystalline Si (c-Si) and wider band-gap hydrogenated amorphous silicon (a-Si:H). These devices obtain high photovoltages due to excellent passivation of the c-Si surface by a-Si:H. They are also known to be extremely sensitive to imperfections in the interface between the a-Si:H and the c-Si. We describe simulations and experiments that show this sensitivity is due in part to lateral transport of photo-excited carriers near the heterointerface. These results provide an improved understanding of the device physics in these devices and will aid in the development of advanced designs, including all back-contacted heterojunction structures and the use of novel passivation

layers.

Finally, we describe a simulation-based method for simultaneously optimizing the optical and electrical properties of thin-film solar cells featuring nanophotonic light-trapping structures. A key challenge in the optimization of such light-trapping structures is to account for the interdependent optical and electrical properties of solar cells, including variations in material quality. We address this challenge with multidimensional optoelectronic simulations that fully account for the optical and electrical properties of the devices including the effects of imperfect carrier collection. We demonstrate that light-trapping structures can be designed to reduce the fraction of light parasitically absorbed within the device and measurably increase the internal quantum efficiency of charge collection. Our results highlight the full potential of engineered nanophotonic light trapping, and represent a new optimization paradigm in which optical design can be leveraged to benefit the electrical properties of solar cells.

Contents

List of Figures	xv
List of Tables	xix
List of Publications	xxi
1 Introduction	1
1.1 Introduction	1
1.2 Solar cell basics	2
1.2.1 Operation	2
1.2.2 Performance parameters	4
1.3 Models for solar cell performance	6
1.3.1 Optical models	7
1.3.2 Electrical models	9
1.4 Overview	15
2 Film crystalline silicon solar cells	17
2.1 Introduction	17
2.2 Device physics of interfaces and localized defects in film crystalline silicon solar cells	18
2.2.1 Columnar-grained film crystalline silicon solar cells	19
2.2.2 Horizontal interfaces in film crystalline silicon solar cells	24
2.3 Plasma-enhanced chemical vapor deposition of microcrystalline silicon emitters	27

2.4	Hot-wire chemical vapor deposition of crystalline silicon absorber layers	32
2.4.1	Achieving dense crystalline growth	34
2.4.2	Process control challenges in HWCVD	37
2.4.3	Performance of compact HWCVD epitaxial Si absorber layers grown at low temperature	43
2.5	Conclusion	44
3	Device physics of silicon heterojunction solar cells	47
3.1	Introduction	47
3.2	Local epitaxial defects	49
3.2.1	Simulation details	49
3.2.2	Effects of defective epitaxial regions	51
3.2.3	Reduced-mobility layers to improve efficiency	54
3.3	Experimental characterization of lateral inversion layer transport in SHJ cells	56
3.3.1	Laser-beam-induced current imaging of defective SHJ cells	57
3.3.2	White-light-biased, selected-area-illumination measurements with variable i-layer thickness	64
3.4	Pyramidal structuring of film-silicon-based heterojunction cells	69
3.5	Conclusion	74
4	Unified modeling of optical, electrical, and material properties in thin-film solar cells	75
4.1	Introduction	75
4.2	Model details	77
4.3	Agreement between optoelectronic simulations and experimental results	82
4.4	Nanophotonic design to benefit electrical performance	84
4.5	Optoelectronic effects of changing feature aspect ratio	95
4.5.1	Changing aspect ratio: Ideal case	96
4.5.2	Accounting for localized material defects	99
4.6	Conclusion	106

5	Conclusion and outlook	109
5.1	Summary of work	109
5.2	Outlook	111
A	Convergence in numerical simulations	115
	Bibliography	117

List of Figures

1.1	Typical types of solar cells	3
1.2	Example photovoltaic current density – voltage characteristic curve	5
1.3	Equivalent circuit model of a solar cell	10
2.1	Thin-film polycrystalline Si solar cell structure based on the use of local epitaxy	19
2.2	Simulation of carrier flow toward a grain boundary under variable bulk lifetime	21
2.3	Transition from bulk-lifetime-limited to grain-boundary-limited performance	22
2.4	Depletion around a grain boundary for varying doping levels	23
2.5	Effects of base doping level on grain boundary electrostatics and device performance	24
2.6	Device physics of crystalline Si film solar cell exhibiting a horizontal defect plane at varying position	25
2.7	Efficiency of crystalline Si film solar cell exhibiting a horizontal defect plane at a varying position	27
2.8	Schematic of plasma-enhanced chemical vapor deposition	28
2.9	Fit to a Raman spectrum to estimate crystalline volume fraction	29
2.10	Raman spectra for PECVD films deposited with changing hydrogen dilution	30
2.11	Raman spectra for PECVD films deposited with changing substrate temperature	31

2.12	Schematic of hot-wire chemical vapor deposition	34
2.13	Polycrystalline films deposited with HWCVD	35
2.14	Epitaxial Si films grown with HWCVD showing roughening with increased deposition time	36
2.15	HWCVD film microstructure evolution during deposition	37
2.16	Epitaxial Si films grown with HWCVD, showing a smoother surface microstructure is maintained at reduced processing temperatures . . .	38
2.17	Severe HWCVD process drift caused by redeposition of material from chamber components	39
2.18	Secondary ion mass spectroscopy on epitaxial HWCVD film showing boron contamination	40
2.19	HWCVD chamber components	42
2.20	Secondary ion mass spectroscopy on epitaxial HWCVD film showing boron contamination	42
2.21	SEM showing dense epitaxial silicon film grown with HWCVD	44
3.1	Band diagrams for a SHJ cell at short circuit and open circuit	48
3.2	The SHJ cell structure used for device simulations	50
3.3	Simulated effect of defect-rich epitaxy on cell open circuit voltage . . .	52
3.4	Modeling results showing lateral transport in the inversion layer at an a-Si:H/c-Si heterojunction	53
3.5	Simulated effects of epitaxial pinholes on SHJ cell performance	54
3.6	The use of reduced mobility layers to mitigate lateral transport and improve performance in SHJ with isolated junction defects	55
3.7	Schematic illustration of carrier collection in SHJ solar cells	57
3.8	Laser-beam-induced current measurements near junction defects in a SHJ solar cell	60
3.9	Characteristic inversion layer transport length for changing bias in SHJ cell	62

3.10	LBIC data demonstrating wavelength independence of lateral carrier transport	63
3.11	Schematic illustration of the white-light-biased, selected-area-illumination experiment	65
3.12	Fabrication steps for the SHJ structure studied with WLB-SAL	66
3.13	Current splitting ratio observed in the WLB-SAL experiment	67
3.14	Agreement between simulation and experiment for a SHJ solar cell	71
3.15	Simulated Shockley Read Hall recombination at open circuit in a thin pyramidally structured SHJ solar cell	72
3.16	Simulated open-circuit voltage and short-circuit current for textured SHJ solar cells	73
4.1	Experimental validation of optoelectronic solar cell model	83
4.2	Generation rate profiles for different nanophotonic light-trapping approaches	85
4.3	Spectral absorption in all layers of a-Si:H solar cells	89
4.4	Correlation between electrical internal quantum efficiency and fraction of light absorbed in i-layer of a-Si:H solar cell	90
4.5	Results of 3D optoelectronic simulations of a-Si:H solar cells	91
4.6	Improvement in internal quantum efficiency of a-Si:H solar cells by coupling to a low-parasitic absorption optical mode	92
4.7	J-V curves illustrating the optimization of nanophotonic light-trapping structures in a-Si:H solar cells	94
4.8	Generation rate and electrostatic field in nanostructured a-Si:H solar cell	95
4.9	Optical effects of changing light-trapping feature aspect ratio	97
4.10	Effect of changing aspect ratio on IQE in idealized case	98
4.11	Simulated effects of localized defects in nanostructured a-Si:H solar cell	101
4.12	Interaction between spectral absorption profiles and localized defects	102
4.13	Effect of localized defects on current flow at cell operating bias	105
4.14	Recombination in a localized defect at varying cell bias	106

A.1	Convergence of optical simulations	116
-----	--	-----

List of Tables

2.1	Hall measurement results for epitaxial HWCVD films	40
3.1	Basic a-Si:H electrical parameters used for pyramidal SHJ cell simulations	70
4.1	Basic a-Si:H electrical parameters	81
4.2	Basic a-Si:H trap parameters	82
4.3	Simulated performance of a-Si:H solar cells with various light-trapping features	87
4.4	Simulated performance of a-Si:H solar cells with various light-trapping features at matched J_{sc}	88

List of Publications

Portions of this thesis have been drawn from:

M.G. Deceglie, H.S. Emmer, Z.C. Holman, A. Descoeurdes, S. De Wolf, C. Ballif, and H.A. Atwater, “Scanning laser-beam-induced current measurements of lateral transport near junction defects in silicon heterojunction solar cells,” *IEEE Journal of Photovoltaics*, 4 (1), pp.154–159 **2014**.

M.G. Deceglie, V.E. Ferry, A.P. Alivisatos, and H.A. Atwater, “Accounting for localized defects in the optoelectronic design of thin-film solar cells,” *IEEE Journal of Photovoltaics*, 3 (2), pp. 599–604 **2013**.

J. Grandidier, R.A. Weitekamp, M.G. Deceglie, D.M. Callahan, C. Battaglia, C.R. Bukowsky, C. Ballif, R.H. Grubbs, and H.A. Atwater, “Solar Cell Efficiency Enhancement via Light Trapping in Printable Resonant Dielectric Nanosphere Arrays,” *Physica Status Solidi A*, 210 (2), pp. 255–260, **2013**.

J. Grandidier, M.G. Deceglie, D.M. Callahan, and H.A. Atwater, “Simulations of solar cell absorption enhancement using resonant modes of a nanosphere array,” *Journal of Photonics for Energy*, 2, 024502, **2012**.

M.G. Deceglie, V.E. Ferry, A.P. Alivisatos, and H.A. Atwater, “Design of nanostructured solar cells using coupled optical and electrical modeling,” *Nano Letters*, 12, pp. 2894–2900, **2012**.

M.G. Deceglie and H.A. Atwater, “Effect of defect-rich epitaxy on crystalline silicon / amorphous silicon heterojunction solar cells and the use of low-mobility layers to improve performance,” *Proceedings of the Thirty-Seventh IEEE Photovoltaic Specialists Conference (PVSC)*, pp. 001417–001429, **2011**.

M.G. Deceglie, M.D. Kelzenberg, and H.A. Atwater, “Effects of bulk and grain boundary recombination on the efficiency of columnar-grained crystalline silicon film solar cells,” *Proceedings of the Thirty-Fifth IEEE Photovoltaic Specialists Conference (PVSC)*, pp. 001487–001490, **2010**.

Chapter 1

Introduction

1.1 Introduction

For billions of years, sunlight captured by photosynthesis has been the primary energy input to life on the surface of the Earth. With over 1.6×10^{17} W of solar radiation incident on the Earth, it is the largest energy flux into our terrestrial environment [1]. In the last two centuries, however, humans have begun using significantly increased amounts of energy stored in fossil fuels, changing the composition of the Earth's atmosphere and driving global climate change [2]. While convenient, this reliance on fossil fuels is not necessary; the amount of solar radiation incident on the Earth still dwarfs human energy consumption by a factor of approximately 10^4 [2, 3]. Photovoltaic cells offer a way to capture solar radiation and transfer its energy directly into electricity for human use.

A fundamental challenge in the development and deployment of solar photovoltaic technology is to lower the associated energy generation cost to directly compete with fossil-fuel-based energy sources. At present, this means the cost of photovoltaic systems must be reduced by a factor of 2–3 [4]. A key driver in this cost reduction is optimized device efficiency because increased energy output per unit area leverages all photovoltaic system costs, from raw materials and module manufacturing to installation and maintenance. To continue progress toward higher conversion efficiencies, solar cells are being fabricated with increasingly complex designs including

engineered nanostructures, heterojunctions, and novel contacting and passivation schemes. Such advanced designs require a comprehensive and unified understanding of the optical and electrical device physics at the microscopic scale. This thesis describes such a microscopic understanding of solar cell optoelectronic performance and its impact on cell optimization.

1.2 Solar cell basics

1.2.1 Operation

Photovoltaic cells are optoelectronic devices designed to transform energy captured from incident photons into electrical power. A simplified but useful understanding of their function is that they must 1) absorb incident light and 2) inject electrical charge into an external circuit at an appreciable voltage. This is most commonly achieved with inorganic semiconductors. Semiconductors are useful for this application because of their ability to maintain two populations of charge carriers (electrons and holes) at different electrochemical potentials under illumination (i.e., incident radiation drives quasi-Fermi level splitting), and also because it is possible to fabricate structures such as a p/n junctions in semiconductors to control the internal flow of electrical current. Crystalline Si (c-Si) is currently the most commonly used semiconductor for photovoltaic applications.

Two typical design approaches for photovoltaics are shown schematically in Figure 1.1. The first in Figure 1.1a, is based on a p/n junction and is the most widely used approach, and that which is implemented in most c-Si based devices. The majority of the cell consists of a light to moderately doped “base” or “absorber” region, designed to be the layer in which light is absorbed. At the front of the cell, a thin heavily doped “emitter” forms a p/n junction with the base. This results in a depletion region which exhibits a built-in electrostatic field. Under external illumination, the absorption of photons with energy greater than the band gap generates electron-hole pairs. Photogenerated minority carriers in the base then diffuse to the depletion region where the built-in electrostatic field sweeps them away, driving an electronic

current which can be used to generate power in an external circuit.

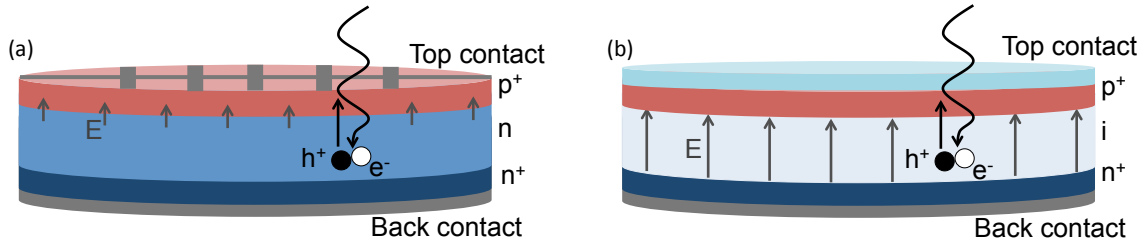


Figure 1.1. Schematic illustrations of solar cell junction types. (a) a p/n junction which relies on minority carrier diffusion to the built-field in the depletion region for carrier separation. The front contact is often a metal grid since the emitter exhibits high conductivity. (b) a n-i-p solar cell which relies on a built-in electrostatic field across and intrinsic absorber layer to drive carrier separation via drift. The front contact is often a transparent conducting film since the p⁺ layer has low conductance. Note these schematics are not to scale. A p/n junction may be several orders of magnitude thicker than a n-i-p device.

A high differential doping is desirable to realize a strong built-in potential across the junction. However, heavy doping introduces defects into the material and induces Auger recombination limiting carrier collection efficiency. Thus, as opposed to a more symmetric structure, it is preferable to adopt a junction between a very thin heavily doped region, in which there is minimal optical absorption due to its thickness, and a much thicker lightly doped region from which charges can be efficiently extracted [5]. It is also advantageous from a manufacturing perspective because the junction is often formed by thermal diffusion, which limits the reasonably achievable thickness of the top layer. The emitter region is often “dead” indicating that charge collection from it is negligibly low. In this case, the emitter is a source of parasitic optical absorption. Many solar cell designs also include a “back surface field” (BSF) region of the same doping type as the base but with higher carrier concentration. The BSF functions to reflect minority carriers away from the back contact of the device where they would otherwise be lost to recombination. The devices considered in Chapter 2 are based on a p/n junction approach. A variation of the p/n junction design is based on a heterojunction formed between an emitter and base of different material

and band gap. Silicon heterojunction devices are discussed in Chapter 3.

An alternative approach is pictured in Figure 1.1b. This n-i-p structure is utilized in low mobility materials such as hydrogenated amorphous Si (a-Si:H) and microcrystalline Si ($\mu\text{c-Si}$). Carriers in such materials cannot diffuse far enough to be collected via a traditional p/n junction. Instead, the absorber layer is much thinner (hundreds of nm as opposed to the typical thickness of hundreds of μm in a c-Si based device) and is intrinsic so that the built-in electrostatic field induced between the heavily doped p and n regions extends throughout the device. Thus photo-excited carriers are collected via electrostatic drift in these structures. The devices considered in Chapter 4 are based on a n-i-p approach. Since holes are typically less mobile than electrons, these cells are almost always fabricated such that illumination occurs through the p-layer. Because more carriers tend to be generated near the front of a device due to exponential Beer-Lambert absorption, this design rule ensures the average collection length for holes is shorter than for the more mobile electrons. Convention dictates that the layers are named in the order they are deposited. Thus an n-i-p cell pictured in Figure 1.1b would be a substrate device and a p-i-n cell would be a superstrate device; in either case illumination occurs through the p-layer. Another feature of the n-i-p approach is that a transparent conductor is often used to make top contact because the lateral conductance of the heavily doped p-layer is much less than in a crystalline emitter, thus a metallic grid front contact alone is not feasible due to increased series resistance in the emitter and the associated power loss.

1.2.2 Performance parameters

The most important performance metric for a solar cell is its efficiency, defined as the ratio of the output power to the incident optical power. Since the electrical power dissipated in a load is the product of current through the load and voltage across it, it is useful to characterize a solar cell in terms of the current it produces at a given voltage. This is typically represented as a current density – voltage (J-V) curve. Here, the total current is normalized via the area of the solar cell to obtain a current

density. A typical J-V curve is shown in Figure 1.2. Note that it resembles a diode J-V curve, but offset from 0 current. This point is discussed in more detail in Section 1.3, but is related to the fact that the device is fundamentally a diode operating in forward bias.

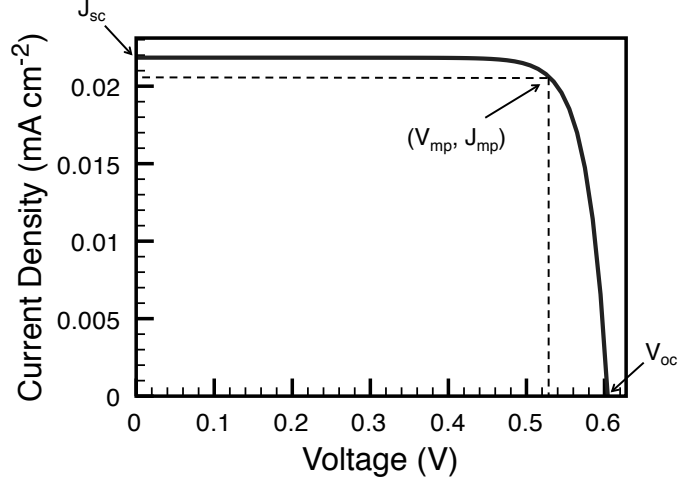


Figure 1.2. An example of a J-V curve with the open circuit voltage, V_{oc} , short circuit current density, J_{sc} , and maximum power operating point (V_{mp} , J_{sc}) labeled. The curve is from the simulation of a c-Si solar cell with a 5 μm thick base layer.

From the J-V curve, we extract several performance parameters. The open-circuit voltage, V_{oc} , is the intercept with the voltage axis at which point no current is passed through the device. The short circuit current, J_{sc} , is the intercept with the current axis which occurs when the terminals are connected to one another with no external load. At some point along the J-V curve, the power density output of the cell ($J \times V$) is maximized. This defines the maximum power operating point of the device at the associated current density (J_{mp}) and voltage (V_{mp}). The fill factor, FF is defined as

$$FF = 100 \times \frac{V_{mp}J_{mp}}{V_{oc}J_{oc}}. \quad (1.1)$$

The conversion efficiency η is then given by

$$\eta = \frac{V_{oc}J_{oc}FF}{P_{in}} \quad (1.2)$$

where P_{in} is the incident optical power. Standard test conditions for a cell dictate that the incident power is that contained in the AM1.5G spectrum, an agreed upon standard spectrum for solar illumination at the surface of the Earth with a power of 100 mW cm^{-2} [6]. The J_{sc} is often impacted by how well the device absorbs incident above-band-gap photons. A reduced V_{oc} is often indicative of low quality material or other defects, and FF can be adversely impacted by parasitic resistances in the device.

1.3 Models for solar cell performance

The limiting case efficiency for a photovoltaic cell was originally calculated by Shockley and Queisser using the principle of detailed balance [7]. It is based on a unified optical and electrical idealization of a solar cell. It is derived under the assumption a the solar cell consists of a material which perfectly absorbs all incident photons above its band gap, then perfectly collects each electron-hole pair that is not lost to radiative emission, the fundamental inverse process to absorption [8]. This approach is useful in devices which are fundamentally limited by radiative emission, such as high-quality, group III-V compound-semiconductor-based cells [9, 10]. However, useful efficiencies can be achieved at significantly reduced cost in other materials which do not reach their radiative limit. In particular it is important to note that Si, the most widely used photovoltaic material is fundamentally limited by Auger recombination due to its indirect band gap and correspondingly low radiative efficiency [11].

In the optimization of solar cells operating below the Shockley Queisser limit, it is useful to consider a performance model which more closely reproduces real-world performance. While it is often useful to focus on either the optical or electrical part of the optimization, a comprehensive model for solar cell performance must self-consistently treat the optical and electrical performance of the device. In this section we briefly introduce several different optical and electrical models for solar cells.

1.3.1 Optical models

In order to convert incident light into electrical power, a solar cell must first absorb the incident light. Thus it is desirable to implement a model for the optical absorption properties of the device. There are a wide variety of optical models available, and full consideration of each is beyond the scope of this thesis, however we present a brief summary of several important models and discuss their strengths and weaknesses. The discussion below is by no means an exhaustive list of the available optical models. Though it is often possible to carry out the calculations associated with various models, it is critical to understand the underlying assumptions of each, since they may be violated in the structures under consideration yielding unphysical results.

In the context of solar cell modeling, the ultimate goal of any optical model is to determine where light is absorbed within the structure. The assumption that every absorbed photon with energy greater than the semiconductor band gap generates one electron-hole pair in the absorbing semiconductor enables us to interpret the absorption rate as equivalent to a generation rate. In this case, the generation rate of electron-hole pairs as a function of position, \vec{r} , within a semiconductor from radiation with an optical frequency of ω , $G_{opt}(\vec{r}, \omega)$, is given by

$$G_{opt}(\vec{r}, \omega) = \frac{\varepsilon''(\omega)|E(\vec{r}, \omega)|^2}{2\hbar} \quad (1.3)$$

which is derived from the divergence of the Poynting vector, where $\varepsilon''(\omega)$ is the imaginary part of the complex permittivity of the material. Thus an optical model which yields the intensity of the optical field within the active layers is suitable for solar cell modeling. Simplified models which rely on optical reflection and transmission from the entire device to determine absorption are of limited use because they cannot distinguish between useful absorption in the active regions of the device and parasitic absorption in other layers.

One of the most basic models for light absorption in a semiconductor is the Beer-Lambert law which describes the exponential absorption of incident light in a material. It is expressed

$$I(x) = I_0 e^{-\alpha x} \tag{1.4}$$

where I is the intensity of light at a point, x within the thickness of the material, I_0 is the initial intensity of the light at the front of the material, and α is the optical absorption coefficient which depends on the complex optical index of the material. The Beer-Lambert law by itself is inherently 1D, and is useful for modeling optical absorption in simple structures which are much larger than the incident wavelength. It does not account for thin-film anti-reflection effects or Fabry-Perot type standing wave patterns within thin layers. The transfer matrix method (TMM), which accounts for reflections from multiple interfaces [12], is useful for capturing these thin-film interference effects in flat 1D layer structures, and is not computationally demanding.

An alternative that can be useful in modeling large multidimensional structures, such as pyramidal texturing on a wafer-based c-Si solar cell, is ray tracing. In this approach, optical rays are propagated through the structure, and reduced in intensity via the Beer-Lambert law when they are in absorbing material. The rays change direction according to reflection and Snell's law of refraction making this method applicable to multidimensional structures. However, since it is based on ray optics, the features of interest must be much larger than the wavelength of light under consideration. Another consideration is that enough rays must be considered with dense enough spacing order to accurately model the absorption of many photons thus approximating solar illumination.

Another approach is to numerically solve Maxwell's equations for the full geometry under consideration. Because this full-wave approach inherently captures the full classical electrodynamics of a structure, it is particularly useful when feature size is comparable to or smaller than the wavelength of light. It is valid for larger structures as well but can become computationally intensive. In Chapter 4 and Section 3.4 we adopt such a full-wave approach, the finite-difference time-domain (FDTD) method, to model light-trapping structures in solar cells designed to aid in light absorption. The FDTD technique simulates the propagation of an electromagnetic wave through

a structure in the time domain. It generates a numerical solution to Maxwell's curl equations:

$$\frac{\partial \vec{D}}{\partial t} = \nabla \times \vec{H} \quad (1.5)$$

$$\frac{\partial \vec{H}}{\partial t} = -\frac{1}{\mu_0} \nabla \times \vec{E} \quad (1.6)$$

where \vec{H} is the magnetic field, \vec{E} is the electric field, μ_0 is the permeability of free space, and \vec{D} is the electronic displacement, $\vec{D}(\omega) = \varepsilon(\omega)\vec{E}$ where $\varepsilon(\omega)$ is the frequency dependent complex permittivity of the medium. Full-wave techniques, such as FDTD, are particularly useful because they yield the optical field intensity profile calculated directly from classical electrodynamics within a structure. This can then be used in Equation 1.3 to obtain a generation profile within the device. As will be described in Chapter 4, wavelength-scale features in the absorption profile can couple to structure of the solar cell and measurably impact its electrical performance. Thus it is critical to understand when such mechanisms may be relevant, and in those cases, to adopt a full-wave approach to modeling the optics of solar cells.

1.3.2 Electrical models

Once the optical performance of a solar cell is understood, its electrical performance must be considered in order to fully understand its energy-conversion properties. One such method for understanding the electrical performance of solar cells is to consider an equivalent circuit consisting of standard circuit elements which correspond to internal features of the device. Such an equivalent circuit for a solar cell is shown in Figure 1.3. This circuit is based on a photocurrent source in parallel with a forward-biased diode. It also accounts for internal losses through the inclusion of parasitic resistances. R_s is a series resistance which parasitically dissipates power. Sources of parasitic series resistance include the contact resistance between contacts and the semiconductor, the internal resistance of the device itself, and sheet resistance of the emitter, BSF, or transparent contact. The equivalent circuit also includes a shunt

resistance, R_{sh} , which parasitically allows current to leak through the device. Sources of shunt resistance include physical conductive shunt pathways in the device, such as edges or cracks. Non-idealities in the diode characteristic of the device can also manifest as reduced shunt resistance.

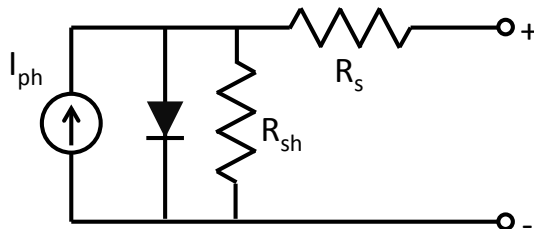


Figure 1.3. An equivalent circuit that can be used to understand the J-V behavior of a solar cell.

The current-voltage characteristic of the equivalent circuit pictured in Figure 1.3 is described by

$$I = I_{ph} - I_0 \left(e^{\frac{q(V-IR_s)}{n_d k T}} - 1 \right) - \frac{V - IR_s}{R_{sh}} \quad (1.7)$$

where I_0 is the ideal diode saturation current (commonly referred to as the dark current in the photovoltaic field), q is the elementary charge, n_d is the diode ideality factor, k is the Boltzmann constant, and T is the temperature of the device [5]. A high shunt resistance and low series resistance are desirable for optimized conversion efficiency, with both impacting the FF of the device. A high series resistance will reduce the slope of the J-V curve near open circuit and a low shunt resistance will reduce its slope near short circuit [5]. The equivalent circuit approach can be modified with more diodes and circuit elements to describe more complex performance in solar cells.

The equivalent circuit approach has proven quite useful in the photovoltaic field. It is particularly powerful in that it enables a quick and intuitive way to understand J-V curves from experimental devices, and to diagnose problems (for example, shunts and poor contact formation). It is also useful in understanding module or system

level performance phenomena, as multiple circuits can be used to represent multiple solar cells and combined into a larger circuit model of the module or system.

While the equivalent circuit approach is useful in a number of applications, and in fact parasitic resistances are referred to throughout this thesis, it represents a simplification and idealization of the full device physics governing solar cell operation. A more complete understanding of solar cell device physics is obtained by considering a more detailed model capturing the underlying carrier transport mechanisms in solar cells.

The full behavior of electrons and holes in arbitrary semiconductor structures can be described by a set of differential equations [13]. Gauss' law, Equation 1.8 describes the electrostatics of the structure.

$$\nabla \cdot \vec{D}(\vec{r}) = \rho_f(\vec{r}) \quad (1.8)$$

The current density equations (Equations 1.9 and 1.10) describe the two carrier transport mechanisms in the device: drift driven by an electrostatic field, and Fick's law diffusion driven by the random thermal motion of individual carriers.

$$\vec{J}_n(\vec{r}) = q\mu_n n(\vec{r})\vec{E}(\vec{r}) + qD_n \nabla n(\vec{r}) \quad (1.9)$$

$$\vec{J}_p(\vec{r}) = q\mu_p p(\vec{r})\vec{E}(\vec{r}) - qD_p \nabla p(\vec{r}) \quad (1.10)$$

Finally, the continuity equations (Equations 1.11 and 1.12) describe the time dependent evolution of carrier concentrations, accounting for carrier conservation.

$$\frac{\partial n(\vec{r})}{\partial t} = G(\vec{r}) - U(\vec{r}) + \frac{1}{q} \nabla \cdot \vec{J}_n(\vec{r}) \quad (1.11)$$

$$\frac{\partial p(\vec{r})}{\partial t} = G(\vec{r}) - U(\vec{r}) - \frac{1}{q} \nabla \cdot \vec{J}_p(\vec{r}) \quad (1.12)$$

The generation rate calculated from an optical model can be taken as input into the continuity equations to link the optical and electrical device models. It should

be noted that since solar cells operate in direct-current mode, the high-frequency optical fields do not directly couple to Equations 1.8 - 1.12. In Equations 1.8 - 1.12, n and p are the electron and hole concentrations, G is the generation rate, U is the recombination rate, q is the elementary charge, \vec{J}_n and \vec{J}_p are the electron and hole current densities, μ_n and μ_p are the electron and hole mobilities, \vec{E} is the electrostatic field, D_n and D_p are the electron and hole diffusion coefficients, and \vec{D} is the electric displacement.

In equilibrium conditions, the electron and hole concentrations can be described by a single electrochemical potential, called the Fermi level as E_F , as shown in Equations 1.13 and 1.14, where n_i is the intrinsic carrier concentration and E_i is the intrinsic Fermi level. (Note that position dependence has not been explicitly included, but is implied.)

$$n = n_i e^{(E_F - E_i)/kT} \quad (1.13)$$

$$p = n_i e^{(E_i - E_F)/kT} \quad (1.14)$$

When a semiconductor is not in equilibrium, the populations of holes and electrons are not necessarily in equilibrium with one another, thus their populations cannot be described by a single electrochemical potential. In non-equilibrium conditions, it is useful to introduce the construct of the quasi-Fermi level for electrons and holes, E_{Fn} and E_{Fp} , defined such that the electron and hole concentrations satisfy the relations in Equations 1.15 and 1.16 [14].

$$n = n_i e^{(E_{Fn} - E_i)/kT} \quad (1.15)$$

$$p = n_i e^{(E_i - E_{Fp})/kT} \quad (1.16)$$

The quasi-Fermi level construct is particularly useful because it enables a reformulation of the electron and hole current equations (Equations 1.9 and 1.10) to simulta-

neously account for both drift and diffusion as shown in Equations 1.17 and 1.18.

$$\vec{J}_n(\vec{r}) = \mu_n n(\vec{r}) \nabla E_{Fn}(\vec{r}) \quad (1.17)$$

$$\vec{J}_p(\vec{r}) = \mu_p p(\vec{r}) \nabla E_{Fp}(\vec{r}) \quad (1.18)$$

In contrast to an equivalent circuit approach, solving Equations 1.8 - 1.12 for the solar cell device structure yields a full microscopic description of its electrical performance. However, this is non-trivial for all but a few idealized cases, such as an ideal 1D diode. Numerical methods such as the finite element method (FEM) can be used to numerically solve the semiconductor device equations in multidimensional structures, an approach that is used throughout this thesis.

The full device physics approach accounts for imperfect carrier collection from the active region of a device. This is accomplished through the inclusion of various models for the recombination rate, U , which describes the local rate at which electrons and holes recombine with one another, thus being lost from the available photocurrent. Typical sources of recombination in solar cells include band-to-band radiative recombination, Auger recombination, and trap-mediated (Shockley-Read-Hall) recombination. Carriers recombine both in the bulk and at defective interfaces.

Trap-mediated recombination is the dominate recombination mechanism in the materials considered in this thesis. Traps are localized electronic states in the energetic band-gap of the semiconductor. Typical sources of traps include chemical impurities and crystallographic defects in the material. The statistics of recombination through such states is described by Shockley-Read-Hall statistics. For a trap located at energy E_t above the valence band of the material, the recombination rate is given by

$$U = \frac{\sigma_n \sigma_p v_{th} N_t (pn - n_i^2)}{\sigma_n (n + n_1) + \sigma_p (p + p_1)} \quad (1.19)$$

where σ_n and σ_p are the trap capture cross sections for electrons and holes, respectively, N_t is the concentration of trap states, n_i is the intrinsic carrier

concentration, $n_1 = n_i \exp((E_t - E_i)/kT)$, and $p_1 = n_i \exp((E_i - E_t)/kT)$.

There are multiple methods for incorporating Shockley-Read-Hall recombination in a numerical device physics model. The simplest is to use the electron and hole concentrations (n and p) along with the associated recombination rate (U) to couple Equation 1.19 to the charge transport equations (Equations 1.9-1.12). This method tends to be computationally inexpensive and is useful for simulating bulk recombination processes. While this method captures the full carrier concentration dependent statistics of Shockley-Read-Hall recombination, it does not capture the electrostatics of trapped charges. An alternative is to account for the statistics of trap occupation and explicitly include their impact on the electrostatic field within the device. Both methods are implemented in this thesis for different applications.

Similarly, there are multiple methods available to account for recombination at surfaces. Semiconductor surfaces tend to exhibit recombination active trap states, which mediate carrier recombination via the same mechanism of bulk Shockley-Read-Hall recombination. For example, the surface recombination rate for a surface trap level is given by an expression identical to Equation 1.19 except that the bulk concentration of trap states N_t is replaced by a surface concentration $N_{t,s}$ with dimension of inverse area. A parameter known as the surface recombination velocity (SRV) for electrons (S_n) or holes (S_p) can then be defined as

$$S_{n,p} = \sigma_{n,p} v_{th} N_{t,s}. \quad (1.20)$$

The surface recombination rate, U_s is then given by

$$U_s = \frac{pn - n_i^2}{(n + n_1)/S_p + (p + p_1)/S_n} \quad (1.21)$$

Under low-level injection (when majority carrier concentration is not perturbed) the SRV can be also be interpreted as a boundary condition imposing a minority carrier recombination current density, J_{SR} , lost to recombination at the interface:

$$J_{SR} = qS_p(p - p_0) \quad (1.22)$$

expressed here for holes in an n-type material, where p_0 is the equilibrium hole concentration.

The simplest way to account for surface recombination is to specify a surface recombination velocity (SRV), and impose the resulting recombination rate at the interface as the device physics equations are solved. However, as in the case of bulk recombination, a more complete model of an interface can be obtained by considering the electrostatics of filled interface states. The importance of this is discussed in Section 2.2.

1.4 Overview

This thesis addresses several advanced designs for silicon-based solar cells with a focus on understanding their microscopic optoelectronic device physics. Our approach relies heavily on the use of computer simulations to numerically solve the governing optical and electrical equations described in Section 1.3. Thus we avoid idealized limiting case versions of the governing physics such as the equivalent circuit model. Such an approach is critical to gain a full understanding of the operation of these advanced devices.

In Chapter 2, we consider thin crystalline silicon solar cells. These devices are based on the use of a monocrystalline or large-grained polycrystalline silicon base layer, but avoid material utilization costs associated with wafer based devices. We first consider the electrical device physics associated with recombination active interfaces which may occur in these devices. We find that to fully understand the effects these interfaces have on device performance, it is important to consider the full multidimensional device physics associated with the interfaces. We also describe the experimental development of devices based on a thin crystalline base grown with hot-wire chemical vapor deposition (HWCVD) and discuss challenges associated with this approach.

Chapter 3 addresses the device physics of a p/n heterojunction between crystalline Si (c-Si) and wider band-gap hydrogenated amorphous silicon (a-Si:H). Devices based

on this heterojunction, commonly referred to as silicon heterojunction (SHJ) cells, obtain high photovoltages due in part to excellent passivation of the c-Si surface by a-Si:H. They are also known to be extremely sensitive to imperfections at the interface between the a-Si:H and the c-Si. We describe simulations and experiments that show this sensitivity is due in part to lateral transport of photo-excited carriers near the heterointerface. These results provide an improved understanding of the device physics of SHJ cells and will aid in the development of advanced designs including all back-contacted heterojunction structures and the use of novel passivation layers.

Finally, in Chapter 4 we describe a simulation-based method for simultaneously optimizing the optical and electrical properties of thin-film solar cells featuring nanophotonic light-trapping structures. A key challenge in the optimization of such light-trapping structures is to account for the interdependent optical and electrical properties of solar cells, including variations in material quality. We address this challenge with multidimensional optoelectronic simulations that fully account for the optical and electrical properties of the devices including the effects of imperfect carrier collection. We demonstrate that light-trapping structures can be designed to reduce the fraction of light parasitically absorbed within the device and measurably increase the internal quantum efficiency of charge collection. Our results highlight the full potential of engineered nanophotonic light trapping, and represent a new optimization paradigm in which optical design can be leveraged to benefit the electrical properties of solar cells.

Advanced designs such as those considered here take on higher complexity than previous generations of solar cells in the pursuit of increased efficiency and reduced cost. In turn, they are governed by more complex optoelectronic device physics. In the context of thin-crystalline cells, a-Si/c-Si heterojunction cells, and devices with engineered nanophotonic light trapping, this thesis demonstrates the importance of understanding the device physics governing solar cell operation at the microscopic scale. This type of comprehensive approach will be critical in continuing efficiency improvements and cost reductions in future generations of solar energy conversion devices.

Chapter 2

Film crystalline silicon solar cells

2.1 Introduction

Crystalline Si (c-Si) solar cells are the dominant photovoltaic technology for terrestrial power generation, however their cost needs to be reduced by a factor of 2–3 in order to directly compete, subsidy free, with fossil-fuel-based, grid-scale energy generation technologies [4]. Approximately 1/3 of the cost of a module is the cost of the Si wafer itself, driven in part by poor material utilization [4]. In particular, roughly half of the crystalline material is lost to kerf (i.e., sawdust) in the wafering process. In addition, due in part to handling requirements, a typical photovoltaic Si wafer is approximately 180 μm thick [4], though with appropriate light-trapping design and surface passivation, efficiencies exceeding 15% are possible in cells tens of μm thick [15]. Thus in order to drive cost lower, it is desirable to develop a crystalline-Si-based technology in which the Si thickness is reduced and the material utilization is simultaneously increased. To this end, there have been a wide variety of approaches considered [4, 16].

An alternative to wafer-based photovoltaics is based on thin-film active layers deposited electrochemically or from gas phase precursors; examples include CIGS, CdTe, or thin-film amorphous or microcrystalline Si solar cells. In this chapter we consider a film-based approach in which the absorber layer consists of large-grained polycrystalline Si deposited directly from the gas phase. Thin-film photovoltaic

technologies benefit from reduced manufacturing cost, however due to reduced material quality, they typically achieve lower efficiency than c-Si-based devices. The approach considered in this chapter is based on the use of hot-wire chemical vapor deposition (HWCVD) to deposit Si epitaxially on a template layer [17–23]. A schematic illustration of such a structure is shown in Figure 2.1. This approach eliminates the traditional wafer-based process in favor of a film deposition process. However, the active material would be large-grain polycrystalline, maintaining the material benefits of the wafer-based approach. In addition, we target low processing temperatures enabling the use of low-cost substrates such as glass. In Section 2.2, we first present a discussion of the device physics associated with such a device, based on simulations of the structure. In Section 2.3 we present the experimental development of microcrystalline Si emitter layers deposited by plasma-enhanced chemical vapor deposition (PECVD). Finally in Section 2.4 we detail the experimental development of dense epitaxial Si films deposited at low-temperatures and discuss technical challenges to this approach.

2.2 Device physics of interfaces and localized defects in film crystalline silicon solar cells

Active layers of a solar cell fabricated by epitaxial thickening of a template would inherit its grain structure from the underlying substrate. Thus, since many candidate template layers are polycrystalline, these epitaxially deposited devices would also be polycrystalline. The boundaries between crystalline domains are likely to exhibit high densities of recombination active defects which limit efficiency [16]. Depending on the substrate used, the approach can also result in crystallographic dislocations extending through the device [22]. The film deposition approach can also introduce horizontal interfaces into the device; for example, an interface between the base and emitter can result from the use of separate deposition steps for each layer. It is important to understand the performance limiting factors in the proposed cell structure, including the impact of both horizontal and vertical interfaces and bulk

recombination within crystalline grains. In this section, we present the results from 2D carrier transport simulations to elucidate the device physics associated with such defects.

2.2.1 Columnar-grained film crystalline silicon solar cells

We first consider the effects of grain boundaries induced by the growth template along with intragranular defects associated with the bulk quality of the material. Grain boundaries would manifest as vertical interfaces in a columnar-grained material such as that shown in Figure 2.1. Previous work has considered the effects of these factors [24–30], however few studies [25, 26] thoroughly treat the effects of localized traps at grain boundaries. Instead, it is common to define effective recombination rates and surface recombination velocities, an approach which has been shown to be of limited use [26]. We describe a two-dimensional device model that explicitly models the statistics and electrostatics of traps at the grain boundary along with other important physical processes including light absorption and bulk intragranular carrier recombination. We use this model to more completely understand and optimize the device physics of polycrystalline film solar cells.

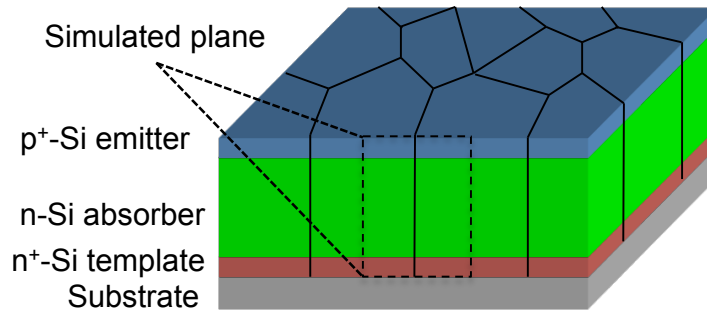


Figure 2.1. Illustration of the thin-film polycrystalline Si solar cell structure based on the use of local epitaxy to thicken a polycrystalline template. The dashed box indicates the two-dimensional plane in which device performance was modeled. [31]

The simulated structure consists of an n-type Si absorber layer of varying thickness and doping, a 50 nm p-type top-side emitter doped at 10^{20} cm^{-3} and 50 nm n-type

layer on the back doped at 10^{20} cm^{-3} to provide a back surface field. Contacts are modeled as perfect ohmic contacts. The simulation area is the width of a grain, with the grain boundary defined in the center of the device and extending vertically through it as illustrated in Figure 2.1. The grain width is varied from 50 nm - 4 μm . We also vary the bulk Si Shockley-Read-Hall (SRH) recombination lifetime for electrons and holes, τ , to model the effect of bulk intragranular recombination. Mobility is taken as doping dependent in all layers according to the model presented in [32].

To model grain boundary recombination, we explicitly define the trap distribution in the band gap at the grain boundary. We model the energetic trap distribution at the grain boundary, $N(E)$, as a double exponential:

$$N(E) = N_{gb}e^{-E/\beta_1} + \gamma N_{gb}e^{-E/\beta_2} \quad (2.1)$$

where N_{gb} is a surface density of traps in units of $\text{cm}^{-2} \text{ eV}^{-1}$ and E is the energetic distance into the band gap from the corresponding band edge in eV. In this work, the parameters used are: $\gamma = 0.01$, $\beta_1 = 0.025 \text{ eV}$, and $\beta_2 = 0.25 \text{ eV}$. We include this distribution for both a acceptor-like trap distribution distributed below the conduction band and an donor-like distribution above the valence band. Capture cross sections for both carrier types are taken as 10^{-15} cm^2 [25, 26]. The value of N_{gb} is varied to model the effect of grain boundary quality, including passivation effects.

We numerically simulated the performance of these structures using the a commercial semiconductor FEM package [33]. The generation profile under illumination is calculated based on single pass absorption from a spectrally weighted sum of 95 light beams of different wavelength and intensity to approximate the AM1.5G solar spectrum. The carrier transport and Poisson equations (Equations 1.8 - 1.12) are numerically solved on a mesh for varying contact voltages to extract current density – voltage (J-V) curves and the photovoltaic performance parameters for each set of simulation parameters.

We first characterize the transition from grain-boundary-limited to bulk-lifetime-limited performance as a function of the trap density at the grain boundaries and

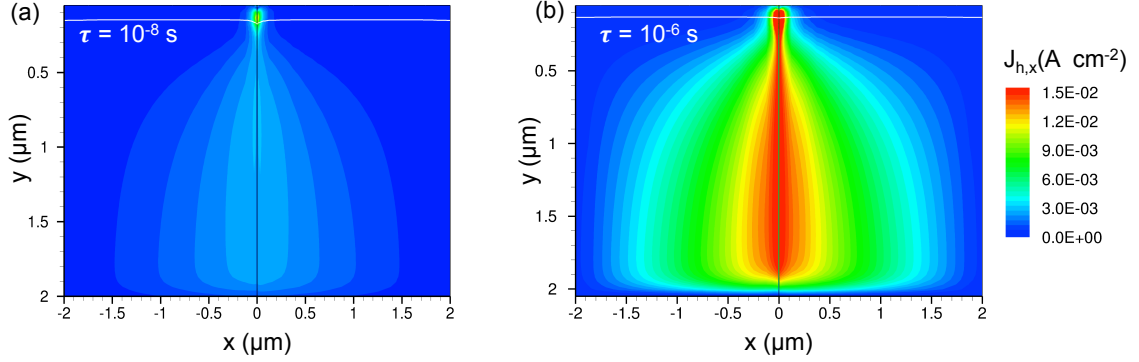


Figure 2.2. Simulation results showing the magnitude of the x-component of the hole current density in the base region under AM1.5G illumination at open circuit for 4 μm grain width, 2 μm base thickness, $N_D = 10^{16} \text{ cm}^{-3}$ base doping level, and $N_{gb} = 10^{14} \text{ cm}^{-2} \text{ eV}^{-1}$, with bulk lifetimes of (a) 10^{-8} s and (b) 10^{-6} s . The currents shown are directed toward the grain boundary. The white lines near the top of the plots indicate the depletion region edges. [31]

examine the device physics governing this transition. Figure 2.2 illustrates the interplay between bulk lifetime and grain boundary recombination. For identical grain size and grain boundary trap density, the longer bulk lifetime ($\tau = 10^{-6} \text{ s}$) case exhibits a larger horizontal component of the minority current density directed toward the grain boundary as more carriers are driven to recombine at the boundary to meet the open circuit condition. We note that $\tau = 10^{-6} \text{ s}$ corresponds to a bulk minority carrier diffusion length of 33 μm , and $\tau = 10^{-8} \text{ s}$ to a diffusion length of 3.3 μm . Even though 33 μm is much longer than the width of the grain for the case pictured in Figure 2.2, the x-component of the current goes to 0 at $x = \pm 2 \mu\text{m}$ due to the assumed presence in the model of another grain boundary at $x = \pm 4 \mu\text{m}$.

The effects of these microscopic device physics on overall performance are presented in Figure 2.3. Toward the left of the plot in Figure 2.3a (corresponding to lower grain boundary trap densities), efficiencies for the same bulk lifetimes converge with one another and become much less sensitive to grain size, indicating bulk-lifetime-limited performance. Toward the right of the plot (corresponding to higher grain boundary trap densities), curves of the same grain size converge, indicating grain-boundary-limited performance. We also see that, in the intermediate regime between grain-boundary-dominated and bulk-dominated performance, improved bulk

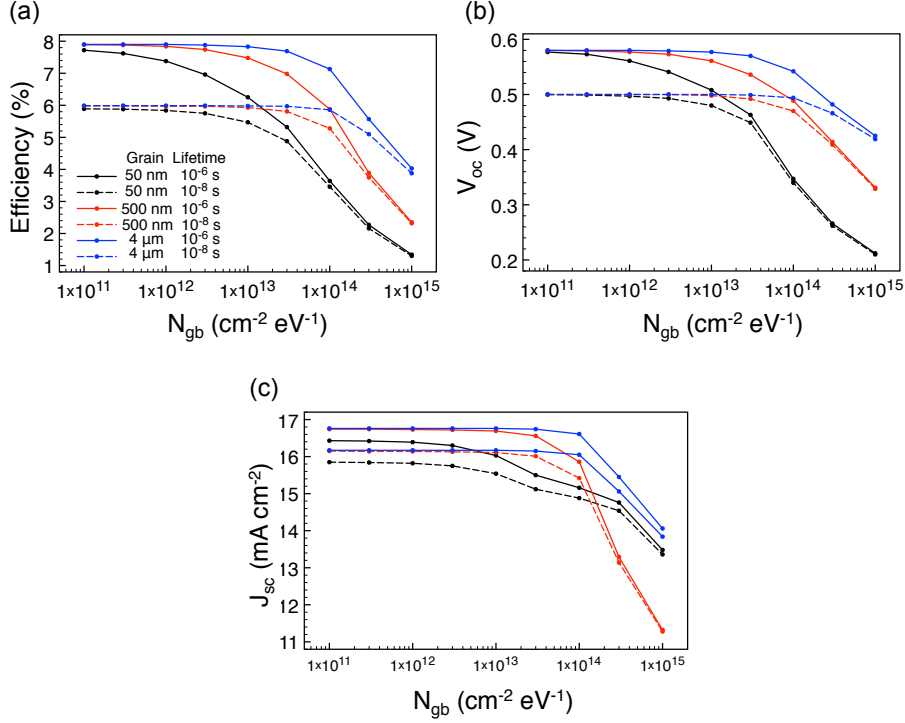


Figure 2.3. Simulated AM1.5G photovoltaic performance parameters characterizing the transition between bulk SRH-limited performance at low intergranular defect density and grain-boundary-limited performance at high intergranular defect density for cells with $2 \mu\text{m}$ thick base layers and $N_D = 10^{16} \text{ cm}^{-3}$. [31]

lifetimes augment the reduction in efficiency due to reduced grain size (also evident in Figure 2.2). These results emphasize the importance of long bulk lifetimes and the inherent trade-off between grain size and grain boundary passivation. In Figure 2.3c, we note that the 50 nm grain, high trap density cases actually produce higher short circuit currents than the 500 nm grain cases. We attribute this to significant depletion of the small grains resulting in the onset of carrier collection by drift. However, the open circuit voltage is so strongly degraded in this case that the ultimate efficiency remains lower than for larger grain microstructures.

Next, we investigate the effect of base doping level on recombination at the grain boundary. Figure 2.4 shows that when the base is more lightly doped, the partially depleted region surrounding the grain boundary extends further into the bulk. This extended partially depleted region is characterized by an electric field directed toward

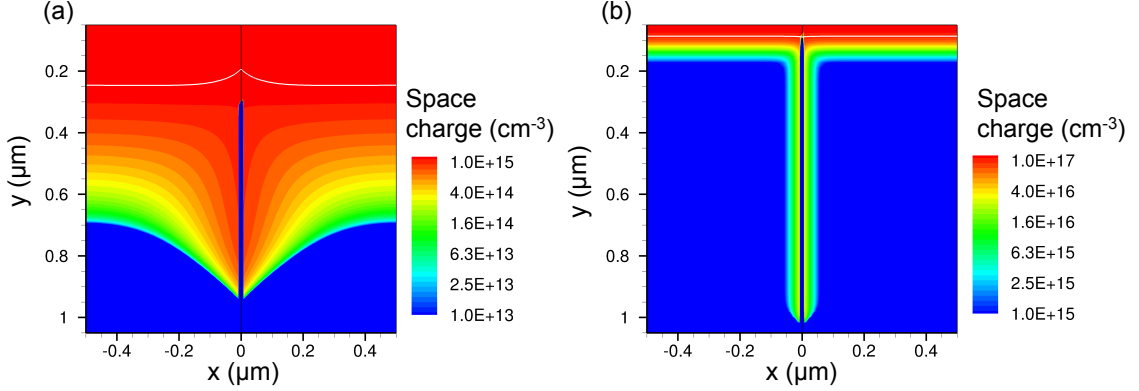


Figure 2.4. Simulation results showing partial depletion in the base surrounding the grain boundary under AM1.5G illumination at open circuit for bases doped at $N_D = 10^{15} \text{ cm}^{-3}$ (a) and 10^{17} cm^{-3} (b). The color scales extend from 1% to 100% of the base doping level. The base is 1μ thick, the grain is 1μ wide, $\tau = 10^{-6} \text{ s}$, and $N_{gb} = 10^{14} \text{ cm}^{-2} \text{ eV}^{-1}$. [31]

the grain boundary (as indicated in Figure 2.5a) that drives minority carrier current flow toward the boundary under open-circuit conditions. We also note that our model, which explicitly considers trap electrostatics at the grain boundary, provides a detailed view of the microscopic device physics that would not be evident in analysis relying on the assumption of quasineutrality.

In agreement with this physical understanding, Figure 2.5b confirms that the efficiencies of the simulated devices with higher base doping levels are more robust with respect to increasing grain boundary trap density. This agrees with previous reports [26, 27]. Based on the device physics described above and illustrated in Figure 2.4, we attribute the increased performance of the more heavily doped devices to the shorter Debye screening length, which confines the electric field to the region immediately surrounding the grain boundary. Although even higher doping might further reduce grain boundary recombination, such devices would ultimately display degraded performance due to reduced bulk minority carrier lifetime at high doping, reduced efficacy of the back surface field, and degraded carrier mobility. We also note that regions of heavier doping surrounding the grain boundary would likely have beneficial impact, since they would limit the physical extent of the partially depleted region. This case is often observed in practice since dopant segregation is known

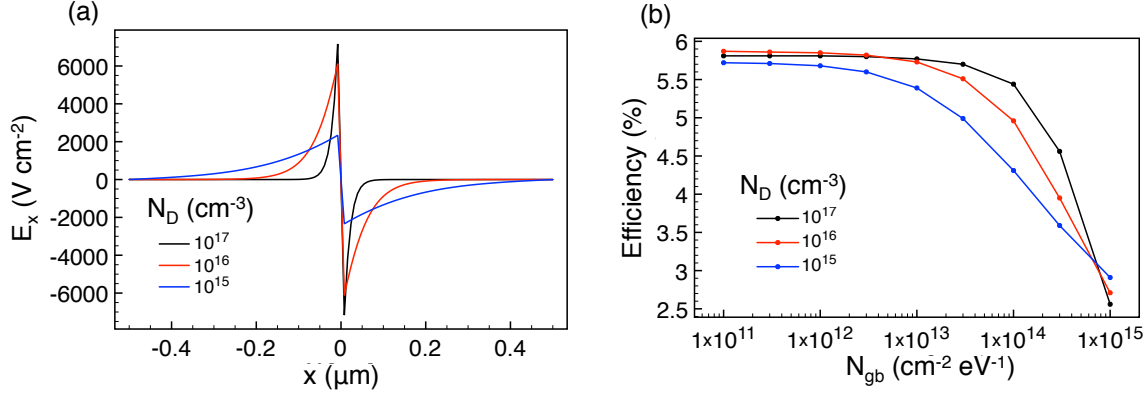


Figure 2.5. Simulation results for devices under AM1.5G illumination with a 1 μm thick base, 1 μm wide grain, and $\tau = 10^{-6}$ s. (a) The x-component of the electric field along the horizontal slice at the middle of the base region ($y = 550$ nm) for $N_{gb} = 10^{14}$ cm^{-2} eV^{-1} and selected base doping levels at open circuit. Note that the field is directed toward the grain boundary and extends further into the bulk with decreasing base doping level. (b) Cell performance for varying base doping level as grain boundary quality is reduced. [31]

occur at grain boundaries.

2.2.2 Horizontal interfaces in film crystalline silicon solar cells

Since the approach considered in this chapter is deposition based, horizontal interfaces may be introduced into the active device layers due to sequential deposition steps. Typically the different device layers (back surface field, base, and emitter) would be deposited by separate processes, possibly in separate deposition chambers to prevent dopant cross contamination. In this section we consider the effects of horizontal interfaces at different locations throughout the device. Though the most likely location for a horizontal interface is between device layers, understanding the effects of location is important because it can inform process decisions. For example, buffer layers with variable doping could be introduced to move the physical interface associated with a process/chamber change away from the electrical junction between device layers.

The simulations are carried out in the same manner described in Section 2.2.1, except that there is no vertical interface. Instead, a defective interface with

$N_{gb} = 3 \times 10^{14} \text{ cm}^{-2} \text{ eV}^{-1}$ is defined horizontally through the device. Note that though the simulation is carried out in 2D, the structure is effectively 1D. Here, we use a value for the bulk lifetime of $\tau = 10^{-6} \text{ s}$.

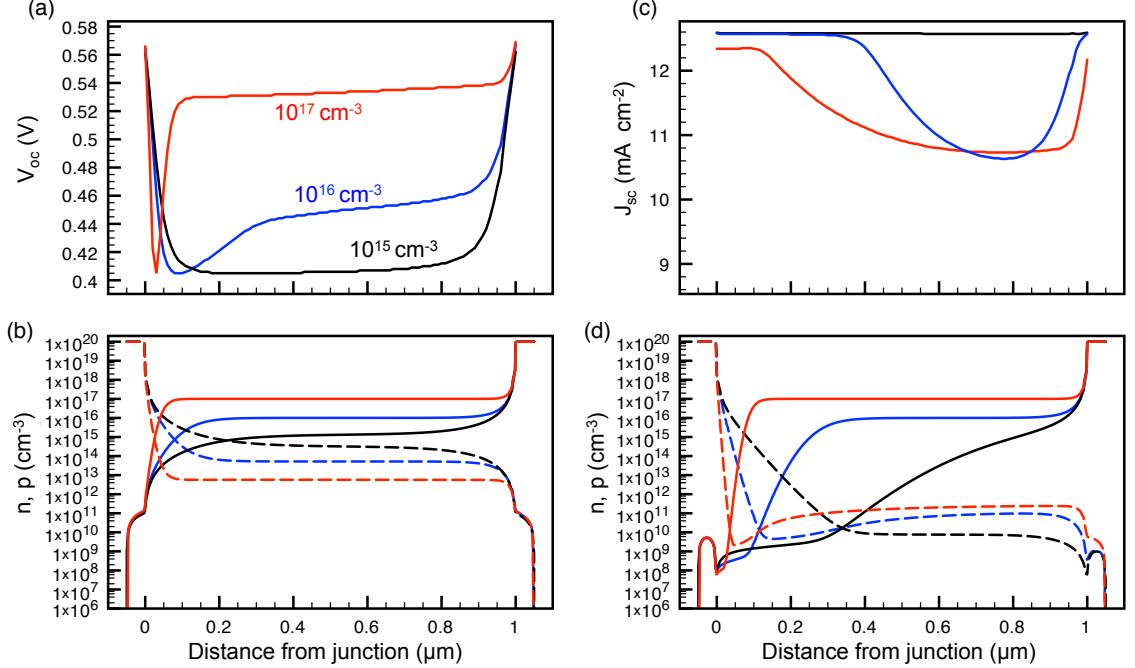


Figure 2.6. Device physics of crystalline Si film solar cell under AM1.5G illumination exhibiting horizontal interface defect planes for various levels of N_D in the base as indicated by color and labeled in panel (a). (a) The V_{oc} as a function of interface position in the base. (b) Electron and hole concentrations in a cell with no horizontal defective interfaces at open circuit. (c) The J_{sc} as a function of interface position in the base. (d) Electron and hole concentrations in a cell with no horizontal defective interfaces at short circuit. In all panels, 0 is the emitter/base junction and the base is $1 \mu\text{m}$ thick. The dashed lined in (b) and (d) are hole concentrations, p , and the solid lines are electron concentrations, n .

Figure 2.6ac shows the V_{oc} and J_{sc} as a function of horizontal interface position within a $1 \mu\text{m}$ base, for variable doping levels. The dependence on position and doping level can be understood in terms of the carrier-density-dependent recombination statistics. For example, recall Equation 1.19 for recombination through a single trap state:

$$U = \frac{\sigma_n \sigma_p v_{th} N_t (pn - n_i^2)}{\sigma_n (n + n_1) + \sigma_p (p + p_1)}. \quad (2.2)$$

We see that recombination is highest when $pn - n_i^2$ is high, i.e. the numerator in Equation 2.2 is large indicating the carrier gasses are relatively far out of equilibrium, and also when $p + n$ is low, resulting in a low value in the denominator. This condition is met when the system is far out of equilibrium, and there are nearly equal concentrations of electrons and holes present. Figure 2.6b shows the electron and hole concentrations in the cell at open-circuit under AM1.5G illumination. We note that as the doping level is decreased, the value of $n + p$ is reduced near the middle and rear regions of the absorber, which is reflected in higher sensitivity of V_{oc} to the presence of the horizontal defective interface. It is clear from a comparison of Figure 2.6a and 2.6b, that when the interface is located at the position where $n = p$, the V_{oc} is strongly degraded for all doping levels. We also note that right at the physical interfaces between device layers, carrier populations become inverted, and V_{oc} is robust with regard to the presence of interface defects. In the short circuit case (Figure 2.6cd) we see that lower base doping levels are advantageous due to partial depletion extending through a significant portion of the base (or the entire base for the $N_D = 10^{15} \text{ cm}^{-3}$). The partial depletion is apparent in the electron concentrations in Figure 2.6d and is associated with an electrostatic field that drives carrier collection via drift.

Figure 2.7 shows the ultimate conversion efficiency obtained for various base doping levels as a function of horizontal interface position. In the control case for which no horizontal interface is included in the model, the efficiencies for doping levels in the base of $N_D = 10^{15}$, 10^{16} , and 10^{17} cm^{-3} were 5.71%, 5.85%, and 5.79%, respectively. It is clear that heavier base doping benefits the conversion efficiency when the defect is located in the bulk of the device. We note that efficiency is dominated by V_{oc} near the front of the device, and J_{sc} near the rear. As expected from the results presented in Figure 2.6, the efficiency is not strongly degraded when the defective physical interface is present at the electrical junction between adjacent

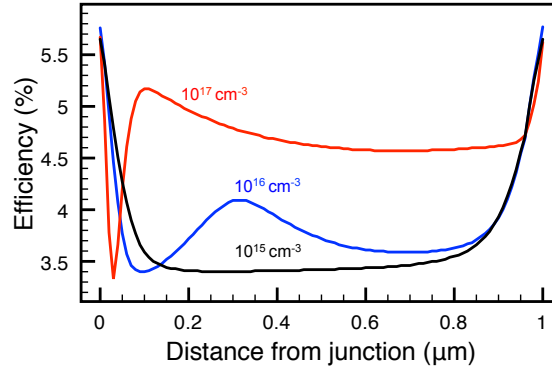


Figure 2.7. AM1.5G conversion efficiency for the devices considered in Figure 2.6, with a horizontal defect plane at varying position. The value of the active donor concentration in the base, N_D , is indicated by color as labeled.

device layers. This is a very promising result for the deposition-based approach described in this chapter, in which the natural place for physical interfaces to occur is the interface between device layers deposited with sequential processes.

2.3 Plasma-enhanced chemical vapor deposition of microcrystalline silicon emitters

In typical wafer-based cells, emitters are thermally diffused, but this process is not compatible with low-cost substrates which necessitate reduced processing temperatures. Thus, the proposed cell will require a deposited emitter layer. We investigated the use of doped microcrystalline silicon ($\mu\text{-Si}$) deposited via plasma-enhanced chemical vapor deposition (PECVD) for use as an emitter layer in thin-film c-Si devices. Our approach was to first demonstrate and optimize the emitter film on a c-Si wafer in order to isolate the emitter quality and performance from complications arising from a deposited film absorber layer.

In PECVD, an RF plasma is used to dissociate process gasses into film precursors. There are many different variations on the technique, but the basic implementation we used is illustrated in Figure 2.8. For the deposition of amorphous silicon (a-Si) and $\mu\text{-Si}$, SiH_4 and H_2 are typically used as process gasses. The mechanisms governing

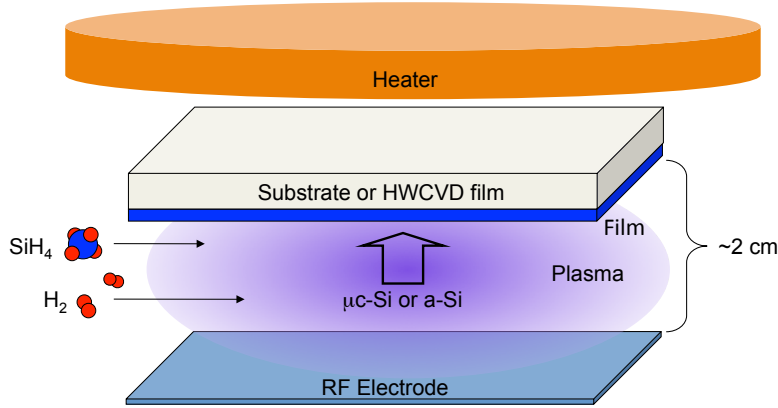


Figure 2.8. Schematic of the PECVD technique. SiH₄, and H₂ are dissociated in an RF plasma into growth precursors for either $\mu\text{c-Si}$ or a-Si depending on the processing conditions.

the deposition are complex and are influenced by secondary reactions of radicals in the plasma (after initial plasma dissociation) and surface reactions on the deposited film [34, 35]. Hydrogen partial pressure during growth is a critical process parameter since hydrogen promotes the $\mu\text{c-Si}$ phase over the a-Si phase, and H bonds to Si within the film aiding in passivation of dangling Si bonds that would otherwise create electronic defect states [35].

PECVD can be used to deposit either amorphous Si (a-Si) or $\mu\text{c-Si}$. $\mu\text{c-Si}$ is a mixed phase material consisting of small crystallites surrounded by an amorphous matrix. The transition between deposition of these two materials is governed by the PECVD process parameters, including H₂ partial pressure and substrate temperature. Though a-Si can be used to form a junction with crystalline Si in silicon heterojunction (SHJ) cells to obtain high V_{oc} , these junctions are extraordinarily sensitive to interface properties as discussed in Chapter 3, and we expect a $\mu\text{c-Si}/\text{c-Si}$ junction to be more robust. This is important for early stage experimental investigations of the HWCVD absorber approach since it avoids potential complications arising from heterojunction formation on the rough, as-grown absorber surface. To realize this robustness, we target a high crystalline fraction in the mixed phase material so that the junction functions as a c-Si homojunction.

In our PECVD system, process gasses enter the chamber through a T inlet on one

edge of the chamber and the plasma is maintained by a 13.56 MHz RF excitation of the capacitor formed between the sample and an electrode. We used H₂ and 151 ppm trimethylboron (TMB) with 5% SiH₄ in Ar as process gasses for deposition of p-type material. The flow rates of the individual process gasses were controlled with mass flow controllers. We define the parameter R to be the flow ratio of H₂ to SiH₄. The temperature of the substrate is controlled by an external heater directly above the sample position. All substrate process temperatures for both HWCVD and PECVD are reported as the temperature maintained externally by the heater on the chamber as measured during processing with a thermocouple (T_{set}). In this work the plasma power is constant at 0.03 W cm⁻². The pressure is controlled by a butterfly valve intake of the turbo pump.

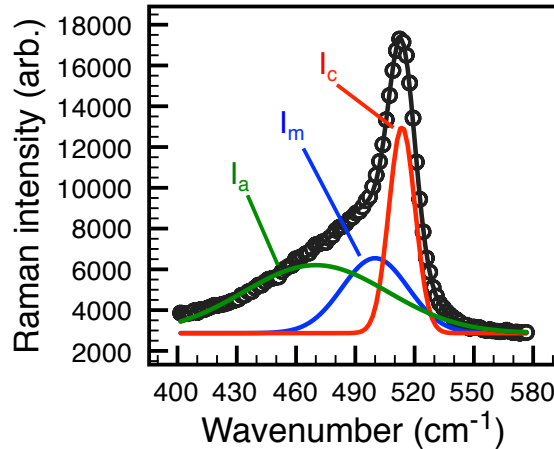


Figure 2.9. An example fit to a Raman spectrum collected from a μ c-Si film deposited at $T_{set} = 450^\circ$ C, at a pressure of 400 mTorr, and at an H₂/SiH₄ flow ratio, R , of 153. The fit gave an amorphous peak at 470 cm⁻¹ (green), an intermediate crystalline peak at 500 cm⁻¹ (blue) and a crystalline peak at 514 cm⁻¹ (red). This fit yields a crystalline volume fraction X_c of 0.51.

We used Raman Spectroscopy, in which the energy shifts of photons which have interacted with vibrational modes of a material are measured, to estimate the crystalline volume fraction of the PECVD films as processing parameters were changed. Raman spectroscopy is widely used to obtain a semiquantitative measure of crystalline volume fraction in μ c-Si films by fitting three Gaussian peaks to the

spectra, and attributing the peaks near wavenumbers 500 and 520 cm^{-1} to the crystalline phase, and the peak near 480 cm^{-1} to the amorphous phase [36, 37]. An estimate of the crystalline volume fraction is then obtained from Equation 2.3 where I indicates the integrated intensity under each peak as shown in Figure 2.9.

$$X_c = \frac{I_c + I_m}{I_c + I_m + I_a} \quad (2.3)$$

The presence of atomic H during deposition is known to promote the crystalline phase [35]. We characterized the transition from purely a-Si to $\mu\text{c-Si}$ deposition as R is varied for our process. This is shown in Figure 2.10. The emergence of the crystalline peak near 520 cm^{-1} indicates the onset of $\mu\text{c-Si}$ near a value of $R=78$.

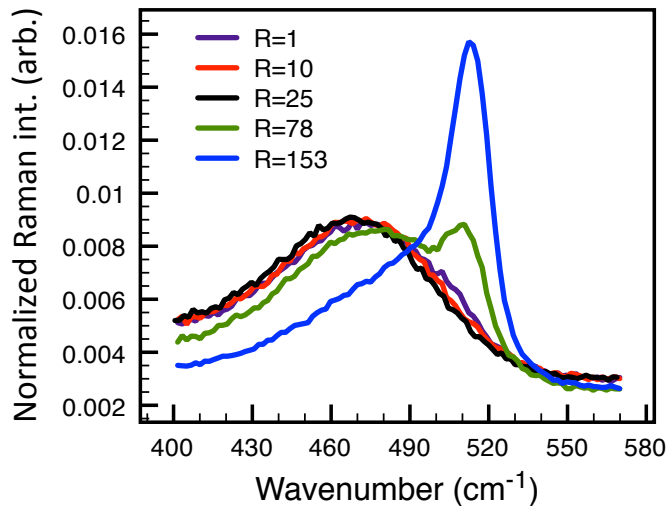


Figure 2.10. Raman spectra of PECVD films showing the transition from a-Si deposition to $\mu\text{c-Si}$ deposition under varying hydrogen dilution. The films were deposited at $T_{set} = 450^\circ \text{C}$, at a pressure of 400 mTorr. The film deposited at $R = 78$ had $X_c = 0.11$ and that deposited at $R=153$ had $X_c=0.51$. The spectra are normalized to their respective integrated intensities to enable comparison.

The crystalline volume fraction, X_c of $\mu\text{c-Si}$, also depends on substrate temperature and is typically maximized at a substrate temperature below 400 $^\circ\text{C}$, with the reduction in X_c at temperatures near or above 500 $^\circ\text{C}$ attributed to lack of hydrogen coverage on the growth surface [35]. We observe this trend with our PECVD process

indicated by the Raman spectra shown in Figure 2.11. From these observations we identify an optimal substrate temperature of $T_{set} = 300$ °C to maximize the crystalline volume fraction of the film.

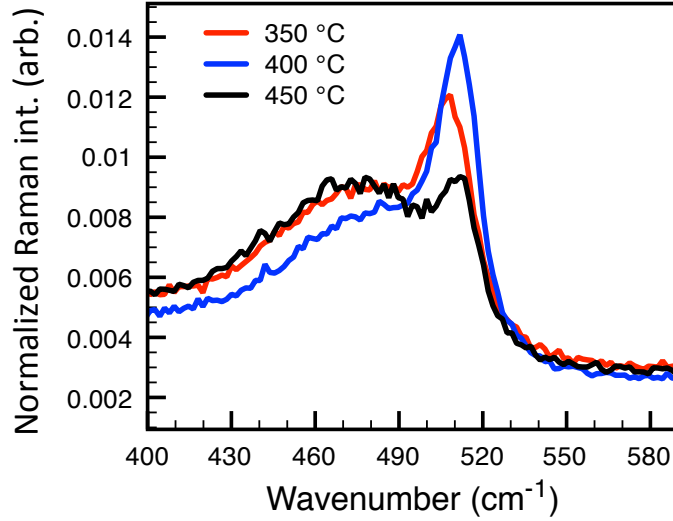


Figure 2.11. Raman spectra of PECVD films showing the change in crystalline volume fraction of $\mu\text{c-Si}$ deposited with varying values of T_{set} . The films were deposited at a pressure of 400 mTorr, with $R = 121$. The strong crystalline peak near 520 cm^{-1} indicates an optimal deposition temperature near 300 °C. The spectra are normalized to their respective integrated intensities to enable comparison.

To deposit a p-type $\mu\text{c-Si}$ emitter, we used $R = 121$, $T_{set} = 390$ °C, and total chamber pressure of 400 mTorr. These conditions yield a deposition rate of 0.5 nm min^{-1} . We performed Hall measurements on a 195 nm thick film deposited under these conditions and measured a hole carrier density of $\sim 3 \times 10^{19}\text{ cm}^{-3}$ with a resistivity $1.5\ \Omega\text{ cm}$. We tested the performance of these films by depositing them on n-type wafers (doped at $\sim 1 \times 10^{17}\text{ cm}^{-3}$) and testing V_{oc} under 1-sun illumination. In such an experiment Ga/In eutectic was scribed into the back of the wafer after film deposition and protected with Ag print to form a back contact. Front contact was made by sputtering a transparent conducting oxide (TCO), either indium doped zinc oxide (IZO) or indium doped tin oxide (ITO), through a shadow mask. Because the junction was formed across the entire sample surface, but contact was only made in isolated areas of the moderately high-resistivity emitter, these rudimentary devices

exhibited very high series resistance, preventing direct interpretation of their J-V curves. However, series resistance does not affect V_{oc} since no current flows at open circuit. Thus it is straightforward to measure the V_{oc} of these samples as a quick screening method for junction quality. Though processing of working solar cells using these PECVD films was often inconsistent due to uncontrolled contaminants present in a research laboratory environment, we were able to consistently achieve a V_{oc} above 500 mV. Prior to PECVD of the emitter, we prepared the wafer with either an RCA 1 clean (to remove organic contaminants) followed by an HF dip, or just an HF dip to remove the native oxide. The champion V_{oc} achieved under AM1.5G illumination with this process was 606.1 ± 0.7 mV, The device had a 120 nm thick PECVD emitter. For this sample, only a 30 s dip in buffered HF was used to prepare the wafer for deposition, and IZO was used for the top contact. This high V_{oc} indicates that the junction is of good quality and the emitter is functioning as intended.

2.4 Hot-wire chemical vapor deposition of crystalline silicon absorber layers

The wafering of Si for photovoltaics represents a significant production cost, with roughly half of the crystalline material present in a crystalline ingot lost during the sawing and polishing process. Because of this, there is presently intense interest in the photovoltaics industry in methods for the manufacturing of high-quality crystalline Si absorber layers without incurring the costs associated with wafering. One solution is kerf-less wafering of Si ingots with techniques such as spalling, ion-implantation and exfoliation, or epitaxial growth on porous Si and exfoliation [4]. An alternative method is based on direct thin-film deposition (similar to the manufacturing processes used in CIGS, CdTe, or thin-film amorphous and microcrystalline Si solar cells). Hot-wire chemical vapor deposition (HWCVD) has been considered as a technique to deposit crystalline Si epitaxially on a template at temperatures which enable the use of low-cost substrates such as glass [17–23].

In HWCVD, a hot filament is used to thermally decompose the process gasses

into film precursors. The technique can be used to deposit polycrystalline and amorphous Si films [34]. However the growth of epitaxial crystalline Si at low substrate temperature has also been demonstrated with this technique [20, 21, 38, 39]. In addition, high-quality Si epitaxy suitable for solar cells has been achieved at temperatures above 500 °C [19]. Though the lack of hydrogen on the growing surface at these elevated temperatures promotes high-quality crystalline growth, it prevents bulk hydrogen passivation of grain boundaries and dislocations during growth.

The phase and microstructure of the material deposited by Si HWCVD are determined by gas phase and surface chemistry and kinetics during deposition, making the process sensitive to pressure, the ratio of H_2/SiH_4 (R), and substrate temperature [18–21, 40–43]. One important feature in the low-temperature regime (< 500 °C), is that the critical epitaxial thickness that can be achieved before breakdown to twinned, polycrystalline, or amorphous growth tends to decrease with increasing temperature. This has been attributed to oxygen contamination on the growth surface that is prevented by surface hydrogenation at low temperature [18, 21, 42]. Another important growth mechanism is that atomic hydrogen etches amorphous and strained Si-Si bonds, promoting the crystalline phase [34, 44].

The implementation of HWCVD used here is illustrated in Figure 2.12. The chamber is identical to that used for PECVD, with the exception that a hot-wire assembly (instead of an RF electrode) is placed below the substrate. As described in Section 2.3, R describes the flow ratio of H_2 to SiH_4 and T_{set} indicates the substrate heater set point. We used a DC current to resistively heat two tungsten wires of 0.5 mm diameter, and monitored their temperature with optical pyrometry. In this work a wire temperature of 1900 °C was used. The wires were used either straight, or coiled to increase the deposition rate. The process gasses were H_2 and 5% SiH_4 in Ar with 5 ppm PH_3 .

Here we consider epitaxial growth of Si solar cell absorber layers at low temperature with HWCVD. The use of low substrate temperatures (< 500 °C), enables the use of low-cost substrates such as soda lime glass and offers the possibility that H can be incorporated into the film to passivate dangling Si bonds and improve car-

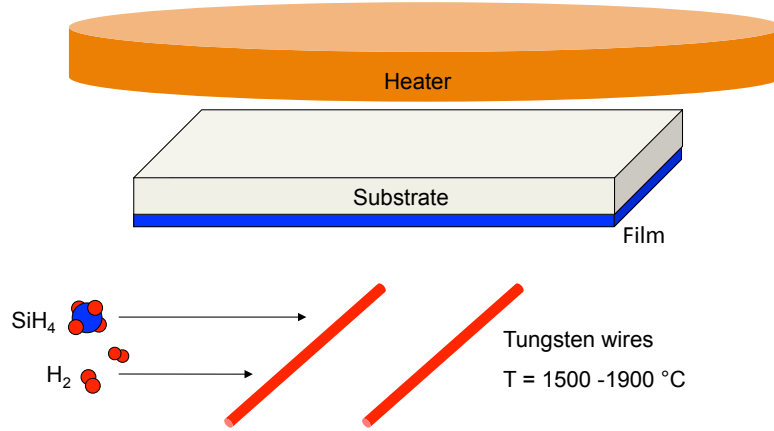


Figure 2.12. Schematic of the HWCVD technique. SiH_4 , and H_2 are dissociated by resistively heated tungsten wires into growth precursors for silicon thin-film deposition. Crystalline silicon can be grown epitaxially with this method under certain processing conditions.

rier lifetime. Previous work has shown that post-deposition oxidation of surfaces in porous Si HWCVD films severely limits photovoltaic performance [20]. Therefore we target dense epitaxial growth. Though the ultimate goal was to use HWCVD to grow absorber layers on thin-film polycrystalline templates, we studied films deposited on (1 0 0) heavily doped n-type (n+) Si wafers to study the material properties of the HWCVD films without potential complications from growth on an imperfect template.

2.4.1 Achieving dense crystalline growth

This section focuses on evaluating the performance of epitaxial Si films grown at low substrate temperature with HWCVD. Though the physical mechanisms governing HWCVD have been previously studied [18–21, 40–43], empirical process tuning was necessary to achieve the dense epitaxial microstructure which is the subject of this work.

Unsuitable processing conditions led to highly-structured, fine-grain polycrystalline growth as shown in Figure 2.13. The films shown in Figure 2.13 was deposited for 180 minutes using straight wires at $R = 200$, $T_{set} = 390$ °C (a) or 450 °C (b), and a total pressure of 120 mTorr. We found that a reduction in the chamber pressure to

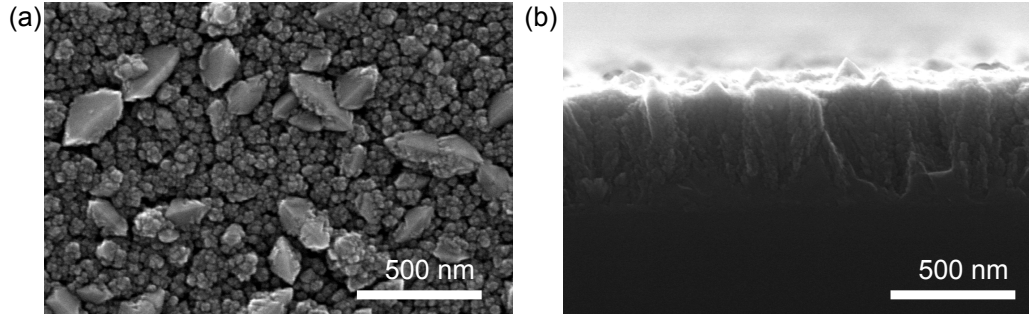


Figure 2.13. Scanning electron micrographs of polycrystalline films deposited by HWCVD for 180 minutes using straight wires at $R = 200$ and a total pressure of 120 mTorr. (a) is a plan view of the film surface for a film deposited at $T_{set} = 390$ °C. (b) is a cross-sectional image taken along a cleaved edge of the substrate for a film deposited at $T_{set} = 450$ °C; close inspection reveals the substrate/film interface. These are examples of the microstructure observed when processing conditions were not suitable for the epitaxial growth we were targeting.

80 mTorr during growth allowed us to access the epitaxial phase as shown in Figure 2.14 (all other deposition parameters were identical to those used for the film shown in Figure 2.13a). Reflection high-energy electron diffraction (RHEED) was used post deposition to confirm that the deposited film was epitaxial. The RHEED pattern shown in Figure 2.14b indicates (1 0 0) crystalline growth [45]. The deposition rate under these conditions (80 mTorr) was approximately 1.5 nm min^{-1} as estimated from scanning electron microscopy (SEM) of a pinhole found in the film. Though this reduced growth pressure yielded epitaxial growth, longer deposition times resulted in roughening of the surface and twinned growth as shown in Figure 2.14c,d. This rough film can be expected to exhibit a high defect density and be unsuitable for solar cell applications.

We implemented cross-sectional transmission electron microscopy (XTEM) and selected area electron diffraction to further understand the evolution of the growth surface microstructure during deposition and the associated growth phase of the film. Figure 2.15ab shows the surface microstructure of two films grown under identical conditions for differing amounts of time. We observe that the surface evolves from the flake-like morphology, to a rough cauliflower-like morphology with increased growth time. Figure 2.15 shows an XTEM image and selected area diffraction patterns for the

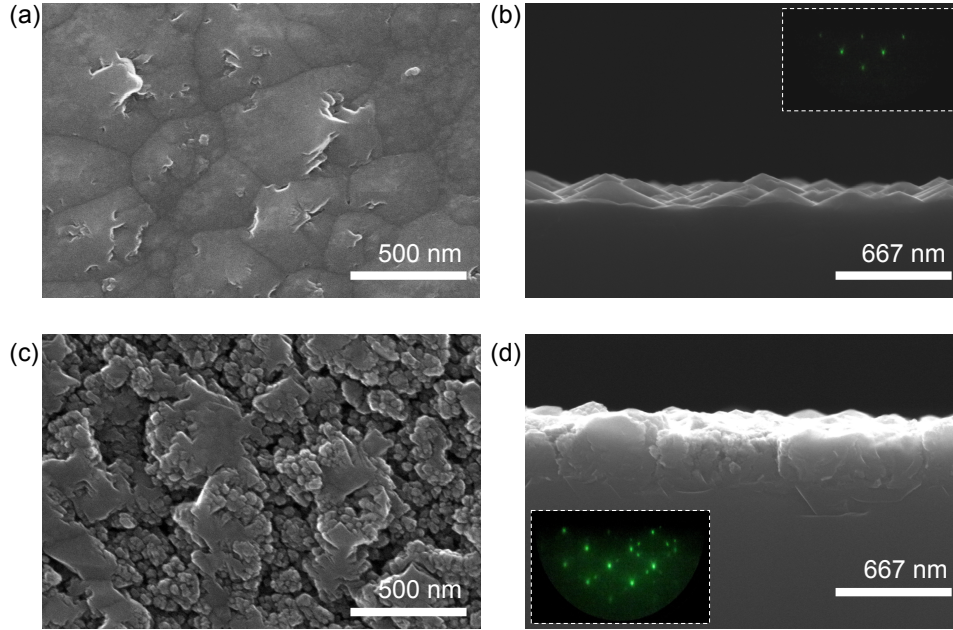


Figure 2.14. Scanning electron micrographs of two films deposited with HWCVD using straight wires at $R = 200$, $T_{set} = 390$ °C, and a total pressure of 80 mTorr. The film shown in (a) and (b) was deposited for 180 minutes, and the film in (c) and (d) was deposited for 360 min. (a) and (c) are plan view images of the film surface; (b) and (d) are cross-sectional images. The insets of (b) and (d) are post-deposition RHEED patterns of the film surface. We note that the film grown for 360 min shows breakdown to rough, twinned growth.

film pictured in Figure 2.15b. The selective area diffraction patterns shown in Figure 2.15c show that growth evolves from a twinned phase (indicated by the observation of higher-order diffraction spots) to fine-grain polycrystalline growth (indicated by the emergence of rings on the diffraction pattern).

We found that a reduction in the substrate temperature during growth mitigated roughening and breakdown of the epitaxial phase. This observation is consistent with previous work which identified reduced oxygen contamination due to increased hydrogen coverage of the growth surface as the mechanism for the observed reduction in roughening at lower temperature [18, 21, 42]. This effect is shown in Figure 2.16. Both samples were grown at 120 mTorr with $R = 371$, for 210 minutes. The increased R (relative to that used to deposit the films in Figure 2.14) was used to achieve epitaxial growth at higher chamber pressure. In addition, the film shown in Figure

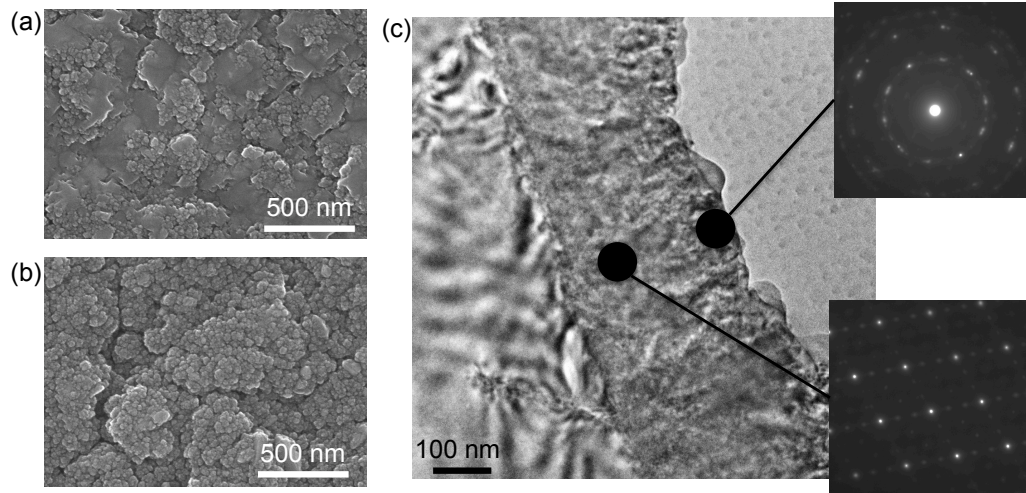


Figure 2.15. The evolution of film microstructure during HWCVD Si growth at $R = 150$, $T_{set} = 450$, and a pressure of 80 mTorr from twinned epitaxial to polycrystalline deposition. (a) and (b) show SEM images of film surfaces for deposition times of 180 min (a) and 270 min (b). (c) shows an XTEM image of the film shown in (b), along with selected area electron diffraction patterns taken from the approximate regions indicated.

2.16 was deposited using coiled hot wires, the increased surface area of the wires yielded an improved deposition rate of approximately 3.5 nm min^{-1} .

2.4.2 Process control challenges in HWCVD

Since the low-temperature HWCVD epitaxial regime is achieved under high H_2 dilution, atomic H etching of strained and amorphous Si-Si bonds is an important process to consider when optimizing the process [44]. This etching process makes film properties very sensitive to contamination and uncontrolled radical partial pressure due to etching of material from the chamber walls. This presents two challenges. The first is that it becomes difficult to control doping in the film, as doped material from previous runs may be etched from the chamber components and redeposited in the film. The second is that Si from chamber components can be abstracted back into the gas phase resulting in uncontrolled precursor partial pressures. We have observed evidence of both of these mechanisms.

After introducing a new, clean molybdenum sample carrier to the process, we

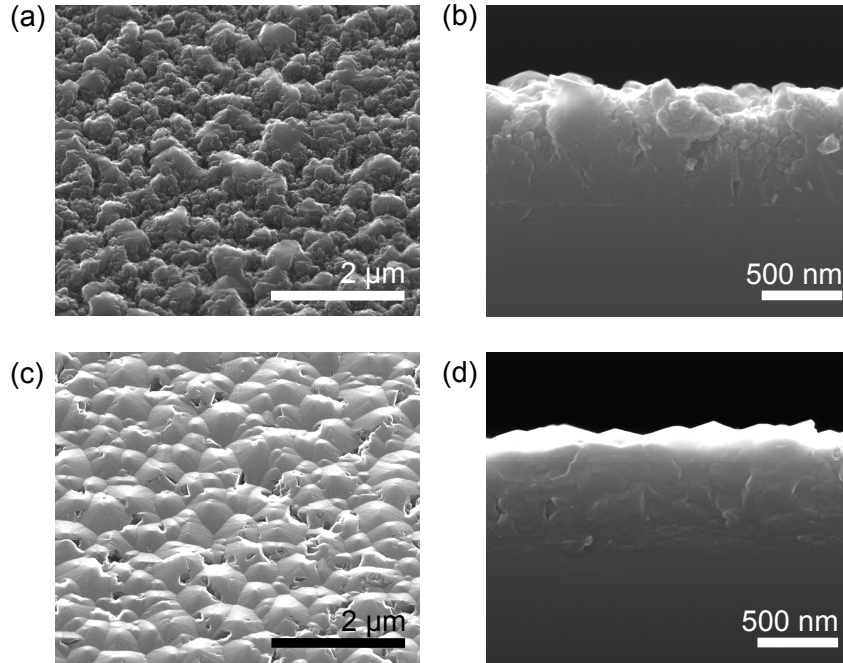


Figure 2.16. Scanning electron micrographs of HWCVD films deposited with coiled wires at 120 mTorr with $R= 371$ for 210 minutes. The film shown in (a) and (b) was deposited at $T_{set} = 450$ °C and that shown in (c) and (d) was deposited at $T_{set} = 250$ °C. The images in (a) and (c) were taken at a 45° angle from the surface, the images in (b) and (d) are cross-sectional views. We note that reduced substrate temperature yields a smoother surface microstructure.

noted a significant decrease in film deposition rate. To investigate the cause of this, we deposited a film under a standard set of conditions expected to yield epitaxial growth. A cross-sectional SEM image of this is shown in Figure 2.17a. We then ran the reactor at 120 mTorr with the wire heated to their normal process temperature of 1900 °C flowing only the SiH_4/PH_3 gas mixture (no hydrogen) for 1 hour with the sample holder and the borosilicate glass backing plates, typically placed on top of the growth substrate to help hold it in place during loading, present in the normal deposition position. We noted dark material, likely rough a-Si had accumulated on the sample holder and backing plates after this process. We then repeated a film growth under standard deposition conditions and observed a dramatic increase in the film thickness along with a change in the deposition phase from epitaxial to polycrystalline growth. Cross section and plan view SEM images of this second film are shown in

Figure 2.17bc. This result shows that the hydrogen rich processing conditions needed to achieve epitaxial growth at low temperature via etching of strained Si-Si bonds results in uncontrolled precursor partial pressure and thus inconsistent film growth highly dependent on the state of the chamber and components.

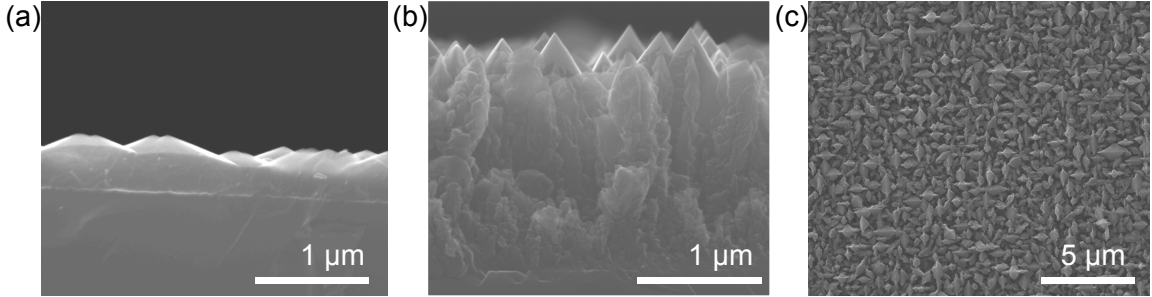


Figure 2.17. SEM images showing severe HWCVD process drift likely caused by redeposition of material from chamber components. (a) shows a cross section of an epitaxial film deposited with a new, clean substrate carrier. Note the substrate/film interface apparent in the micrograph. (b) and (c) show cross section and plan view (respectively) of a film grown under the same conditions, but immediately after a process was run on the empty sample holder while flowing only the SiH_4/PH_3 gas mixture. Both films were deposited at $R = 371$, $T_{set} = 250$ °C, at a pressure of 120 mTorr. The film in (a) was deposited for 313 minutes, and that in (b) and (c) for 296 min.

The other challenge posed by hydrogen rich deposition conditions is that contaminants may be redeposited in the film as material is etched from chamber components during deposition. This is a concern for both impurities that induce electronic defects in Si (such as metals or carbon) and for control of dopant incorporation. The chamber has historically been used for deposition of both n- and p-type material. Though it had been used for hundreds of hours for exclusively n-type deposition, we found significant boron incorporation into the films persisted. This is shown in Figure 2.18, which shows secondary ion mass spectroscopy (SIMS) analysis (performed by Evans Analytical Group) of an epitaxial HWCVD film. The film was also deposited on a silicon on insulator (SOI) substrate and Hall measurements were performed. Hall measurements on the 1 μm thick n-type SOI device layer indicated an electron concentration of $2.97 \pm 0.04 \times 10^{14} \text{ cm}^{-3}$ with a mobility of $5.3 \pm 0.7 \text{ cm}^2 \times 10^2 \text{ V}^{-1}$

s^{-1} . Hall data for this bi-layer system in which the properties of one layer (the SOI substrate) were known, was interpreted as described in [46] to extract the properties of the HWCVD-grown layer. The results are shown in Table 2.1 (sample A).

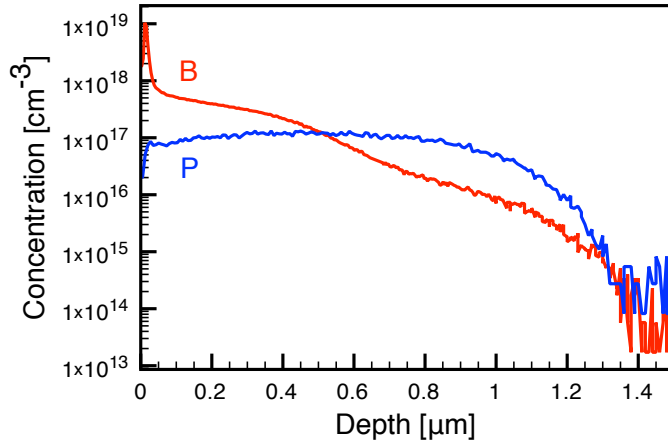


Figure 2.18. SIMS profiles on epitaxial HWCVD film showing phosphorus and boron concentrations. Hall data for a sample from the same deposition run is given in the first entry in Table 2.1. The film was grown at $R = 323$, 120 mTorr, $T_{set} = 250$ °C for 480 min. The sample for this SIMS profile was deposited on an heavily antimony doped Si substrate.

Table 2.1. Hall measurement results for epitaxial HWCVD films. Four point contacts were made by thermally evaporating ~ 200 nm of Al through a shadow mask. All films were grown with $T_{set} = 250$ °C, at a total pressure of 120 mTorr. Sample A was deposited prior to cleaning of the chamber components while B, C and D were deposited after cleaning.

Sample	R (H_2/SiH_4)	Growth Rate ($nm\ min^{-1}$)	n (cm^{-3})	μ_n ($cm^2\ V^{-1}\ s^{-1}$)
A	323	2.7	$4.50 \pm 0.04 \times 10^{15}$	$2.83 \pm 0.02 \times 10^2$
B	370	1.6	$3.700 \pm 0.006 \times 10^{16}$	$2.022 \pm 0.003 \times 10^2$
C	400	1.2	$2.557 \pm 0.002 \times 10^{16}$	$2.583 \pm 0.002 \times 10^2$
D	370	1.5	$4.75 \pm 0.06 \times 10^{16}$	$1.72 \pm 0.02 \times 10^2$

^CNo PH_3 in process gas / No glass backing; ^DNo glass backing

In order to address this uncontrolled dopant incorporation we disassembled all the internal chamber components and had them professionally cleaned. The removed components are shown prior to cleaning in Figure 2.19. After cleaning, the boron contamination persisted but was reduced as shown in Figure 2.20. However, the electron density as measured by Hall measurements increased an order of magnitude as shown in Table 2.1 (samples B, C, D). It was also postulated that boron from the borosilicate glass used to back the Si substrate during growth was contributing to contamination, however removing the backing pieces did not significantly alter the observed electron concentration (Table 2.1, samples C and D). Although the doping is difficult to control, the results in Table 2.1 show that we were able to consistently dope the film n-type in the 10^{16} cm^{-3} regime, which is a reasonable doping level for an n-type absorber layer. It is also worth noting that on a subsequent deposition during which no additional PH_3 was introduced to the chamber (Table 2.1, sample C) the carrier density was measured to stay above 10^{16} cm^{-3} . This highlights the difficulty in controlling dopant and contaminant incorporation during low-temperature epitaxial HWCVD growth. One possibility to mitigate this problem would be to clean the chamber between uses. However, it is important to note that many perfluorinated gasses (i.e., NF_3 , CF_4 , and SF_6) used for cleaning deposition chambers are high-impact global warming gasses [47].

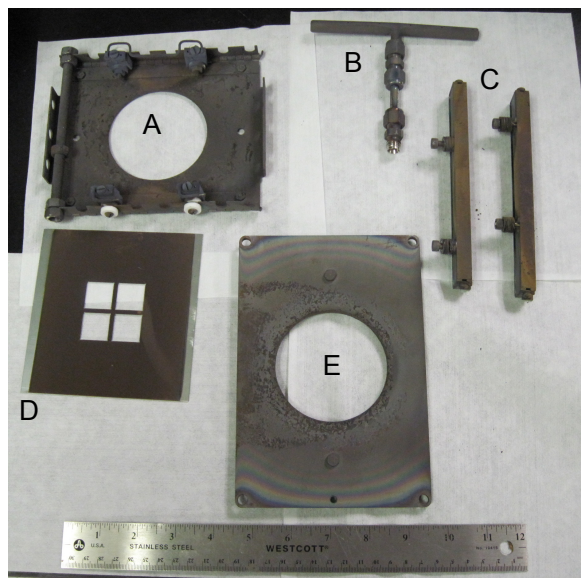


Figure 2.19. Removable components of the HWCVD chamber which were professionally cleaned to mitigate contamination from material etching and redeposition. A: the hot-wire assembly used to hold and make electrical contact to the tungsten wires. B: The gas inlet. C: Sample holder rails which support the sample holder in the chamber. D: Mo sample holder, dark deposited material is visible noting the contrast near the edges, where the holder is in contact with the support rails. E: Support plate for the hot-wire assembly.

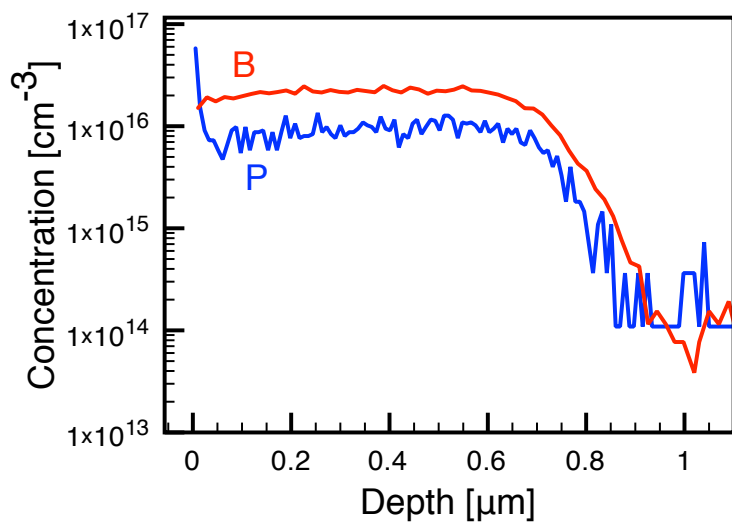


Figure 2.20. SIMS profiles of an epitaxial grown HWCVD film (Sample B in Table 2.1) showing a reduction in the boron contamination after cleaning of the chamber components.

2.4.3 Performance of compact HWCVD epitaxial Si absorber layers grown at low temperature

Ultimately, we were able to achieve stable growth in the targeted low-temperature epitaxial regime using the general processing trends discussed in Section 2.4.1 to optimize the observed microstructure and correct for process drift. An example of such a film is shown in Figure 2.21. Even with the addition of doping control as described in 2.4.2, the photovoltaic performance of these dense films as absorber layers was poor. A film was deposited under the same conditions as that shown in Figure 2.21 on an RCA1 cleaned n⁺ Si wafer for 840 minutes. A junction was then formed by depositing a PECVD emitter layer at $T_{set} = 390$ °C, 400 mTorr, $R=121$, for 120 minutes. An n-type Si wafer was included for the emitter deposition process to serve as a control against the HWCVD film. Both the n-type Si wafer and the HWCVD film were HF dipped prior to PECVD emitter deposition. After junction formation ITO was sputtered at room temperature through a shadow mask onto the PECVD layer to serve as a transparent top contact. Note that heating during ITO deposition was found to adversely affect the performance of the PECVD emitters. Back contact was formed with Ga/In eutectic and protected with conductive silver print. The control sample produced a V_{oc} of 549.7 ± 0.3 mV under AM1.5G illumination, while the HWCVD film produced a V_{oc} of 201 ± 5 mV. Using a XeF₂ etch to isolate the devices under each ITO contact pad did not measurably improve the V_{oc} .

Even though much was learned regarding the processing necessary to achieve dense epitaxial growth and repeatable n-type doping at low substrate temperature, we were not able to achieve high photovoltages with photovoltaic absorber layers deposited with this method. Here, the epitaxial phase is accessed by implementing a hydrogen rich processing environment resulting in etching of amorphous and strained bonds. Although the films were single crystal, it is possible that they exhibit a high crystallographic defect density due to limited surface mobility of film precursors at low substrate temperature. In addition the hydrogen rich processing conditions result in removal of material from the chamber and associated components which is a likely

source of impurities that would also degrade the electronic material quality. Further study on the exact nature of the defects and impurities in these materials could provide more concrete insights into the factors limiting photovoltaic performance. We note that it may be interesting to pursue applications of the optical properties of low-temperature, HWCVD-grown polycrystalline films (such as that shown in Figure 2.17bc). These films appear black by eye indicating excellent optical absorption.

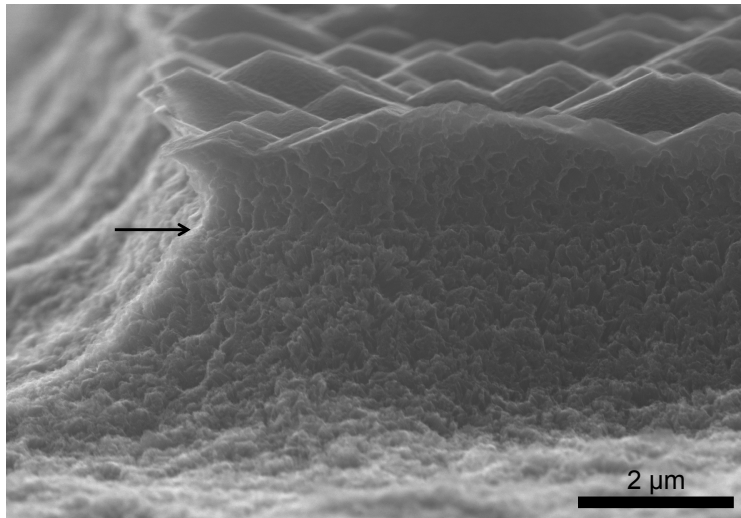


Figure 2.21. Scanning electron micrograph of a dense epitaxial HWCVD Si film growth at 120 mTorr, $T_{set} = 250$ °C, $R=371$, for 780 minutes. A region of the film was protected with photoresist, and then the sample was exposed to XeF_2 , a gaseous isotropic silicon etching agent. The pitting of the film and substrate is a result of this etch. The apparent substrate/film interface is indicated by the arrow. The growth rate was estimated to be 1.8 nm min^{-1}

2.5 Conclusion

Though significant challenges remain to the realization of efficient deposited film Si photovoltaics, the more general approach involving the use of thin (tens of μm thick) crystalline absorbers remains an important area of research and development. Promising approaches include epitaxy and lift off or kerf-less exfoliation from an ingot, for example. Since different fabrication schemes can be expected to result in materials with varying defect structure, a detailed understanding of the associated

device physics, such as that developed in this chapter, will be important in their optimization. Furthermore, high efficiency in such devices will require novel cell architectures with both robust optical design, and excellent control of surfaces. Since Si is an indirect gap semiconductor, absorption is relatively weak near its band edge making it challenging to optimize optical absorption in a thin device. Also, as the surface to volume ratio increases, well passivated surfaces become critical to maintaining high operating voltages. Thus optimization of devices based on thin c-Si absorbers will benefit from a detailed understanding of the multidimensional optoelectronic device physics in governing their operation.

Chapter 3

Device physics of silicon heterojunction solar cells

3.1 Introduction

Silicon heterojunction (SHJ) solar cells, based on a heterojunction between hydrogenated amorphous silicon (a-Si:H) and a crystalline silicon (c-Si) absorber, are a promising approach to high-efficiency silicon-based photovoltaics; they are notable for their high V_{oc} , which can exceed 720 mV [48, 49]. In their most common implementation which was pioneered by Sanyo with the heterojunction with intrinsic thin layer (HIT) cell, SHJ cells employ a thin region of intrinsic a-Si:H to passivate the c-Si surface [50, 51]. The deposition of a-Si:H at low temperature, usually via plasma-enhanced chemical vapor deposition (PECVD), benefits cell manufacturing by eliminating high temperature diffusion steps. The devices are also known to maintain their performance better than homojunction devices at elevated operating temperature, an important consideration for photovoltaic system performance in realistic operating conditions [51, 52]. In addition, this approach is considered to be an enabling technology for thin c-Si absorber designs [4]. A schematic of a typical SHJ along with band diagrams at short circuit and open circuit is shown in Figure 3.1. Note that the hole quasi-Fermi level (E_{Fp}) comes very close to the valence band edge at the junction. This indicates the near-junction region of the c-Si is in inversion, exhibiting a high concentration of holes at the surface; this inversion layer has been observed by others experimentally [53–60].

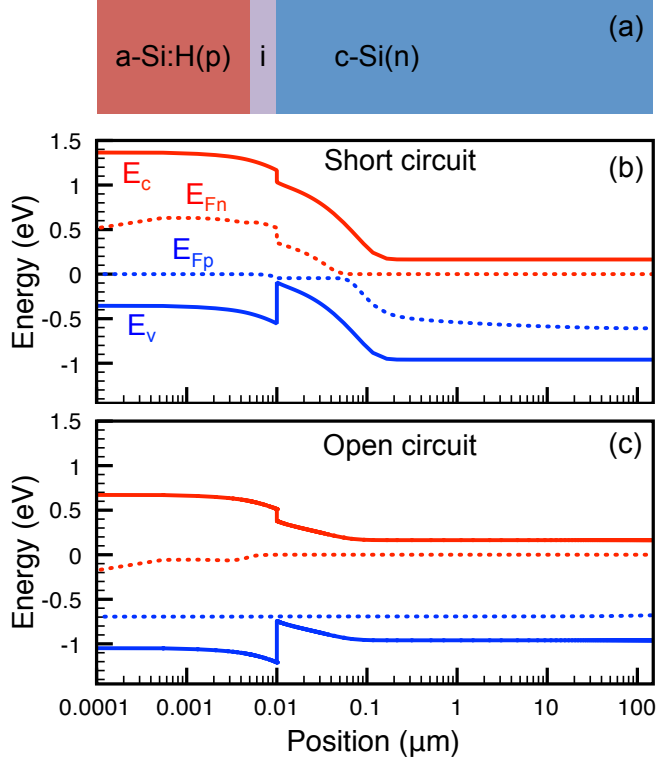


Figure 3.1. (a) Schematic of a SHJ. (b) The simulated band diagram for a SHJ at short circuit under AM1.5G illumination. (c) The simulated band diagram for a SHJ at open circuit under AM1.5G illumination. The electrical parameters are the same as those described in Section 3.4, except that the bulk lifetime in the c-Si was increased to 0.1 ms to more closely represent a high-quality Si wafer.

Although SHJ cells have demonstrated high efficiency and have been commercialized, a complete understanding of their device physics is still being developed. Currently, the most common implementation of the SHJ structure is based on a 1D structure in which layers are deposited uniformly over the entire wafer. However, more advanced next generation designs including interdigitated back contact SHJ solar cells, will benefit from improved understanding of the charge collection physics in these devices [61–66]. In Section 3.2, we present simulations which suggest that regions of epitaxy, which are known to form at the c-Si/a-Si:H interface, can induce lateral transport of photo-excited carriers near the junction. In Section 3.3, we present experimental investigations of this near-junction lateral transport mechanism, and characterize the length scale over which such transport takes place. Finally

in Section 3.4, we present simulations aimed at understanding the device physics of textured SHJ devices based on film c-Si absorbers.

3.2 Local epitaxial defects

It is well known from experiments that to optimize photovoltaic conversion efficiency of SHJ cells, care must be taken to control the a-Si:H/c-Si interfaces. Numerical modeling and experiments have shown that recombination and charging due to interface defects can degrade performance [52, 67–69]. Along with the passivation of these interface defects, it has been shown experimentally that avoiding epitaxy during the early stages of a-Si:H deposition is also critical to high performance [70–73]. It has been proposed that this is due to poor quality of the epitaxy leading to recombination. In this section we consider two-dimensional device physics simulations to study the effects of these epitaxial layers. We model devices with a defect-rich epitaxial layer covering the full wafer surface, and also those with isolated regions of epitaxy. We show that even when defect-rich epitaxy is confined to a small percentage ($\sim 5\%$) of the wafer surface, performance can be significantly degraded and we describe the device physics governing this effect. Finally, we consider the inclusion of a thin layer of low-mobility microcrystalline Si ($\mu\text{c-Si}$) to reduce lateral carrier flow toward defective pinhole regions and improve device performance.

3.2.1 Simulation details

The simulated cell is based on a 200 μm thick n-type Si wafer doped at 10^{16} cm^{-3} . The layer structure from front to back is a-Si:H(p)/a-Si:H(i)/c-Si(n)/a-Si:H(i)/a-Si:H(n) with Ohmic front and back contacts. The doped a-Si:H regions are doped at $3 \times 10^{19} \text{ cm}^{-3}$. For the basic cell, in which no epitaxy is present, all a-Si:H layers are 5 nm thick. To model the effect of partial epitaxy, an additional c-Si layer is included so the front junction layer structure is a-Si:H(p)/a-Si:H(i)/c-Si(epi)/c-Si(n), or a-Si:H(p)/c-Si:H(epi)/c-Si(n) for the cases where epitaxy extends into the emitter region. The combined thickness of the amorphous and epitaxial layers is fixed at 10 nm. The

first 5 nm of crystalline epitaxy is assumed to be intrinsic, and the additional epitaxy is doped at the same level as the a-Si:H emitter. We also consider isolated regions of epitaxy in which the epitaxial region only covers a portion of the front junction, the rest retains the a-Si:H(p)/a-Si:H(i)/c-Si(n) structure. The simulated structure is illustrated in Figure 3.2. For all results presented here the simulation region width, and thus the effective pitch between isolated epitaxial regions, is 500 nm.

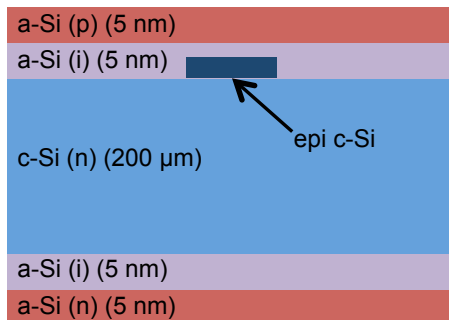


Figure 3.2. The SHJ cell structure used for device simulations. Defects are included in the epitaxial c-Si region for which the width and thickness are varied. [74]

The electrical behavior of the heterojunctions is simulated taking into account thermionic emission and tunneling at interfaces according to the Wentzel-Kramers-Brillouin (WKB) approximation as implemented in the software package Sentaurus Device based on the approach in Reference [75]. Tunneling has been shown to be an important consideration for SHJ device [68]. The electrical properties and band structure parameters for a-S:H are taken from Reference [34], with recombination in the a-Si:H regions modeled based on the explicit inclusion of band tail and Gaussian dangling bond traps according to the parameters presented in Reference [34]. Shockley-Read-Hall (SRH) recombination is assumed in the Si wafer region with electron and hole lifetimes of 100 μ s. To model the effect of defects incorporated into the c-Si epitaxial layers, we include varying densities (N_t) of mid-gap traps (both acceptor and donor) with capture cross sections of 10^{-15} cm^{-2} in the epitaxial region. The full electrostatics and recombination statistics of the traps in both the epitaxial and a-Si:H layers are included. Doping dependent mobility and Auger

recombination are also taken into account in the crystalline Si regions. Fermi statistics are implemented for the entire structure.

In order to study the effects of including a layer with reduced mobility near the front junction, we also perform calculations in which a region of $\mu\text{c-Si}$ varying in thickness from 10 nm to 100 nm is included just below the front a-Si:H / defective c-Si layer. The combined thickness of the wafer and $\mu\text{c-Si}$ is fixed at 200 μm . The electron and hole mobilities in this region are estimated to be $5 \text{ cm}^2 \text{ V}^{-1} \text{ s}^{-1}$ and $1.65 \text{ cm}^2 \text{ V}^{-1} \text{ s}^{-1}$, respectively. Recombination is included in this layer with electron and hole SRH recombination lifetimes varied from 1 ns to 100 ns. All other properties of this layer including the doping level are assumed to be the same as in the c-Si wafer.

We carry out the two-dimensional numerical simulations of these structures with a commercial device physics simulation package [33]. The carrier generation profile is calculated based on a single pass of AM1.5G illumination binned in 95 discrete wavelengths. The optical properties of a-Si:H are taken from spectroscopic ellipsometry measurements of a-Si:H films. Current density – voltage (J-V) curves are generated by varying voltage across the contacts and numerically solving the Poisson and carrier transport equations (Equations 1.8–1.12) on a finite-element mesh for each voltage.

3.2.2 Effects of defective epitaxial regions

We first consider the case in which the defect-rich epitaxial layer covers the entire wafer surface. We perform simulations for different epitaxial layer thicknesses and defect densities. Figure 3.3 shows V_{oc} as a function of epitaxial layer thickness for several values of the defect density. We find that V_{oc} is not significantly degraded until the defect density in the epitaxial layer exceeds 10^{17} cm^{-3} . We also note that as the thickness of the defective epitaxial layer increases, performance is degraded in agreement with experimental reports in the literature [70–72]. Once the defect density reaches $\sim 10^{19} \text{ cm}^{-3}$, the V_{oc} becomes severely degraded and is suppressed below 500 mV once the epitaxy extends into the doped layer.

We next explore the effects of localized epitaxy on the wafer surface. Figure

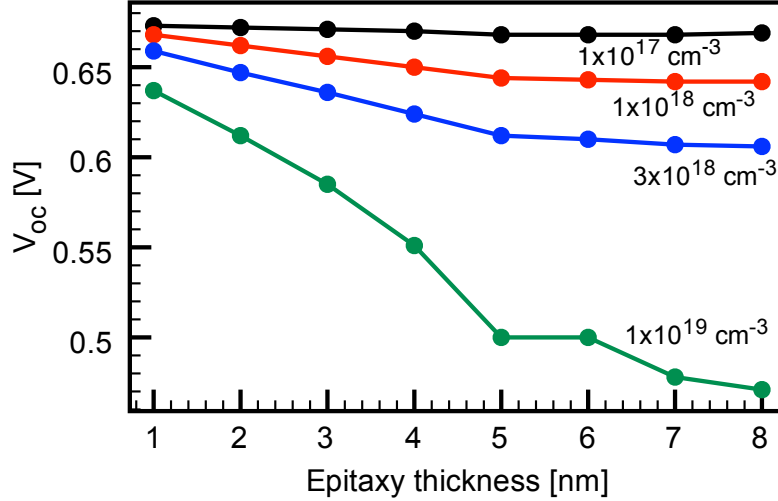


Figure 3.3. Simulated open-circuit voltage as a function of epitaxial thickness for defect-rich epitaxial layers covering the entire wafer at the front heterojunction for varying values of mid-gap trap density (as labeled) in the epitaxial layer. [74]

3.4 shows the hole (the minority carrier type in the wafer) current density at open circuit for a structure in which a 6-nm-thick epitaxial region covers 25 nm of the wafer surface. This corresponds to 5% coverage since the simulated region is 500 nm wide. Figure 3.4b shows the case in which the epitaxial region has a defect density of 10^{19} cm^{-3} , and the device achieves a V_{oc} of 588 mV, while Figure 3.4a shows the hole current density for the same geometry but with a defect-free epitaxial layer at its V_{oc} of 674 mV. We see that the open circuit condition is met in the defective case (Figure 3.4b) with holes flowing toward the front of the cell where they turn and flow along the a-Si:H/c-Si interface toward the defective epitaxial region. This is in contrast defect-free case, which exhibits a significantly lower hole current density in the wafer flowing toward the rear of the device; the direction holes would flow in a forward biased diode in the dark.

We can understand this behavior by noting that the epitaxial region provides a lower-resistance pathway for carrier collection than the thick a-Si:H regions, so carriers tend to flow through the epitaxial region. If this region is defect-rich, those carriers are subject to recombination before reaching the contact. Thus, the open circuit condition is reached at a lower voltage, even though there remains a significant flow of

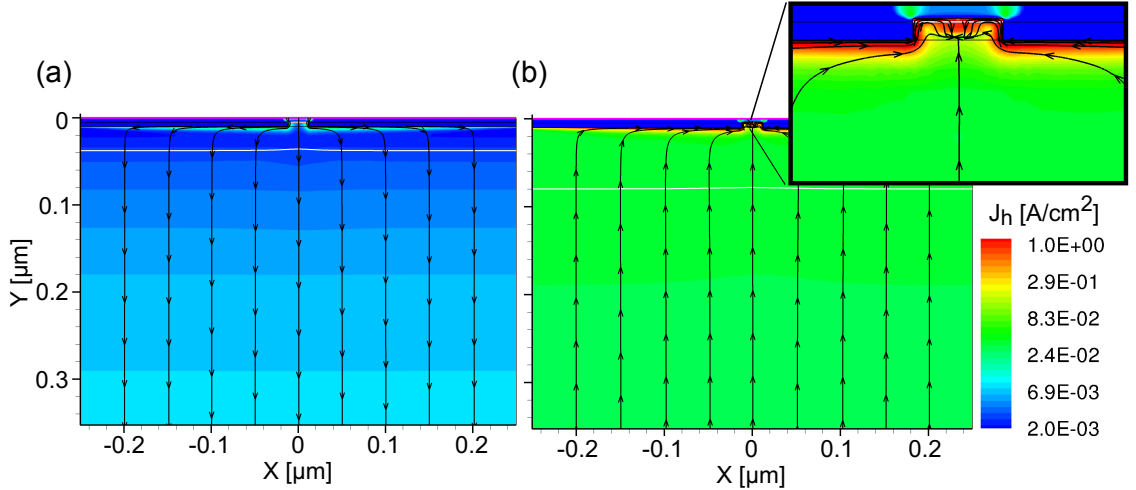


Figure 3.4. Modeling results showing the magnitude and direction of the hole current density (J_h) under illumination at open circuit at the front of the device for a 25 nm wide 6 nm thick epitaxial region for two cases: (a) mid-gap trap density in the epitaxial region of $1 \times 10^{19} \text{ cm}^{-3}$ with the inset showing a magnified view of the localized epitaxy and (b) defect-free epitaxial region. The horizontal white lines indicate the edge of the depletion region. The black lines and arrows indicate only the direction of current flow. [74]

photogenerated carriers in the wafer toward the front junction. Figure 3.4b also shows that the holes flowing toward the defective region are flowing laterally only in the near-interface region. An inversion layer of high carrier density has been experimentally observed in this region due to the band alignment of the a-Si:H/c-Si heterojunction as shown in Figure 3.1 [53–60]. Thus a small gradient in the hole quasi-Fermi level, here induced by the presence of the local epitaxy, can induce significant lateral currents. This lateral transport of photocarriers in a near-junction inversion layer is a unique feature of SHJ cells. In Section 3.3, we describe experiments characterizing the effect, and its impact on the sensitivity of SHJ to interfacial defects.

Figure 3.5 summarizes how the presence of localized defect-rich epitaxy affects cell performance across a range of parameters. Figure 3.5a illustrates that the primary effect of increasing defect density in the epitaxial region is to limit the V_{oc} . In agreement with the microscopic explanation presented above, Figure 3.5b shows that V_{oc} can be significantly degraded in the presence of highly defective epitaxy, even

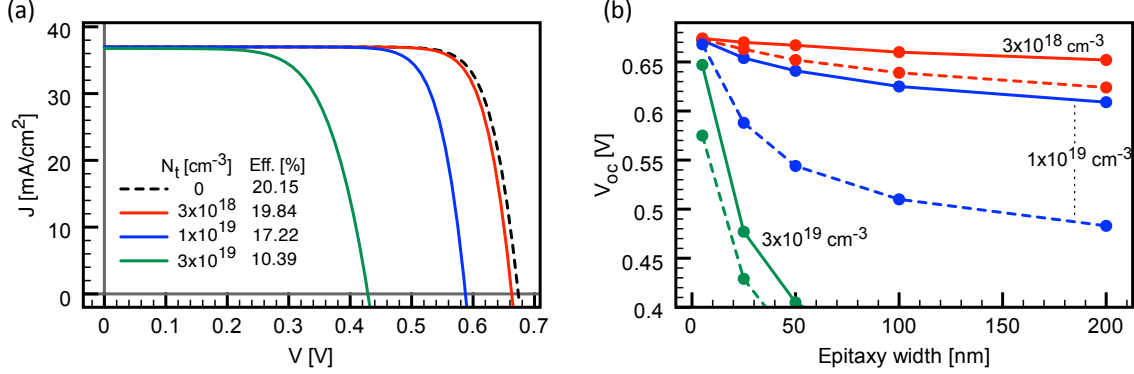


Figure 3.5. (a) Simulated current density – voltage curves and conversion efficiencies for cells with a 6 nm thick, 25 nm wide epitaxial region for changing values of mid-gap trap density (N_t) in the epitaxial region. (b) Simulated open circuit voltages under illumination as a function of epitaxy width for 3 nm (solid lines) and 6 nm (dashed lines) thick epitaxial regions for varying values of N_t as labeled and indicated by color. [74]

if the epitaxial region is confined to a small percentage of the wafer surface. The results presented in Figure 3.5b also indicate that this effect is intensified for thicker epitaxial layers. We suggest that this is due to increased carrier flow through the epitaxial region because of lower resistance in these thicker epitaxial regions than in thinner ones.

3.2.3 Reduced-mobility layers to improve efficiency

It has previously been shown using equivalent circuit modeling that increased distributed series resistance can limit the detrimental effects of spatial nonuniformities in the electrical properties of solar cells [76]. Here, the observation of lateral carrier flow in the wafer toward the defective epitaxial regions suggests that limiting the carrier mobility in the region just below the heterojunction may act to mitigate the effects of the defective epitaxial regions in a similar manner. We investigate this possibility by including a region of reduced mobility, in this case $\mu\text{-Si}$, between the wafer and the a-Si regions as illustrated in Figure 3.6a. Here, we refer to the defective crystalline regions protruding into the a-Si:H layers as pinholes, since they can no longer be understood as epitaxial with respect to the wafer. Similar approaches have

incorporated resistive nanocrystalline silicon oxide layers near contacts in thin-film Si cells to mitigate shunt pathways in aggressively textured geometries. [77, 78].

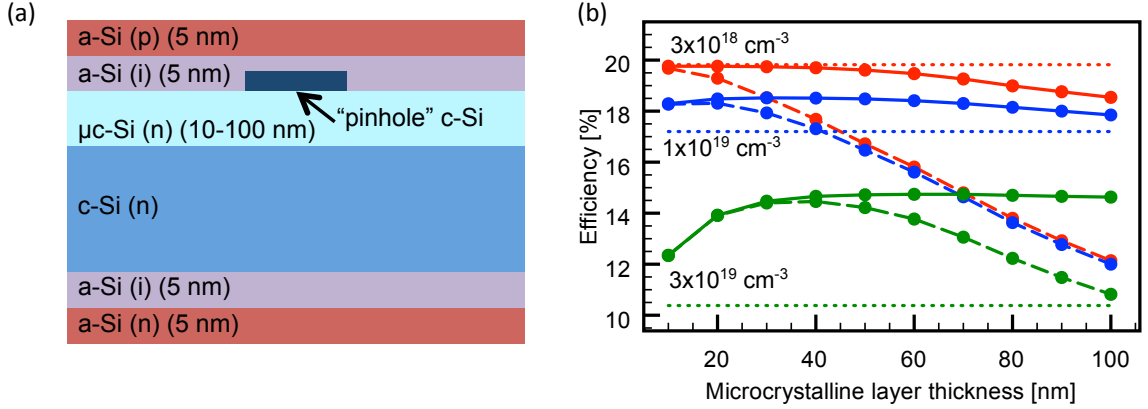


Figure 3.6. (a) The layer structure modeled when considering the use of reduced-mobility layers. The pinhole region has the same properties as the epitaxial region considered above. (b) Simulated solar conversion efficiencies for varying thickness of the $\mu\text{c-Si}$ reduced-mobility layer for three values of N_t , indicated by color as labeled. Solid and dashed lines indicate SRH lifetimes in the $\mu\text{c-Si}$ of 100 ns and 1 ns respectively. The horizontal dotted lines represent the efficiencies of devices with identical pinholes of given N_t but without a $\mu\text{c-Si}$ layer. The pinhole region is 6 nm thick and 25 nm wide. [74]

We find that in cases of moderate to high defect level within the pinhole region, the inclusion of 20 nm to 40 nm of low-mobility $\mu\text{c-Si}$ below the heterojunction can improve overall energy-conversion efficiency, even when the carrier lifetime in the $\mu\text{c-Si}$ layer is limited to 1 ns (Figure 3.6b). These improvements are substantial and exceed 4% absolute efficiency in the case of highly defective pinhole regions ($N_t = 3 \times 10^{19} \text{ cm}^{-3}$ in Figure 3.6). Care must be taken in applying this approach because the introduction of a $\mu\text{c-Si}$ layer can degrade performance in cases where the defective pinhole is not strongly degrading performance ($N_t = 3 \times 10^{18} \text{ cm}^{-3}$ in Figure 3.6b). In addition, efficiency is degraded if the reduced-mobility layer is made too thick, especially when carrier lifetime in that layer is low. It is important to note that there will be experimental challenges related to the deposition of the a-Si:H films on a $\mu\text{c-Si}$ layer. In general, the microstructure of the a-Si:H layer is coupled to the underlying substrate or $\mu\text{c-Si}$ film. However, the inclusion of such mobility limiting

layers remains a promising strategy to reduce the effects of defective pinhole-like structures in heterojunction solar cells.

3.3 Experimental characterization of lateral inversion layer transport in SHJ cells

The results in Section 3.2 indicate that the inversion layer near the junction in SHJ solar cells can mediate carrier flow to defective areas. This mechanism clarifies the physics underlying the well-known requirement that SHJ cells have a high quality a-Si:H/c-Si interface. The prevailing understanding of this sensitivity is that, for a long lifetime c-Si base passivated with a-Si:H, the length scale of sensitivity of photo carriers to defects is governed by the bulk minority carrier diffusion length. In this section, we present experimental results which support an alternate physical mechanism for this sensitivity. As the simulation results in Section 3.2 suggest, we show that the sensitivity of SHJ cells to interface quality is due in part to lateral carrier transport in the inversion layer near the a-Si:H/c-Si interface.

The collection of photo-excited holes in the base can be intuitively understood as a series of processes as illustrated in Figure 3.7. (1) Upon absorption of a photon, electron-hole pairs are excited in the c-Si(n) absorber. (2) The holes undergo minority carrier diffusion until they recombine in the bulk or reach the depletion region. (3) The built-in electrostatic field in the depletion region sweeps the holes, via drift, into the inversion layer. (4) The holes are collected from the inversion layer through the a-Si:H(i) into the a-Si:H(p) emitter where they recombine with electrons at the contact providing current to an external circuit. Note that for photons absorbed within the depletion region, the process begins at step (2). Also, carriers that are ultimately collected will, on average, only diffuse a lateral distance in the quasineutral region approximately equal to their distance from the depletion region prior to being collected via drift. The physical processes involved in (4) are not fully understood, however they likely include thermionic emission, direct tunneling, and/or trap hopping [68, 79, 80].

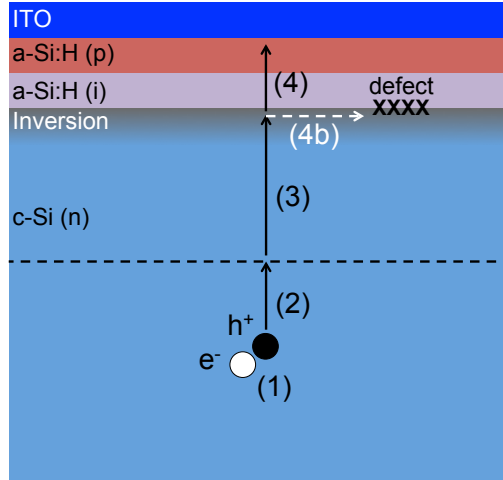


Figure 3.7. Schematic illustration of carrier collection in SHJ solar cells. (1) Electron-hole pairs are photo generated in the base. (2) Minority carriers diffuse to the depletion region. (3) The built-in electrostatic field in the depletion regions sweeps carriers via drift into the inversion layer. (4) Carriers are collected from the inversion layer into the a-Si:H emitter. In the presence of junction defects, carriers in the inversion layer may flow laterally (4b) to the defect where they recombine preventing collection. The dashed black line indicates the depletion region edge.

3.3.1 Laser-beam-induced current imaging of defective SHJ cells

In this section, we present the results of laser-beam-induced current (LBIC) measurements designed to probe the dynamics of carrier transport which occur between step (3) and step (4) in SHJ solar cells. Our measurements support the hypothesis, illustrated by pathway (4b) in Figure 3.7, that carriers can flow laterally toward defects in the inversion layer at the a-Si:H/c-Si interface over a characteristic lateral distance prior to collection into the emitter (step (4)). This process takes place with a characteristic surface sampling length which is found to increase in forward bias indicating that carriers have an increased probability of encountering a localized recombination active defect and be lost prior to collection. Thus the experiments presented here provide physical insight into the physics underlying the sensitivity of SHJ cells to interface quality.

Our interpretation of the experiment as a probe of transport in the near-junction inversion layer is justified by the use of laser wavelengths (633 nm and 488 nm)

with relatively short absorption depths in Si, which result in photo-carrier generation near the front junction. This minimizes lateral minority carrier diffusion in the quasineutral region of the base prior to collection. We also collect LBIC data with varying wavelength and observe that our results are wavelength independent, further supporting our interpretation.

The LBIC experiment is carried out by scanning a focused laser beam over a SHJ device and using the resulting photocurrent as a function of laser position on the sample to form an image. The LBIC image thus indicates where useful photocurrent is generated in the device. In our implementation, we used a Zeiss Imager.Z2m microscope with LSM 710 and 0.25 NA objective to scan the laser beam over the sample and the resulting current signal is passed through a transimpedance amplifier with a gain of $10^5 \Omega$. The amplifier also enabled us to apply a DC bias to the device and thus collect bias dependent photocurrent maps. We carried out the LBIC experiment with laser wavelengths of both 633 nm and 488 nm. Note that because the device was placed in forward bias, the dark current flowing over the entire area of the cell competed with the local photocurrent signal, limiting the forward bias at which photocurrent could be extracted and an image could be formed. This was partially overcome by increasing the power of the laser by up to a factor of 2 in order to obtain a measurable signal for a given bias. We verified that this did not affect the shape of line profiles extracted from the LBIC images. For the purposes of this study, LBIC profiles are normalized such that they converge to a maximum value of unity far from any defective area.

To probe the lateral transport of carries, we performed the LBIC measurement on a SHJ cell with localized intentionally induced defects in the heterojunction. The cells were fabricated by collaborators at École Polytechnique Fédérale de Lausanne using processes described in detail elsewhere [81–83]. Briefly, a-Si:H layers were deposited via plasma-enhanced chemical vapor deposition onto polished n-type float-zone wafers ((100) oriented, 280 μm thick, with a resistivity of 4 $\Omega \text{ cm}$) after removing the native oxide in hydrofluoric acid. An intrinsic/p-type a-Si:H stack was deposited on the front side to collect holes, and an intrinsic/n-type a-Si:H stack approximately 15 nm

thick was deposited on the rear side to collect electrons. To form the contacts, ITO was sputtered onto both sides of the wafers. In keeping with previous optimization [83], the target thickness and sheet resistance were 70 nm and 100 Ω/sq for the front ITO layer, and 150 nm and $> 500 \Omega/\text{sq}$ for the rear. A silver layer was then sputtered over the rear ITO layer, and a silver grid was screen printed on the front contact to finish the cells.

The defects were created by irradiating a target area of the device with a 30 keV focused ion beam (FIB) of Ga ions. The irradiation was carried out for varying ion doses between 6×10^{12} and 6×10^{13} ions cm^{-2} over a $43 \mu\text{m} \times 50 \mu\text{m}$ area of the cell through the front ITO contact, avoiding the contact grid. We note that in this application, the ion beam does not remove a significant amount of material as in typical applications of the FIB milling technique. Instead, we observed local performance degradation in SHJ devices after irradiation of the ITO top contact under typical FIB imaging conditions. We attribute the observed reduction in photocurrent to damage to the junction caused by atoms scattered from the ITO layer. This is confirmed by Monte Carlo simulations [84] of Ga ions impinging on a 70 nm thick ITO layer on Si, which indicated that while negligibly few Ga ions would be expected to penetrate the full thickness of the ITO layer, forward scattered In, Sn, and O atoms reach the Si region. The advantage of inducing a defect of known size and location is that it can be used to probe the device physics in the pristine regions of the device immediately surrounding it.

Figure 3.8ab show examples of the LBIC images collected for the defect which was created with a dose of 6×10^{13} ions cm^{-2} . The white box in Figure 3.8b, shows the location of the FIB induced defect. Comparison of Figure 3.8ab shows that as the forward bias is increased, the lateral influence of the defective region increases, thus increasing the effective cross-sectional area of the defect. Note that the images in Figure 3.8ab were taken at different laser powers and are not normalized, thus the absolute magnitude of the current signal in the two images is not directly comparable; recall that the DC offset to the LBIC signal due to the cell dark current also increases at forward bias. The increasing effective cross-sectional area of the defective region

in forward bias is further characterized in Figure 3.8c, which shows profiles of the LBIC images taken along the dotted white line indicated in Figure 3.8b, with 0 corresponding to the edge of the ion irradiated region.

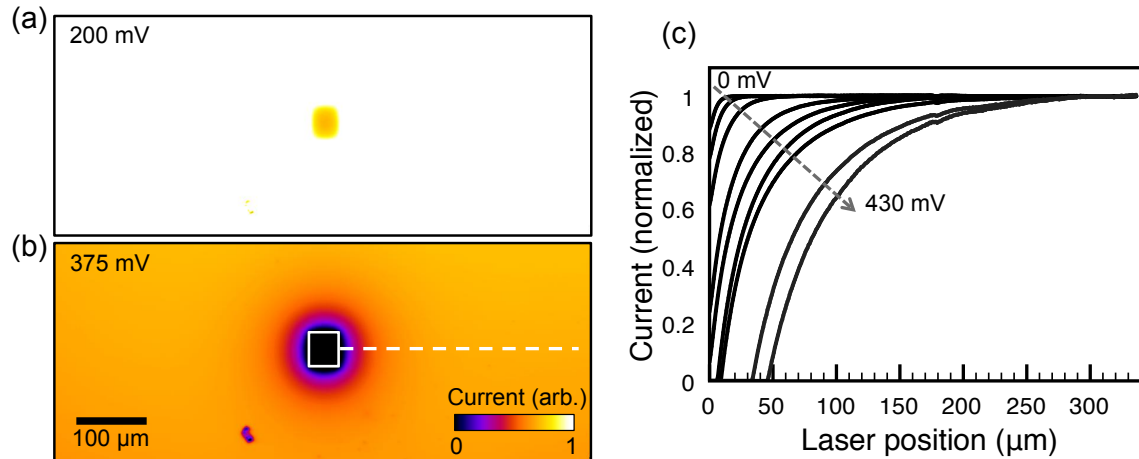


Figure 3.8. Laser-beam-induced current measurements for a laser wavelength of 633 nm near junction defects in a SHJ solar cell. The region indicated by the white box in (b) was irradiated with a dose of 6×10^{13} Ga ions cm^{-2} . (a) Shows the LBIC map for a bias voltage of 200 mV. (b) Shows the LBIC map around the same defect when the cell is forward biased by 375 mV. Note the data in (a) and (b) were taken under different laser intensities. (c) Shows normalized line profiles taken along the dashed white line shown in (b) for bias voltages of 0, 100, 200, 300, 350, 375, 400, 425, and 430 mV. [85]

The change in y-intercept for the profiles shown Figure 3.8c indicates that as the forward bias increases, the recombination activity of the defective region increases. This can be understood by noting that, as the device is forward biased, the electron concentration in the junction region increases by several orders of magnitude as shown by the changing position of E_{Fn} in Figure 3.1bc. This induces a similarly large increase in the recombination activity of any defects in that region according to Shockley Read Hall recombination statistics [22].

We also observe, as shown in Figure 3.8, that as forward bias is increased, the effective region over which the defect reduces carrier collection increases. We attribute this to an increase in the average length along the a-Si:H/c-Si interface that a hole can traverse prior to collection out of the inversion layer. Due to the high density of holes

present at the interface, significant lateral currents can be induced by small lateral gradients in the hole quasi-Fermi level. This is evident from Equation 3.1, the general expression for the hole current density accounting for both drift and diffusion, where μ_p is the hole mobility, p is the hole concentration, and E_{Fp} is the hole quasi-Fermi energy.

$$\vec{J}_p = \mu_p p \vec{\nabla} E_{Fp} \quad (3.1)$$

In this experiment, the gradient in the hole quasi-Fermi level is induced by the ion-irradiated defective region. Carriers can participate in this lateral conduction until they are either collected into the emitter contributing to the measured photocurrent or lost to other recombination processes along the pristine interface. This characteristic length is reflected in the shape of the LBIC profiles shown in Figure 3.8c.

We quantify the characteristic distance over which holes are sensitive to the defect by fitting the normalized LBIC profiles to a simple exponential function:

$$1 - Ae^{-\frac{x}{L_h}}, \quad (3.2)$$

which yields excellent fits to the data. Here the parameter A is included to account for the fact that at changing bias, the y-intercept of the LBIC profile changes. Note that a negative y-intercept is possible at forward bias when there is not enough photocurrent to overcome the forward bias dark current of the device. The parameter of greatest interest however is L_h which corresponds to the distance from the defect edge that the photocurrent recovers to $1 - \frac{1}{e}$ of its value far from the defect relative to its value at the edge of the defective region. L_h is thus interpreted as the characteristic length scale over which holes in the inversion layer are sensitive to interface defects. Note that since hole transport in the inversion layer is a combination of drift and diffusion, L_h , cannot be interpreted as a diffusion length.

Figure 3.9 shows how L_h changes with forward cell bias for three different defective region ion doses. We note the general agreement between values of L_h for the three different ion doses supporting our interpretation of L_h as a general parameter

characterizing lateral hole transport length in pristine regions of the cell. We observe that L_h increases as forward bias is increased. This is consistent with experimental observations that poor interface quality tends to adversely affect fill factor and V_{oc} [52, 70–72]. We postulate that this increase in L_h is due to a reduced carrier collection rate of holes from the inversion layer due to a reduction in the strength of the junction electric field driving collection at forward bias. This would in turn increase the characteristic distance that holes would laterally traverse in the inversion layer prior to collection. Note that we observe values for L_h exceeding 50 μm . Using the area of a circle with radius 50 μm , we estimate a tolerable surface density of defects $\sim 10^4 \text{ cm}^{-2}$. The ultimate impact of defects at any surface density on overall device performance will also be dependent on the capture cross section and associated recombination activity of the defect itself. Due to the experimental limitations discussed above, that the laser generated current must be larger than the forward bias dark current over the entire device area, we were not able to make measurements beyond 430 mV in forward bias, and L_h is expected to increase even further at higher biases.

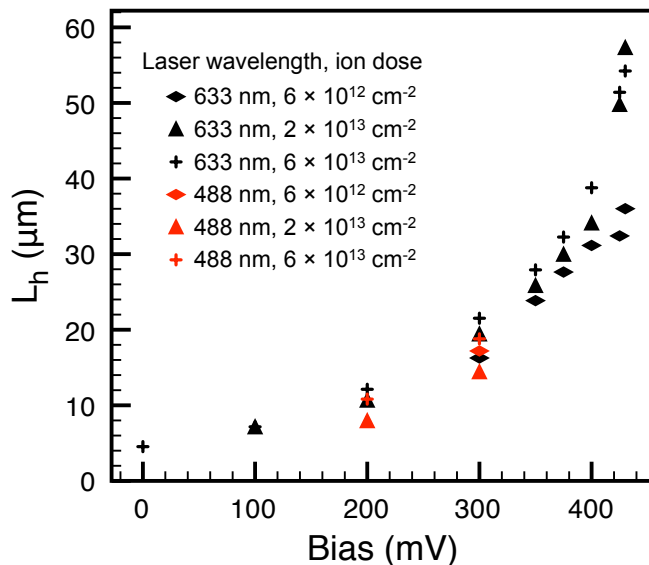


Figure 3.9. The characteristic length scale (L_h) over which holes in the inversion layer are lost to recombination in a nearby junction defect. The values were extracted from line scans such as those shown in Figure 3.8c for LBIC maps formed with both 633 nm and 488 nm laser wavelength, varying applied forward bias, and different ion doses. [85]

A key point in the physical interpretation of our experiment and results is that the lateral transport mechanism occurs primarily in the inversion layer. This is supported by the agreement between the values of L_h measured with laser wavelengths of 488 nm and 633 nm as shown in Figure 3.9. The Beer-Lambert absorption lengths for Si at these wavelengths are 0.8 μm and 3 μm respectively [86], thus the fraction of photocurrent generated in and near the depletion region changes significantly for the two wavelengths, however this does not correspond to a significant change in the measured lateral hole transport length, L_h . Thus we conclude that the device physics governing L_h are dominated by carrier dynamics occurring after photogenerated holes enter the depletion region and are quickly swept into the inversion layer.

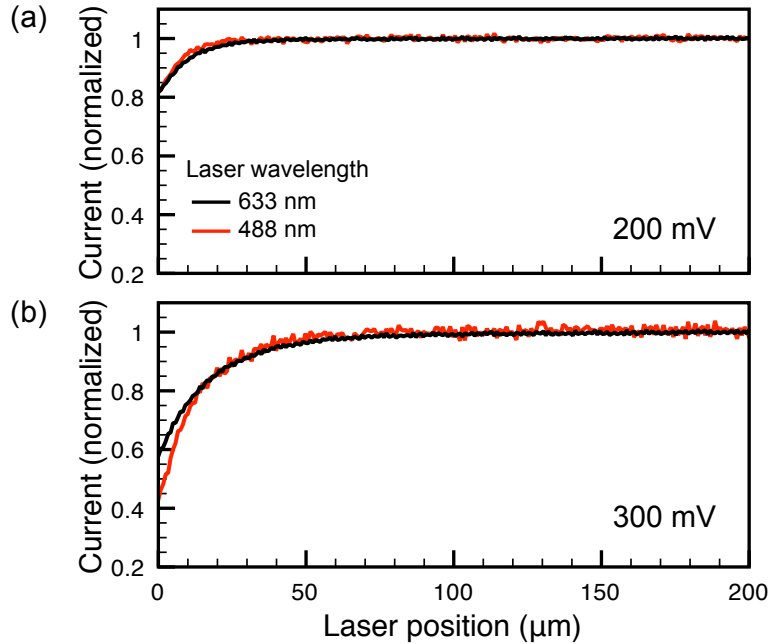


Figure 3.10. LBIC profiles taken with laser wavelengths of 488 nm and 633 nm for forward biases of (a) 200 mV and (b) 300 mV. The ion dose to the defective region was $2 \times 10^{15} \text{ cm}^{-2}$. [85]

Figure 3.10 further illustrates the agreement between the results obtained under varying laser wavelength. We note the change in y-intercept in Figure 3.10b, which we attribute to increased sampling of the defective near-surface region of the wafer at shorter wavelengths when the laser is directly illuminating the defective region. Also,

note that both wavelengths have relatively short absorption depths. Thus, even as the depletion region shrinks in forward bias, carriers do not have to diffuse long distances in order to be collected. Since the diffusion process is governed by random walks of individual carriers, it is expected that the carriers that are ultimately collected would typically diffuse laterally in the quasineutral region a distance roughly equivalent to their distance from the depletion edge. Thus the carriers contributing to the LBIC signal would be expected to diffuse laterally a distance of several μm or less in the quasineutral region, a distance much smaller than the length scale of the LBIC measurement (tens to hundreds of microns) as shown in Figure 3.8c.

3.3.2 White-light-biased, selected-area-illumination measurements with variable i-layer thickness

We also investigated the inversion layer lateral transport mechanism with white-light-biased, selected-area-illumination (WLB-SAL) experiments. These were carried out on SHJ structures with isolated contacts patterned over regions of variable a-Si:H(i) thickness. While the experiments described in Section 3.3.1 rely on a defective region to induce lateral transport in the inversion layer, the approach described in this section takes advantage of internal potential drops across a variable intrinsic layer thickness in the junction under bias. For a given device bias, as the intrinsic layer thickness is increased, thus increasing the width of the junction, the electrostatic field driving carrier collection out of the inversion layer is reduced [80].

The WLB-SAL experiment is illustrated schematically in Figure 3.11. In this experiment, the regions of thin a-Si:H(i) are analogous to the regions of isolated epitaxy discuss in Section 3.2 and illustrated in Figure 3.2, except that there are no additional recombination active defects associated with the thin i-layer in these experiments. The structure is illuminated with white-light bias illumination of variable intensity, producing a photovoltage in the device. A key feature of the measurement scheme is that the white-light bias maintains a uniform photovoltage over the structure, even though some regions of the surface are not directly contacted. During the measurement itself, the “upper” and “lower” contacts are maintained at

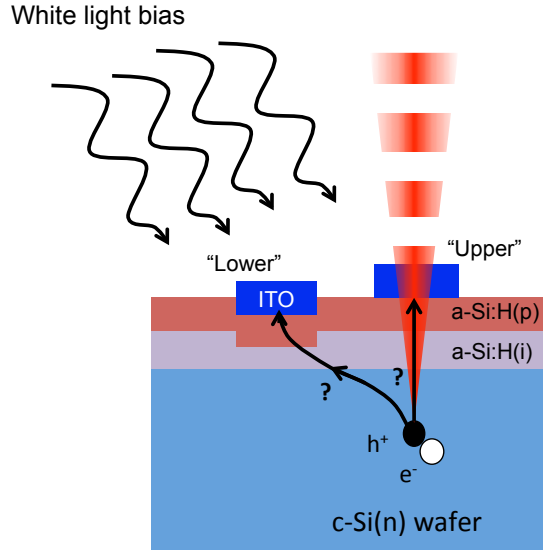


Figure 3.11. Schematic illustration of the white-light-biased, selected-area-illumination experiment. The SHJ structure is uniformly illuminated with white light inducing a known photovoltage uniformly across the junction. A small optical excitation is then applied and the resulting photocurrent at each contact location is observed with the lock-in amplification technique.

this voltage with external voltage sources, and a small additional optical excitation is focused on the device through the “upper” contact. This excitation is chopped and the resulting photocurrent is separately measured in the “upper” and “lower” contacts with a lock-in amplifier. We use a variable intensity halogen lamp to provide the white-light bias, and a chopped 635 nm diode laser fiber-coupled into the Zeiss Imager.Z2m microscope with LSM 710 for the local excitation. As noted above, collection of the holes is expected to be driven by a stronger field under the “lower” contact, inducing lateral hole current flow. This lateral current flow can be characterized by the current splitting ratio I_{lower}/I_{total} as the distance between the contacts is varied, where I_{total} is the sum of the current collected in both contacts.

Fabrication of the experimental structure was based on several deposition and etching steps as illustrated in Figure 3.12. The a-Si:H layers were deposited by collaborators at École Polytechnique Fédérale de Lausanne (EPFL). The first step in the fabrication was to deposit 300 nm of SiO_2 via PECVD. Photolithography was then carried out with positive photoresist (S1813) to mask the SiO_2 at the position

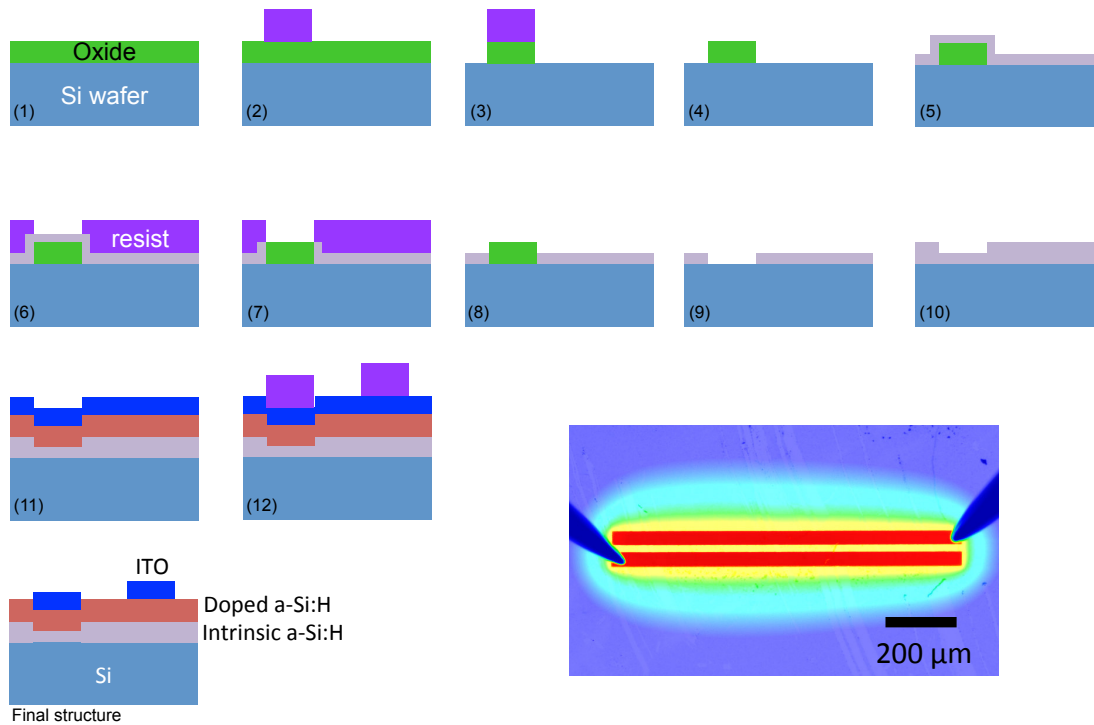


Figure 3.12. Illustration of the fabrication steps for the SHJ cells studied with the WLB-SAL experiment. Also shown is an overlay between a scanning optical micrograph and LBIC map taken at short circuit of a finished structure, with the LBIC signal simultaneously collected from both contacts. While the schematics all show the structure in cross section, the LBIC/optical image shows the plan view. In the LBIC color map, red the maximum signal and blue is no signal. The probe tips used to contact the structure are also visible.

of the “lower” contact. Then, a 5 nm thick initial a-Si:H(i) layer was deposited. Photolithography was again used, this time with a negative resist (AZ5214 in image reversal mode) to mask the entire sample surface except for the location of the “lower” contact. A XeF_2 etch (a non-plasma dry isotropic Si etch) was carried out for 10 s at 2000 mTorr to remove the small region of a-Si:H on top of the oxide. The oxide was then removed with an HF etch and the photoresist was removed with acetone. To ensure a high-quality interface for subsequent PECVD steps, the samples were cleaned in an oxygen plasma for 9 minutes at 300 mTorr. This step is expected to result in a thin oxide layer on the a-Si:H which was then removed with a brief HF dip immediately prior to the subsequent a-Si:H layer deposition. A second a-Si:H

layer of thickness 5 nm was then deposited immediately followed by a 5 nm a-Si:H(p) emitter and sputtered ITO top contact. A positive resist photolithography process was then used to mask the contact regions, and a 35 second 2:1 H₂O:HCl etch used to remove the ITO from the non-contact regions. Finally, the remaining photoresist was removed from the contacts with acetone. Control structures in which the a-Si:H(i) layer is uniformly 10 nm thick were also fabricated simultaneously on the same wafer with the use of a modified photolithography pattern which does not mask the initial SiO₂ layer. The width of the contacts was 80 μm and the pitch was varied.

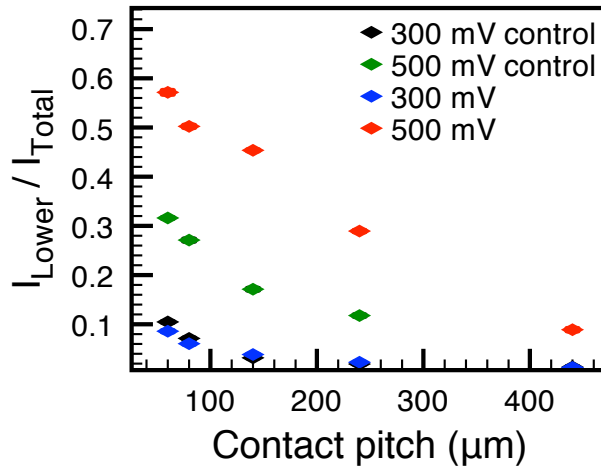


Figure 3.13. The current splitting ratio observed for changing contact pitch in the WLB-SAL experiment for white-light photovoltages of 300 mV and 500 mV. The control structure is one in which the a-Si:H(i) is uniformly 10 nm thick. Lateral transport is observed to increase at higher forward bias (500 mV).

The results from the WLB-SAL experiment are shown in Figure 3.13. At 300 mV white-light bias, the current splitting ratio is low, and there is little difference between the control and experimental case. This indicates minimal lateral transport to the “lower” contact from the location of the optical excitation under the “upper” contact. However, when the white-light-induced photovoltage is increased to 500 mV, we see a significant increase in the current splitting fraction for both the control and experimental samples, indicating a significant number of carriers are traveling laterally and being collected in the “lower” contact. Note that in the control case,

both contacts are in fact over the same 10 nm thick a-Si:H(i) layer. At 500 mV, the current splitting ratio in the experimental structure is much higher than in the control. We attribute this to the increased collection field under the “lower” contact, driving more rapid hole collection and inducing a lateral flow of carriers toward the “lower” contact region of the junction. Also note that more than half of the photocurrent is actually collected at the “lower” contact for closely spaced contacts. The 500 mV control case indicates that even in the absence of a non-uniformity in the junction itself, carriers tend to sample an increased area of the junction at higher forward bias. These results are consistent with our interpretation of the results described in section 3.3.1. Both the LBIC and WLB-SAL experiments show that as the bias is increased, the characteristic length scale that carriers can traverse in the inversion layer prior to collection increases.

The modeling results presented in Section 3.2 and the experimental results described in Section 3.3, both show that lateral charge transport in the inversion layer at an a-Si:H/c-Si heterojunction is an important mechanism to consider in SHJ cells. While holes dwell in the inversion layer prior to collection, they may diffuse or drift laterally for tens of microns. The proposed lateral transport mechanism partially explains the well-known requirement that the junction interface be high quality. Because significant currents can be induced in the inversion layer by small gradients in quasi-Fermi level, carriers can easily flow to defect sites and recombine. It is important to note that under one-sun illumination which includes near-band-gap photons, carriers will be generated throughout the absorber and lateral diffusion in the quasi-neutral region will also be an important transport mechanism. The bias dependence of our results below the maximum power point suggest that high-quality interfaces are important not just for high V_{oc} , but also for optimum fill factor, and demonstrates that controlling surface quality is important for full optimization of the current-voltage behavior of SHJ cells.

3.4 Pyramidal structuring of film-silicon-based heterojunction cells

Beyond their applications in wafer-based devices, heterojunctions formed between a-Si:H and c-Si are an enabling technology for film crystalline or thin kerf-less wafer silicon solar cells [4]. This is due to the excellent surface passivation of the a-Si:H(i) on the wafer surface, which becomes more important as the surface to volume ratio increases in thin devices. In this section we consider the device physics of HIT junctions formed on a film c-Si absorber which has been textured to improve its light-trapping characteristics [23]. The devices considered here are based on c-Si absorber layers grown via HWCVD by collaborators at the National Renewable Energy Laboratory (NREL). The approach they implement is similar to that described in Chapter 2, however the deposition is carried out at higher substrate temperature [19, 22, 23]. In addition, instead of forming the junction with a microcrystalline emitter, a-Si:H is used forming a SHJ structure.

While pyramidal texturing achieved with an anisotropic potassium hydroxide etch increases the J_{sc} of these devices, it has been observed to reduce their V_{oc} by tens of mV [23]. The origin of this reduction in V_{oc} is not apparent from experiments alone. One possible explanation is that it is a feature of the fundamental device physics associated with the geometry of a heterojunction formed on a thin crystalline layer in which the pyramid depth is comparable to the film thickness. An alternative explanation is that texturing the surface complicates the fabrication process and results in more surface defects at the junction, possibly due to the inclusion of voids at the peaks or valleys with a-Si:H. In order to identify which of these explanations is applicable, we carry out 2D optoelectronic simulations of the structures assuming that the heterojunction itself remains high quality.

The electrical parameters used for simulation are based on parameters implemented at NREL in 1D AFORS-HET simulations to model the performance of an experimental device grown via HWCVD [22]. In this study we carried out the 2D electrical simulations using Synopsys TCAD with Sentaurus Device [33]. The basic

Table 3.1. Basic a-Si:H electrical parameters used for pyramidal SHJ cell simulations

Dielectric constant	11.9
Band gap	1.72 eV
Electron affinity	3.94 eV
Effective density of states (CB)	$1 \times 10^{20} \text{ cm}^{-3}$
Effective density of states (VB)	$1 \times 10^{20} \text{ cm}^{-3}$
Mobility (electron, hole)	$20 \text{ cm}^2 \text{ V}^{-1} \text{ s}^{-1}$, $5 \text{ cm}^2 \text{ V}^{-1} \text{ s}^{-1}$
Thermal velocity (electrons and holes)	$4.27 \times 10^4 \text{ cm s}^{-1}$
Acceptor concentration (p-layer)	$1 \times 10^{19} \text{ cm}^{-3}$

a-Si:H parameters used for this study are given in Table 3.1. In the c-Si regions, trap mediated recombination was accounted for by specifying a bulk lifetime. The c-Si base had an active donor concentration of $5 \times 10^{16} \text{ cm}^{-3}$, bulk SRH lifetimes for both electrons and holes of $3 \times 10^{-7} \text{ s}$, an electron mobility of $300 \text{ cm}^2 \text{ V}^{-1} \text{ s}^{-1}$, and a hole mobility of $167 \text{ cm}^2 \text{ V}^{-1} \text{ s}^{-1}$. Note the absorber lifetimes are shorter than what would be expected in a high-quality wafer-based device due to the fact that the devices considered here are based on deposited film c-Si. The c-Si BSF or template layer had an active donor concentration of $2 \times 10^{19} \text{ cm}^{-3}$, the default doping dependent SRH lifetimes for electrons and holes (5×10^{-8} and $1.5 \times 10^{-9} \text{ s}$, respectively), and the default doping dependent mobilities for electrons and holes (87.47 and $67.52 \text{ cm}^2 \text{ V}^{-1} \text{ s}^{-1}$, respectively). Auger recombination was accounted for in both c-Si layers with the default parameters. The full statistics and electrostatics of trap mediated recombination were simulated in the a-Si:H regions with the trap parameters suggested by Schropp and Zeman [34]. A distributed series resistance of $2 \Omega \text{ cm}^2$ was included at the emitter contact to account for series resistance losses in a practical device. Here we used a thermionic emission model for the a-Si:H/c-Si interface and did not include a tunneling model. The layer structure of the front heterojunction was c-Si, 6 nm a-Si:H(i), 10 nm a-Si:H(p), and an 80 nm ITO top contact; all thicknesses are expressed as normal to the c-Si surface. These simulation

parameters were found to give an excellent fit to experimental data obtained by our collaborators as shown in Figure 3.14.

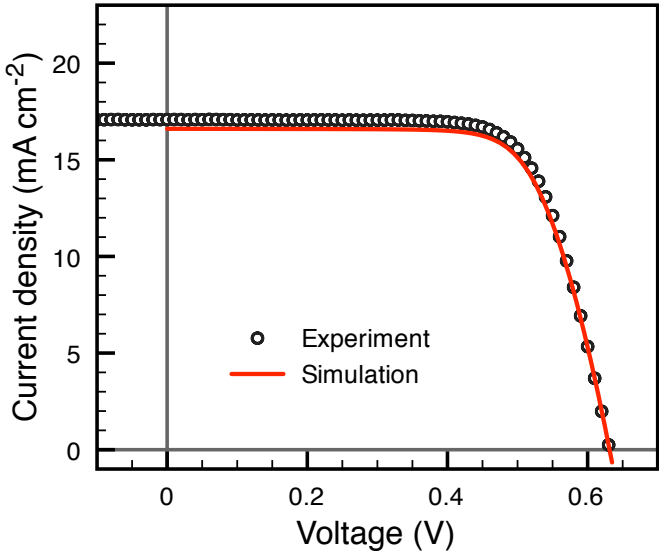


Figure 3.14. Agreement between the simulated and experimental current density – voltage curves for a planar c-Si film-based SHJ solar cell. The layer structure from top to bottom is 80 nm ITO, 10 nm a-Si:H(p) 6 nm a-Si:H(i), 3 μm c-Si base, and 200 μm BSF/template wafer. All layers are flat and the optical portion of the simulation was calculated via TMM. The simulated efficiency of the device was 7.52%

The geometry of the simulated pyramidal structure is shown in Figure 3.15. We vary the ratio between the pyramid etch depth P , and the total base thickness B . The generation rate profiles in the structures were calculated via optical FDTD simulations for wavelengths between 375 nm and 1075 nm at 50 nm increments and weighted by the AM1.5G spectrum and taken as input into the electrical simulation [87, 88]. In some instances, we imposed the assumption of uniform generation in the a-Si:H and c-Si regions to isolate the optical and electrical effects of the structure.

Figure 3.16 shows how the V_{oc} changes for changing pyramid depth (P). We observe a small increase in the V_{oc} with increasing pyramid depth. We note some variability in this trend is apparent in the one-sun simulation. We attribute this to an optical effect which varies the amount of available photocurrent. This variability

also affects the J_{sc} as shown in Figure 3.16b. When the variability is removed by uniformly scaling the optical generation rate for each structure such that they exhibit identical J_{sc} , the trend of increasing V_{oc} becomes more clear.

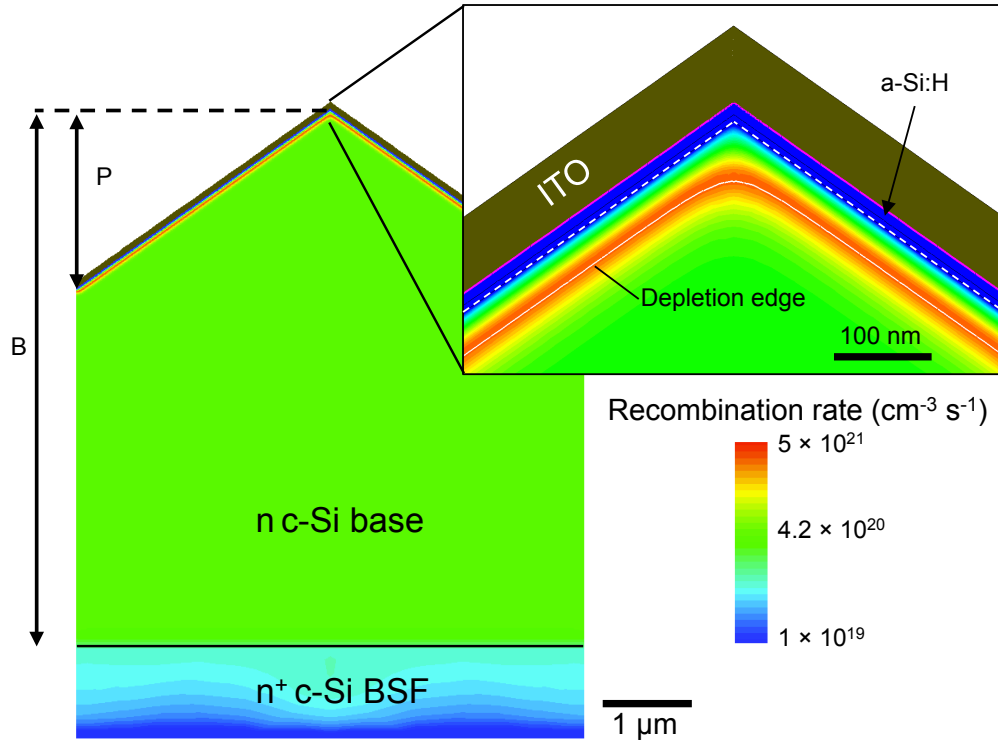


Figure 3.15. Simulated Shockley Read Hall recombination rate in the c-Si region at open circuit for a thin pyramidally structured SHJ solar cell, with a total base thickness (B) of 6 μm and a pyramid depth (P) of 2 μm . Note the SRH recombination appears as 0 in the a-Si:H regions. However, the simulated trap mediated recombination in these regions is not in fact 0, this value on the plot is an artifact of the use of explicit trap occupation simulations for the a-Si:H region and bulk SRH statistics in the c-Si region. The solid white line indicates the calculated edge of the fully depleted region around the junction. The dashed white line indicates the a-Si:H/c-Si interface.

We also consider the case, shown in Figure 3.16a in which B and P are simultaneously varied to maintain a constant average thickness for the absorber layer, which is equivalent to maintaining a constant surface/volume ratio. In this case we also use a constant uniform generation profile in the structure, chosen to yield a J_{sc} of 18.55 mA cm^{-2} . The use of a uniform generation profile completely removes any optical effects associated with the changing geometry, and allows us to investigate only

the electrical properties. In this case, where total absorber volume is held constant, we observe that V_{oc} becomes constant with the pyramid depth P . This suggests that the increase in V_{oc} with increasing pyramid depth is due to a reduction in the total bulk recombination associated with a reduced total absorber volume. In other words, we conclude that the V_{oc} is limited by bulk recombination in these shorter-lifetime film absorber devices.

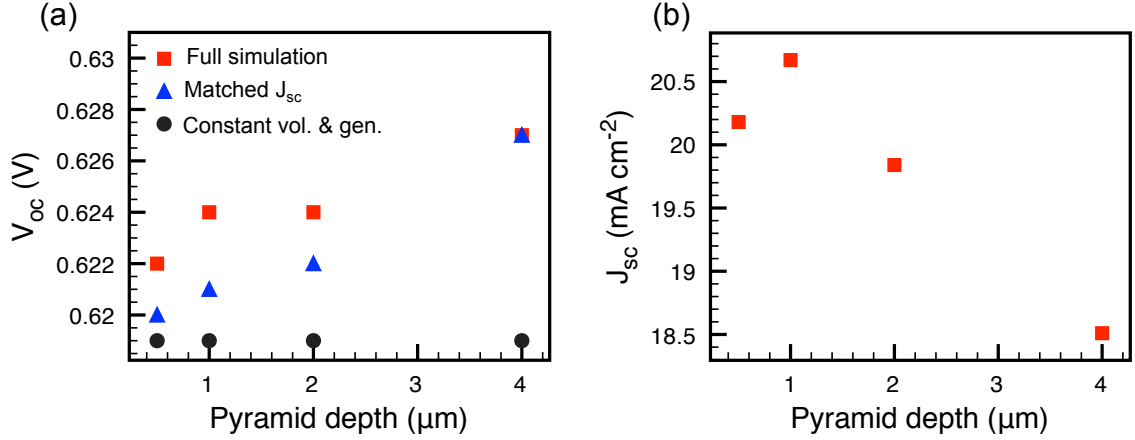


Figure 3.16. Simulated open circuit voltage and short circuit current for textured SHJ solar cells. Both the “full simulation” and “matched J_{sc} ” data sets are from simulations with B fixed at $6 \mu\text{m}$. The full simulation data represents the results from simulations including FDTD calculations of the optical generation rate under one-sun illumination. The matched J_{sc} data is from simulations in which the FDTD calculated generation profiles were scaled such that each device matched the J_{sc} of the $B = 6 \mu\text{m}$, $P = 0.5 \mu\text{m}$. The “constant volume and generation” data set is for simulations in which B and P were simultaneously varied to maintain the average thickness of the $B = 6 \mu\text{m}$, $P = 0.5 \mu\text{m}$ structure, and a uniform generation profile chosen to yield a J_{sc} of 18.55 mA cm^{-2} was used.

This is further supported by considering the simulated SRH recombination rate at V_{oc} as shown in Figure 3.15 in the context of the observation that V_{oc} tends to increase with increasing pyramid depth. Figure 3.15 shows that recombination in the base layer is highest at the depletion region edge. This is due to the carrier concentrations and associated recombination statistics [22]. However, at constant B , an increasing pyramid height P , the surface/volume ratio increases, increasing

the fractional volume of the high recombination associated with the depletion region edge. Despite this, we observe an increase in V_{oc} , indicating that recombination activity over the total absorber volume limits V_{oc} . This explanation is also consistent with the fact that the elevated recombination rate near the depletion region edge is only approximately a factor of 10 higher than elsewhere but the volume over which the elevated recombination takes place is small as shown in Figure 3.15.

Thus the simulations rule out a fundamental limitation of the device physics imposed by a pyramid height comparable to the total absorption thickness. Instead, we conclude that observations of limited V_{oc} in pyramidally structured film SHJ solar cells [23] are due to processing complications associated with achieving a-Si:H deposition on the structured surface.

3.5 Conclusion

The carrier collection physics of SHJ cells are fundamentally different from homojunction devices. While high efficiencies have already been achieved with SHJ cells, continued improvements in the understanding of their device physics will aid in the optimization of future generations of SHJ cells. As SHJ structures are implemented in more complex multidimensional geometries such as the interdigitated back contact scheme, it will be important to consider lateral carrier transport mechanisms such as the inversion layer transport discussed in Sections 3.2 and 3.3. SHJ cells are also promising for application in thin-absorber applications such as kerf-less or film Si. In these applications, the full consideration of their device physics is critical to diagnosing performance-limiting mechanisms and understanding how the properties of the absorber material ultimately affects device performance as discussed in Section 3.4.

Chapter 4

Unified modeling of optical, electrical, and material properties in thin-film solar cells

4.1 Introduction

In order to maximize solar cell efficiency, it is necessary to optimize both the electrical device physics and the optical absorption of the device. Typically, these two problems are treated separately, though compromises between optical and electrical properties are frequently necessary [89, 90]. One route toward realizing benefits to both electrical and optical performance is to use the electrical advantages of thin absorbing layers in combination with light-trapping structures to increase optical absorption within the active layer of the solar cell. The electrical benefits of thin absorbing layers vary for different materials systems [11, 90–92]. For collection-limited semiconductors, thin absorbing layers reduce the need for long diffusion length material. For hydrogenated amorphous Si (a-Si:H) cells, decreased thickness can lead to improved stability and increased open-circuit voltages (V_{oc}) [91, 92]. In addition, thin active regions offer the advantage of decreased cell manufacturing time and cost of raw materials, as well as enabling large scale deployment of scarce materials [92, 93]. However, efficient light trapping is critical to realizing these benefits of thin devices since a reduction in the total material volume decreases the probability that incident light is fully absorbed in the active region.

Standard approaches to light trapping in thin-film solar cells rely on randomly

textured substrates or films to achieve light trapping [94, 95]. However, significant attention has recently been directed toward designed nanostructuring of solar cells [93, 96]. These nanophotonic approaches to light trapping take advantages of metallic and dielectric optical resonances and waveguide modes in periodic or quasi-periodic structures. Such nanostructures offer the ability to control light absorption within a device, and many studies take advantage of theoretical optical analysis to model absorption in these devices and optimize the light-trapping structures [96]. To date, most theoretical studies of light trapping account only for optical effects, but modeling both the electronics and optics of advanced photovoltaic devices is preferable in order to account for carrier recombination and realistically predict device performance [88, 97, 98].

In this chapter, we describe a simulation-based method for simultaneously optimizing the optical and electrical properties of thin-film solar cells with nanophotonic light-trapping structures. A key challenge in the optimization of light-trapping structures is to account for the interdependent optical and electrical properties of solar cells, including variations in material quality. We address this challenge with multi-dimensional optoelectronic simulations that fully account for the optical properties of the device structures and imperfect carrier collection. We present the details of this modeling approach in Section 4.2, and demonstrate that it can be used to reproduce experimental results in Section 4.3. We demonstrate that light-trapping structures can be designed to reduce the fraction of light parasitically absorbed within the device and measurably increase the internal quantum efficiency of charge collection in Section 4.4. In Section 4.5, we discuss the optimization of light-trapping feature aspect ratio and show how our method can be extended to directly account for localized regions of defective material induced by light-trapping structures. This study focuses on a-Si:H solar cells, though the methods are general and applicable to other material systems as well. Our results highlight the full potential of engineered nanophotonic light trapping, showing that optical design can be leveraged to benefit the electrical properties of solar cells.

4.2 Model details

The structures studied here are based on an n-i-p a-Si:H device; in some instances, the substrate is textured, in which case we assume all layers are conformally deposited over the nanostructured substrate. The n-i-p (or p-i-n, in a superstrate configuration) device structure is implemented in a-Si:H solar cells so that a built-in electrostatic field is maintained across the i-layer to drive carrier separation and collection. Carrier collection via drift in a-Si:H solar cells is used because of the low carrier mobility, and thus short minority carrier diffusion lengths, in a-Si:H. Our approach is to first carry out single-wavelength, full-wave optical simulations with the finite-difference time-domain (FDTD) method. The carrier generation profile in the a-Si:H is extracted from the FDTD results for each wavelength and is weighted by the AM1.5G spectrum. The resulting white-light generation profile is then taken as input into a finite element method (FEM) device physics simulation in which the electrostatic and carrier transport equations are numerically solved in the a-Si:H region to extract the current density – voltage (J-V) characteristics of the device. The electrical simulation step accounts for imperfect carrier collection efficiency. The integration of optical and electrical simulations using the software tools implemented here was originally developed by Kelzenberg [88]. From the simulated J-V curve, we extract the open circuit voltage (V_{oc}), the short circuit current density (J_{sc}), the fill factor (FF), and the resulting conversion efficiency. We also use the single-wavelength generation profiles as input into short-circuit calculations to simulate spectral external quantum efficiency (EQE) of the device. This approach accounts for the full microscopic optoelectronic device physics of the cell under illumination and bias in complex geometries.

The structures are based on, from bottom to top, 200 nm of nanostructured Ag, a 130 nm thick aluminum doped zinc oxide (AZO) layer, a variable thickness n-i-p a-Si:H active region, and an 80 nm indium doped tin oxide (ITO) layer. The AZO layer is commonly employed in n-i-p a-Si:H devices both to block diffusion of the Ag into the a-Si:H during growth and to decrease optical losses associated with

coupling to surface plasmon polariton modes [99]. Except where noted otherwise, the simulations are done in 2D to take advantage of reduced computational demand. The corresponding implied 3D structures would be extended in the third dimension to make grating-like structures. In all plots of spatial results presented here, we have stitched together three copies of the simulated region in order to help the reader visualize the periodic structure.

The first step in our approach is to carry out optical simulations by numerically solving Maxwell's equations with a commercial FDTD simulation package [87]. Single-wavelength simulations are carried out at 10 nm increments in wavelength between 350 and 800 nm. Both transverse electric and transverse magnetic polarizations of incident light are simulated, and the results averaged to model unpolarized sunlight. The optical constants for ITO, AZO, and a-Si:H were taken from experimental measurements [91]. The optical constants for Ag were obtained from a Lorentz-Drude fit to values given by Palik [100] as described by Rakic et al. [101]. Each single-wavelength simulation (at wavelength λ) results in an optical field intensity, $|E(\vec{r}, \lambda)|^2$, profile in the simulated structure. We then calculated the wavelength dependent generation rate, profile, $G_{opt}(\vec{r}, \lambda)$, in the a-Si:H using

$$G_{opt}(\vec{r}, \lambda) = \frac{\varepsilon''(\lambda)|E(\vec{r}, \lambda)|^2}{2\hbar} \quad (4.1)$$

derived from the divergence of the Poynting vector, where ε'' is the imaginary part of the permittivity. These single-wavelength generation profiles were weighted by the AM1.5G spectrum to obtain a one-sun, white-light generation profile, $G_{opt}(\vec{r})$, within the a-Si:H. We define the parameter J_{opt} , the optical current density, as the total current that would be extracted if every photon absorbed in the a-Si:H resulted in an electron-hole pair that was collected with unity quantum efficiency. It is obtained by integrating the generation rate $G_{opt}(\vec{r})$, over the a-Si:H region. Similarly we define $J_{opt,i}$ to be the optical current density in the intrinsic a-Si:H only. Taking the ratio of J_{sc} to J_{opt} gives in an internal quantum efficiency of charge collection, referred to here as the electrical internal quantum efficiency (EIQE). Note the distinction

between EQE, which is normalized to the total incident radiation, and EIQE, which is normalized to the total radiation absorbed in the a-Si:H. We also note that parasitic losses in the non-active layers (Ag, AZO, ITO), are accounted for in the optical simulation step. We can calculate these losses explicitly by computing Equation 4.1, in the these non-active layers and interpreting the result as a parasitic absorption rate, which can likewise be integrated over the region of interest to quantify, as an equivalent electronic current, the parasitic absorption losses.

To connect the optical simulations to the device physics simulation, we then interpolated the carrier generation profiles in the a-Si:H region onto a finite element mesh for calculation of the J-V characteristics under illumination [88]. Then the electrical simulations were carried out with a commercial technology computer aided design (TCAD) software package [33] which numerically solves the electron and hole continuity equations:

$$\frac{\partial n(\vec{r})}{\partial t} = G(\vec{r}) - U(\vec{r}) + \frac{1}{q} \nabla \cdot \vec{J}_n(\vec{r}) \quad (4.2)$$

$$\frac{\partial p(\vec{r})}{\partial t} = G(\vec{r}) - U(\vec{r}) - \frac{1}{q} \nabla \cdot \vec{J}_p(\vec{r}) \quad (4.3)$$

the transport equations for electrons and holes:

$$\vec{J}_n(\vec{r}) = q\mu_n n(\vec{r}) \vec{E}(\vec{r}) + qD_n \nabla n(\vec{r}) \quad (4.4)$$

$$\vec{J}_p(\vec{r}) = q\mu_p p(\vec{r}) \vec{E}(\vec{r}) - qD_p \nabla p(\vec{r}) \quad (4.5)$$

and Poisson's equation for the electrostatics:

$$\nabla \cdot \vec{D}(\vec{r}) = \rho_f(\vec{r}). \quad (4.6)$$

In Equations 4.2 - 4.6, n and p are the electron and hole concentrations, G is the generation rate, q is the elementary charge, \vec{J}_n and \vec{J}_p are the electron and hole current densities, μ_n and μ_p are the electron and hole mobilities, \vec{E} is the electrostatic

field, D_n and D_p are the electron and hole diffusion coefficients, and \vec{D} is the electric displacement. The generation profiles calculated via FDTD are taken as input into the continuity equations. The recombination rate (U) is calculated with a model included in the TCAD software package that explicitly calculates the statistics of trap occupation, trap-mediated recombination, and charge state along with the associated electrostatics [33].

We simulated only the a-Si:H regions electrically, and the boundary conditions at the contacts are assumed to be ohmic contacts to the n- and p-type regions. We imposed Neumann boundary conditions at the horizontal boundaries to model a periodic structure. In all plots of spatial results presented here, we have stitched together three copies of the simulated region in order to help the reader visualize the periodic structure implied by the boundary conditions. The band gap was taken to be 1.78 eV in all regions with a 4 eV electron affinity. The active dopant concentration in the doped regions was $3 \times 10^{19} \text{ cm}^{-3} \text{ eV}^{-1}$. All other electronic material parameters are taken to be the values suggested by Schropp and Zeman [34]. The basic electrical parameters for a-Si:H are shown in Table 4.1. We included distributions of traps throughout the band gap to represent band tail (BT) and dangling bond (DB) states. The BT traps are distributed as a function of energy, E , in the band gap according to an exponential:

$$N_0 e^{-\left| \frac{E-E_0}{E_s} \right|}. \quad (4.7)$$

DB traps are distributed in the band gap according to a Gaussian:

$$N_0 e^{-\frac{(E-E_0)^2}{2E_s^2}}. \quad (4.8)$$

All the distributions are defined with respect to the conduction band edge with the exception of the donor/BT traps, which are defined with respect to the valence band edge. All BT traps have capture cross sections for both electrons and holes of $1.6 \times 10^{-4} \text{ cm}^2$. All DB traps have capture cross sections of $7 \times 10^{-14} \text{ cm}^2$. The parameters for the trap distributions are based on those described by Schropp and Zeman [34],

with the exception that the peak dangling bond density in the intrinsic a-Si:H was taken to be $2 \times 10^{17} \text{ cm}^{-3} \text{ eV}^{-1}$ to account for the experimental observation that V_{oc} decreases with increasing intrinsic layer thickness [91]. The full trap parameters used in this work described in this chapter, except where noted otherwise, are shown in Table 4.2.

Table 4.1. Basic a-Si:H electrical parameters

Dielectric constant	11.9
Band gap	1.78 eV
Electron affinity	4 eV
Effective density of states (CB)	$1 \times 10^{20} \text{ cm}^{-3}$
Effective density of states (VB)	$1 \times 10^{20} \text{ cm}^{-3}$
Mobility (electron, hole)	$20 \text{ cm}^2 \text{ s}^{-1}$, $5 \text{ cm}^2 \text{ s}^{-1}$
Thermal velocity (electrons and holes)	$4.27 \times 10^4 \text{ cm s}^{-1}$

For white-light J-V simulation, we take the AM1.5G weighted generation profile $G_{opt}(\vec{r})$, as input into the continuity Equations 4.2 and 4.3. The J-V curve is then swept by quasistatically varying the voltage boundary conditions at the contacts. We also simulate the spectral response of the device by calculating the short circuit current due to the single-wavelength generation profiles, $G_{opt}(\vec{r}, \lambda)$. For the spectral response simulations, illumination power at each wavelength is 10 mW cm^{-2} . This weighting makes the choice of illumination intensity for the purposes of the simulations themselves arbitrary, so long as it does not alter the device physics with respect to the white-light case. To verify this, we integrated the electrical currents calculated at this intensity, weighted by the AM1.5G spectrum, over the wavelength range of interest (350–800 nm) and found that the results matched the calculated white-light J_{sc} to within 0.2%. This indicates that the device physics affecting charge collection are not significantly altered with the choice of 10 mW cm^{-2} as the illumination power at each wavelength for spectral response simulations.

Table 4.2. Basic parameters for trap distributions in a-Si:H

Layer	Type	N_o (cm^{-3})	E_o (eV)	E_s (eV)
Intrinsic	Acceptor/BT	8.00×10^{21}	0	0.032
	Donor/BT	4.00×10^{21}	0	0.047
	Donor/DB	2.00×10^{17}	0.89	0.144
	Acceptor/DB	2.00×10^{17}	0.69	0.144
P-type	Acceptor/BT	2.00×10^{21}	0	0.180
	Donor/BT	1.00×10^{21}	0	0.090
	Donor/DB	2.20×10^{19}	0.7	0.144
	Acceptor/DB	2.20×10^{19}	0.5	0.144
N-type	Acceptor/BT	1.00×10^{21}	0	0.070
	Donor/BT	2.00×10^{21}	0	0.160
	Donor/DB	5.54×10^{19}	1.4	0.144
	Acceptor/DB	5.54×10^{19}	1.2	0.144

All BT traps have capture cross sections for both electrons and holes of $1.6 \times 10^{-14} \text{ cm}^2$
All DB traps have capture cross sections of $7 \times 10^{-14} \text{ cm}^2$

4.3 Agreement between optoelectronic simulations and experimental results

In order to verify that any simulation produces realistic results, it is important to show that it can be used to reproduce experimental results. Here, we apply our optoelectronic simulation technique to reproduce the experimental one-sun AM1.5G J-V curves observed in a-Si:H solar cells featuring light-trapping nanosphere arrays. An example of such a cell is shown in Figure 4.1a. The details of sample preparation and optical theory describing the structure are described elsewhere [102–104]. Both the optical and electrical simulations were done in 3D since the light-trapping mechanism in this sphere-based design is inherently 3D.

Figure 4.1b shows agreement between the experimental and simulated J-V curves. To match the experimental J-V curves in this application, we increased the peak DB trap distribution to $5 \times 10^{17} \text{ cm}^{-3} \text{ eV}^{-1}$. We also added a distributed series resistance of $15 \text{ } \Omega \text{ cm}^2$ to reproduce the slope of the J-V curve near open circuit. Note that this experimental test structure was fabricated such that the device is illuminated through the n-layer. Typically a-Si:H solar cells are illuminated through the p-layer because holes are the less mobile of the two photo-excited species, thus, due to stronger absorption near the front of the device, holes do not have to travel as far to be collected in the p-layer. We also found it necessary to scale down the optical absorption profile uniformly by a factor of 0.9 to match the experimental J-V curve. This is justified by noting that the assumption that every absorbed photon in the a-Si:H creates a mobile electron hole pair may be violated in amorphous material with a high density of states in the band gap.

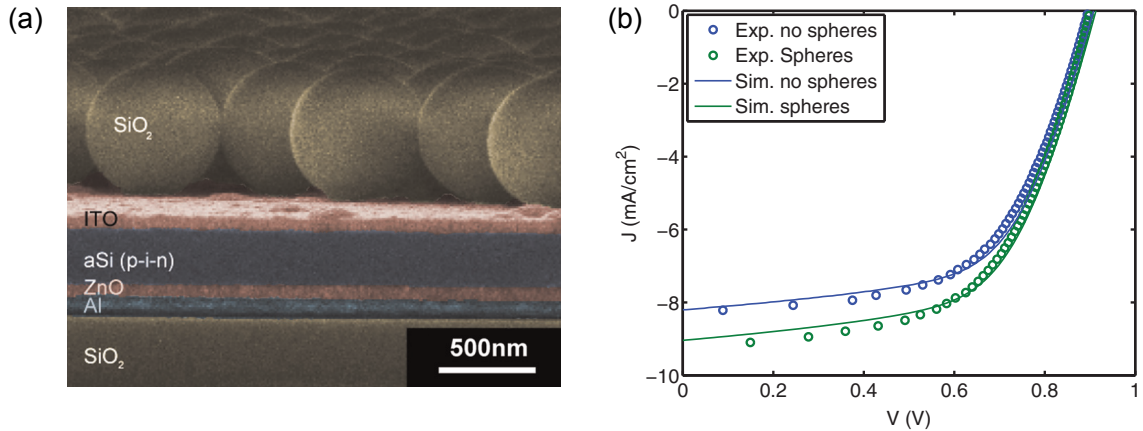


Figure 4.1. (a) False colored scanning electron micrograph showing a flat a-Si:H solar cell which includes an array of light-trapping nanospheres. (b) Comparison of experimental and simulated J-V curves for cells with and without nanosphere arrays, showing good agreement between the experiment and simulation. [102]

4.4 Nanophotonic design to benefit electrical performance

The integration of nanostructures in solar cells significantly changes the mechanism of light absorption. In bulk semiconductor materials, light is absorbed exponentially from front to back via Beer-Lambert absorption. In a thin film with a back reflector, incompletely absorbed light can reflect off each interface several times, making multiple passes through the semiconductor as in a Fabry-Perot cavity [105]. When nanostructures are introduced, however, the absorption in the film will depend on many effects such as scattering, localized modes, and guided modes, which significantly modify both the magnitude and the location of absorption within the thickness of the device [99, 106–111]. The interplay of these effects results in different absorption profiles within the active region for different nanophotonic designs. Here, we implement our coupled optical and electrical model to understand how these differences affect the ultimate electrical device performance.

We explore several different geometries of light-trapping structures and the resulting optical generation profiles, $G_{opt}(\vec{r})$, are shown in Figure 4.2. In the first two designs, the a-Si:H is flat, and a plasmonic ridge is included either on top of the ITO (Figure 4.2b, top grating) or built into the back contact (Figure 4.2e, back grating). In the top grating geometry, the scattering cross section of the ridge, which may be several times larger than its geometrical cross section, couples light preferentially into the semiconductor film. This both increases the path length of the incident light and may couple to the waveguide modes of the structure. In the back grating geometry, the ridge is built directly into the back contact. In this case, light on the blue side of the spectrum will be absorbed by its standard process, while incompletely absorbed red light will scatter from the nanostructure and couple into waveguide modes of the cell. In the third geometry (Figure 4.2d, conformal ITO) we directly structure the ITO while maintaining a flat a-Si:H layer [96]. In the last two geometries, we study cells with both front and back texturing, as would be realized in experimental devices with conformal deposition [91, 96]. In the case shown in Figure 4.2f (conformal Ag), there is both a plasmonic Ag structure on the back interface and a conformal AZO

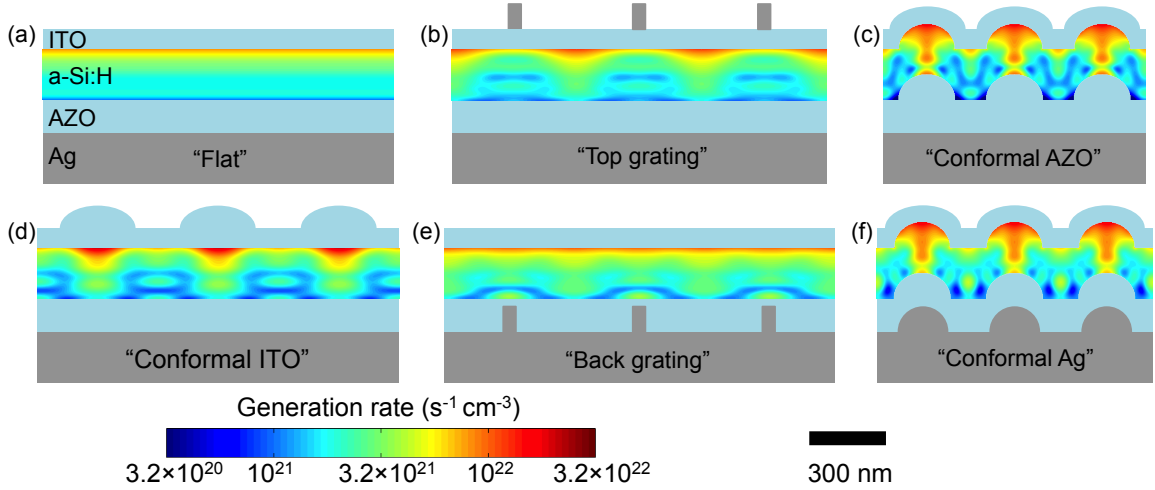


Figure 4.2. The AM1.5G, one-sun, generation rate profile, $G_{opt}(\vec{r})$, calculated from FDTD simulation results plotted on a log scale in the a-Si:H region for several different nanophotonic light-trapping structures. The a-Si:H is 200 nm thick. The Ag ridges in (b) and (e) are 100 nm tall and 50 nm wide. The curved Ag structures in (f) are semicircles with a radius of 100 nm. All other curved surfaces are semi-ellipses with horizontal major axes. The curved ITO structures in (c,d,f) have a major radius of 150 nm and a minor radius of 80 nm. The curved AZO and a-Si:H structures have a major radius of 110 nm and a minor radius of 100 nm. The feature pitch for each structure is given in Table 4.3. [112]

structure coated over the Ag. In the geometry shown in Figure 4.2c (conformal AZO), the Ag layer is a flat mirror but the AZO structure is maintained. As shown in Figure 4.2, the different nanostructures result in different generation rate profiles.

The different light-trapping geometries described here utilize not just plasmonic nanostructures, but also structured semiconductors and dielectrics. For the designs including nanostructured metals, there are several distinct mechanisms that may contribute to plasmonic light trapping [93]. Plasmonic nanostructures exhibit large scattering cross sections, which may be several times their geometrical cross section. In the cases described here, with metal nanostructures on the back contact, the coupled metal nanoparticle / metal film system acts as a plasmonic scatterer for incident sunlight, redirecting light absorption into the cell and potentially coupling into waveguide modes of the device. The metallic nanostructures could also increase absorption locally due to their enhanced local electric field, but the AZO layer here is

130 nm thick, making a local field enhancement unlikely. The waveguide modes of the devices could be either photonic guided modes or surface plasmon polariton (SPP) modes supported on the metal interface; however the presence of the AZO decreases coupling to the SPP modes, as has been discussed elsewhere [96, 99].

To enable straightforward comparison, the conformal geometries were chosen for this portion of the study such that the total volume of a-Si:H is the same as a flat-absorber cell of the same a-Si:H layer thickness. Similarly, the doped regions are thinned over the curved surfaces of the conformal AZO and Ag structures (Figure 4.2c and Figure 4.2f) to maintain the volume ratio of doped to undoped material. We define the parameter d to be the thickness of each doped region in a corresponding flat-absorber cell. For example, in a conformal cell of $d = 20$ nm, the doped regions are 20 nm thick on the flat surfaces and 13.3 nm thick over the curved surfaces.

For each of the structures shown in Figure 4.2, we simulated a range of nanostructure periodicities. The optimal pitch depends on the scattering and absorption cross sections of the features, the strength of their coupling to the waveguide modes, and the constructive and destructive interference of the waveguide modes. Therefore, the optimal pitch varies depending on the light-trapping geometry. Table 4.3 summarizes the electrical and optical performance calculated for each structure at its optimal pitch under white-light illumination. From these results it is apparent that designing light-trapping structures to maximize the absorption current density, J_{opt} , in the semiconductor is the dominant factor in obtaining optimized efficiency in this system.

We note that the optical simulation step accounts for parasitic absorption in non-active regions (Ag, ITO, and AZO). Light absorbed in these regions cannot be expected to contribute to photocurrent. Figure 4.3 shows how each of the materials in the conformal AZO and conformal Ag structures contribute to the overall absorption of the device. In the region around 600–650 nm, the structured Ag back reflector increases parasitic absorption in the Ag. However it is clear from the results in Table 4.3, that in this particular case, the benefits of including the back structuring outweigh the cost of increased absorption in the Ag.

Table 4.3. Simulated electrical and optical performance parameters for 200 nm thick a-Si:H solar cells with $d = 20$ nm extracted from simulations for a flat control and the optimized pitch of each structure shown in Figure 4.2.

Structure	Pitch (nm)	Efficiency (%)	V_{oc} (V)	FF	J_{sc} (mA cm ⁻²)	J_{opt} (mA cm ⁻²)
Flat	–	4.94	0.953	80	6.48	9.22
Back grating	520	5.52	0.957	80.1	7.21	10.28
Conf. ITO	480	5.14	0.955	80.1	6.72	9.70
Top grating	500	5.07	0.954	80.0	6.64	9.38
Conf. AZO	340	6.86	0.963	81.4	8.75	11.85
Conf. Ag	360	7.25	0.965	81.3	9.25	12.28

It is not clear from the results in Table 4.3 whether the change observed in V_{oc} is due to changing photocurrent or to effects of non-standard spatial distributions of carrier generation. To address this, we also calculated the electrical performance of each structure with its J_{sc} matched to that of the flat control structure. This was achieved by scaling the generation profile down by a multiplicative factor prior to inputting it into the device physics simulation. The results of these simulations are given in Table 4.4. From them, we conclude that departures from a flat thin-film interference absorption pattern [105] do not significantly change the relationship between the electrical parameters themselves. The dominant effect of the light-trapping structures is therefore to vary J_{sc} . The V_{oc} and FF vary only in as much as they depend on J_{sc} . We do note, however, that the different profiles, when proportionally scaled, display different white-light EQEs (J_{sc}/J_{opt}) at short circuit. This indicates that some carrier generation profiles are electrically collected more efficiently than others at short circuit.

This effect is quantified in Figure 4.4, which shows that the short circuit EQE correlates with the fraction of absorption current in the intrinsic region. These calculations assume doped regions of $d = 20$ nm. This correlation is understood

Table 4.4. Simulated electrical and optical performance parameters for the devices shown in Table 4.3 with the generation rate profile $G_{opt}(\vec{r})$ of each scaled to match the J_{sc} of the flat control.

Structure	Pitch (nm)	Efficiency (%)	V_{oc} (V)	FF	J_{sc} (mA cm ⁻²)	J_{opt} (mA cm ⁻²)
Flat	–	4.94	0.953	80	6.48	9.22
Back grating	520	4.94	0.953	80.0	6.48	9.19
Conf. ITO	480	4.94	0.953	80.1	6.48	9.36
Top grating	500	4.94	0.953	80.0	6.48	9.16
Conf. AZO	340	5.00	0.952	81.1	6.48	8.78
Conf. Ag	360	5.00	0.952	81.1	6.48	8.60

by noting that the doped regions have much higher densities of dangling bond trap states than the intrinsic a-Si:H, and thus electron-hole pairs generated in the doped regions are subject to higher Shockley-Read-Hall recombination rates making them less likely to be collected as photocurrent [34]. The correlation in Figure 4.4 indicates the importance of light-trapping structures designed to target enhancements in the intrinsic region of the cell, thus avoiding parasitic absorption losses in the doped regions.

Our model predicts that nanostructuring of the a-Si:H layer itself does not degrade V_{oc} , but rather that V_{oc} is improved due to increased photocurrent (Tables 4.3 and 4.4). This result agrees with experimental reports that indicate high V_{oc} can be maintained or improved in nanostructured a-Si:H solar cells [108, 113]. However, there are several possible effects that could lead to a reduction of V_{oc} in nanostructured solar cells. First, increased surface area can result in increased surface recombination. In the structures studied here, the doped regions do not contribute to useful photocurrent (Figure 4.4), and thus an increase in the doped region / contact surface area does not negatively affect V_{oc} . Another potential source of V_{oc} degradation is the increased junction area of the device. However, this prediction is not applicable to n-i-p a-

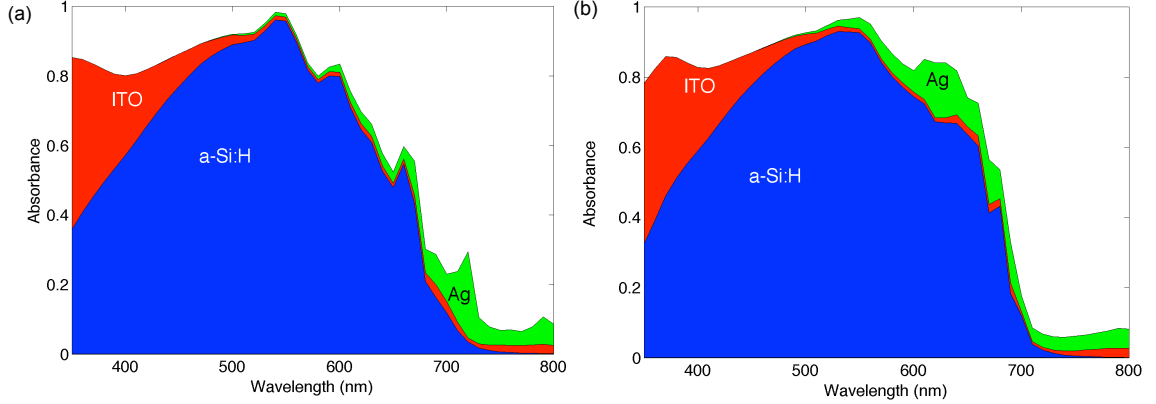


Figure 4.3. Spectral absorption, calculated from optical simulations, in each of the device layers of the conformal AZO device structure (a), and conformal Ag structure (b). Only the absorption in the a-Si:H can be expected to contribute to photocurrent. Absorption in the AZO layers is negligibly low.

Si:H solar cells since trap-mediated recombination in the bulk, and not the forward bias current injected across the junction of an ideal diode, is the primary mechanism competing with photocurrent collection [114–116]. Finally, deposition on textured substrates can lead to degradation in the material quality of the active layers in thin-film Si solar cells, and in turn a reduction of the V_{oc} [117, 118]. We note that our model allows for the inclusion of such effects as described in Section 4.5.2.

Though this study focuses primarily on 2D simulations to take advantage of reduced computational demand, we include the results of two 3D simulations in Figure 4.5 in order to demonstrate that our methods and observations extend to 3D light-trapping structures and devices. The schematics and calculated J-V curves for these two structures are given in Figure 4.5. In both cases, the optical and electrical simulations were carried out for the full 3D device structure. Both devices have $d = 20$ nm. The device pictured in Figure 4.5a corresponds to the point at $J_{opt,i}/J_{opt} = 0.77$ in Figure 4.4 and is based on the conformal Ag structure, but the curved surfaces are 3D semi-ellipsoids. In this case, the doped regions are thinned to 10.5 nm over the curved surfaces. We calculated a white-light conversion efficiency of 7.37% for this structure, with $J_{sc} = 9.36$ mA cm⁻², $V_{oc} = 0.968$ V, and $FF = 81.3$. The device pictured in Figure 4.5b corresponds to the point at $J_{opt,i}/J_{opt} = 0.7$ in Figure 4.4 and

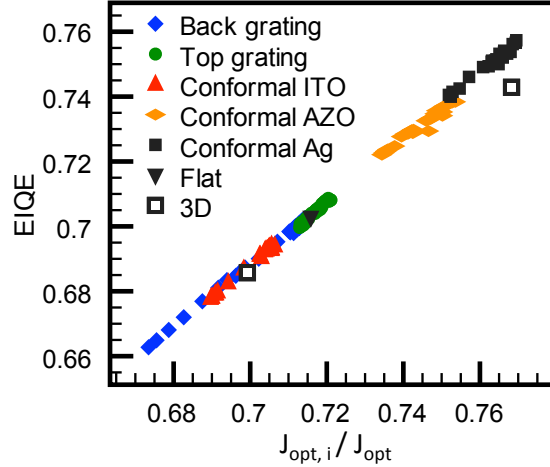


Figure 4.4. White-light electrical internal quantum efficiency at short circuit plotted against the ratio of absorption current density generated in the intrinsic region to the total optically absorbed current density in the a-Si:H for the structures shown in Figure 4.2, along with two 3D structures, with $d = 20$ and varying pitch. We observe a correlation across all structures, indicating the importance of avoiding parasitic absorption in the doped regions of a-Si:H solar cells. [112]

includes only the hemispherical structuring on the Ag back reflector, all other layers, including the a-Si:H, are flat. For this device, we calculated a white-light conversion efficiency of 5.04%, with $J_{sc} = 6.59 \text{ mA cm}^{-2}$, $V_{oc} = 0.956 \text{ V}$, and $FF = 80.1$. Both devices are based on a square array of the light-trapping structures with 300 nm pitch.

Since the performance of the devices studied here is dominated by photocurrent increases due to light trapping, it is critical to understand the factors underlying efficient carrier collection. We note the significance of the observation that the correlation in Figure 4.4 holds for all the structures studied, including conformal ones. This, in combination with the results in Table 4.4, demonstrates that when material quality is assumed to be independent of device morphology, parasitic absorption in doped regions dominates any other performance variations arising from electrical collection, even under bias, of non-standard absorption profiles.

The two structures with conformal a-Si:H layers exhibit higher white-light EIQE than any of the flat devices (Figure 4.4). This is due to decreased parasitic absorption of the blue part of the spectrum in the front p-doped layer, which is thinned over the curved surface. We note that similar geometries have been shown experimentally

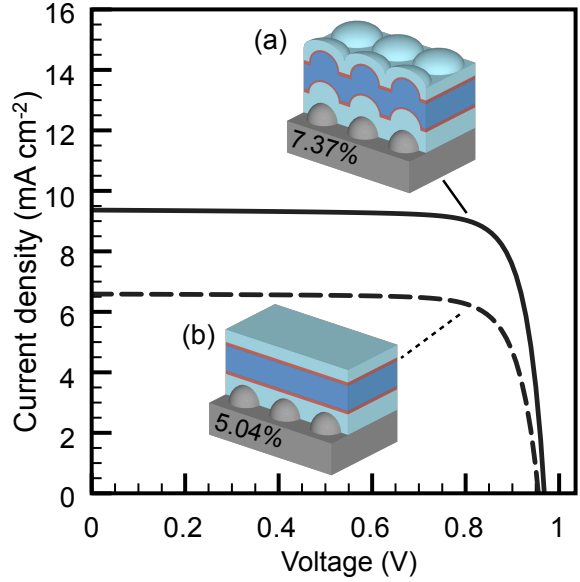


Figure 4.5. Current-voltage curves and one-sun conversion efficiencies calculated with full 3D optical and electrical simulations. The schematics are drawn to scale and have the same color scheme as in Figure 4.2, but with intrinsic a-Si:H indicated as dark blue and doped a-Si:H indicated as red. The upper layers are cut away in the schematics to reveal the underlying structure of the Ag layer. [112]

to exhibit enhanced external quantum efficiency at short wavelengths attributed to improved anti-reflection performance and resonant absorption in the semiconductor nanostructures [91, 119]. However, we are comparing values of EQE which isolate the internal electrical performance of the structure from optical effects such as reflection and resonant absorption.

Among the conformal structures, the conformal Ag structure, which includes plasmonic Ag structures in the back contact, consistently demonstrates higher EQE than the conformal AZO structure, which has a flat Ag surface. Thus there is a twofold advantage for the conformal Ag structure, which includes plasmonic structures, as compared to the conformal AZO structure; it increases the overall light absorbed in the semiconductor, while simultaneously ensuring that the resulting charge carriers are more efficiently collected (Table 4.3).

Careful examination of the spectral response of the two designs reveals the source of this advantage for the conformal Ag structure. Figure 4.6a shows that, for the optimal pitches of the conformal Ag and AZO structures, the increase in optical

absorption and corresponding electrical current of the conformal Ag structure result from an enhancement near an incident wavelength of 650 nm. Figure 4.6bc shows the details of the generation rate profile of 650 nm light for each structure, indicating that the increase in absorption in the conformal Ag case is concentrated in the intrinsic region. The result is that carriers generated from 650 nm light are collected at short circuit with an EIQE of 0.84 for the conformal Ag structure, as opposed to 0.79 for the conformal AZO structure.

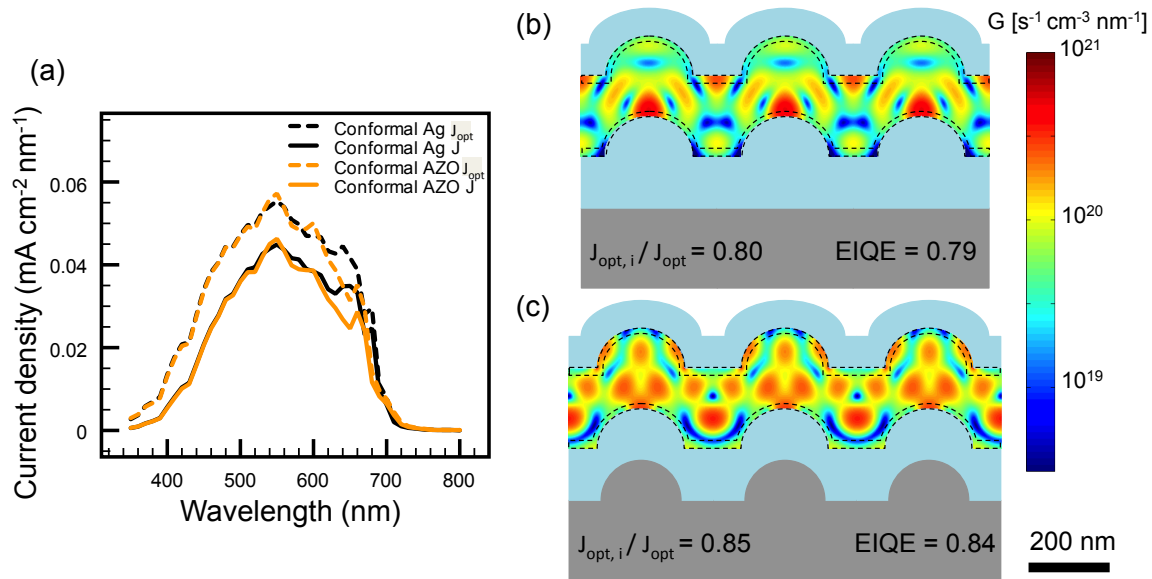


Figure 4.6. (a) Optical and electrical spectral response calculated for the conformal Ag (360 nm pitch) and conformal AZO (340 nm pitch) structures with 200 nm thick a-Si:H layers and $d = 20$ nm, weighted by the AM1.5G spectrum. (b, c) The generation rate from 650 nm light calculated for the conformal AZO (b), and conformal Ag (c) structures plotted on a logarithmic scale, showing the performance enhancement in the conformal Ag structure comes from an optical mode with an improved $J_{opt,i}/J_{opt}$ ratio for 650 nm incident light resulting in improved EIQE at that wavelength as noted in the figure. The dashed lines in (b) and (c) indicate the edges of the doped a-Si:H regions. [112]

This example demonstrates the twofold advantage of including a nanostructured Ag back reflector in the conformal design; it is able to collect more light (Figure 4.6a) and simultaneously use advantageous optical design to reduce the portion of generated current lost to parasitic absorption in the doped regions (Figure 4.6bc). We

estimate that the improvement from EIQE accounts for approximately one quarter of the relative efficiency improvement between the two structures (Table 4.3), with the remainder coming from the optical absorption enhancement. We make this estimate by multiplying the generated current density J_{opt} in the conformal Ag device by the EIQE of the conformal AZO structure to estimate the J_{sc} ; no adjustment is made to the FF or V_{oc} , as these corrections would be small.

This result suggests a novel route toward optical solar cell design, in which light-trapping structures are designed to take advantage of electrical device physics effects. In particular, light-trapping structures for thin-film devices should target enhancement in optical modes that result in efficiently collected carrier generation profiles. In the example considered here, where minimization of parasitic absorption is the dominant effect, a similar benefit to both the EIQE and overall absorption current could be realized without light trapping by thinning the doped regions or increasing the overall thickness of the device.

The effects of such an optimization on the J-V curve of a flat device are shown in Figure 4.7b, along with a thinner un-optimized flat cell (Figure 4.7a) and a comparable conformal Ag cell (Figure 4.7c). The devices in Figure 4.7a and c are comparable in that they utilize the same volume of a-Si:H and the volume ratio of doped to intrinsic a-Si:H is the same. For the optimized flat device (Figure 4.7b), we see the advantage of incorporating thinner doped regions in a thicker overall device structure; the overall absorption current density is increased from 9.40 mA cm^{-2} to 11.66 mA cm^{-2} and the short circuit EIQE is increased from 0.70 to 0.84 compared to the structure in Figure 4.7a. However, in contrast to the case where nanophotonic design is used to target high absorption and improved EIQE (Figure 4.7c, $V_{oc} = 0.965$, $FF = 81.3$), the optimized flat device suffers degradation of V_{oc} (0.939 V) and FF (72.3).

The benefit of coupled optical and electrical optimization is apparent in the result that, in the limiting case of perfectly flat layers, the maximized efficiency of 6.58% remains less than the efficiency of 7.25%, which can be achieved in a thinner device with conformal light-trapping structures and thicker doped regions (Figure 4.7c). This thinner design with conformal light-trapping structures increases absorption

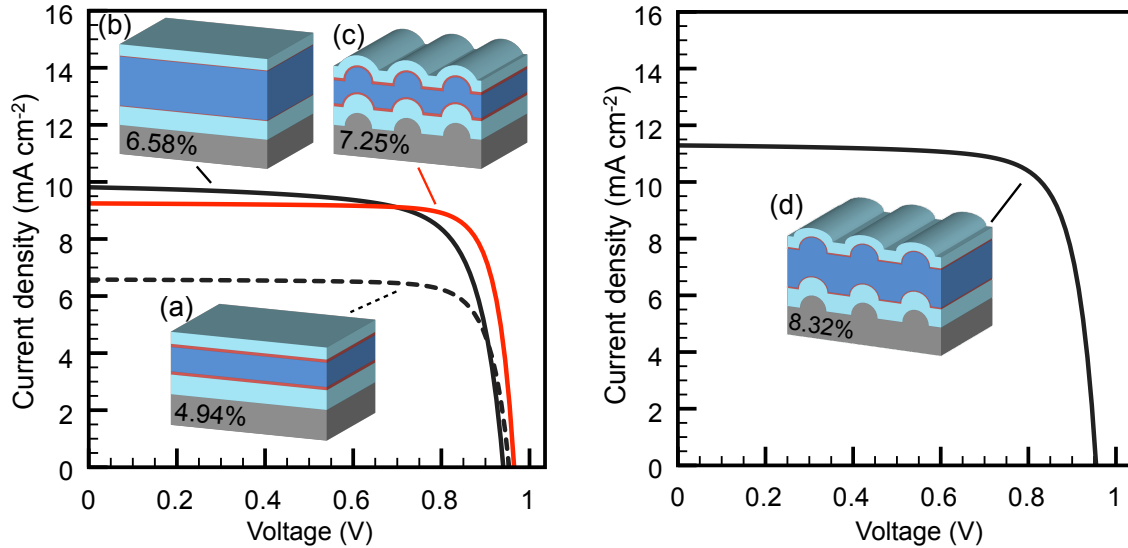


Figure 4.7. Current-voltage curves for solar cells with (a) a 200 nm thick a-Si:H layer with $d = 20$ nm, (b) a 360nm thick a-Si:H layer with $d = 5$ nm, (c) a conformal Ag cell with a 200 nm thick a-Si:H layer, $d = 20$ nm, and a feature pitch of 360 nm, and (d) the optimized geometry for the conformal Ag structure with a 290 nm thick a-Si:H layer, $d = 10$ nm, and pitch of 390 nm. The schematics are drawn to scale and correspond to the implied three-dimensional structures associated with the simulated plane. They have the same color scheme as in Figure 4.2, but with intrinsic a-Si:H indicated as dark blue and doped a-Si:H indicated as red. One-sun conversion efficiencies are indicated on the schematics. (b) is the design with the maximum efficiency we found for a flat cell without additional light-trapping features for the material parameters used in this study; we note that it has degraded V_{oc} and FF compared to the other devices. [112]

and EQE without degradation of V_{oc} or FF (Table 4.3). It also has the advantages of reduced processing costs of Si deposition, reduced light-induced degradation, and decreased vulnerability to non-uniformities in the thicker doped regions [91, 92]. All these benefits are realized while achieving a higher efficiency than an optimized flat cell.

The efficiency of the conformal Ag design is maximized by increasing the a-Si:H thickness to 290 nm and thinning the doped regions to $d = 10$ nm (Figure 4.7d). The optimized feature pitch for this structure is 390 nm. This design yields an efficiency of 8.32% with $J_{sc} = 11.29 \text{ mA cm}^{-2}$, $V_{oc} = 0.955 \text{ V}$, $FF = 77.2$, and white-light EQE = 0.87. We note that the a-Si:H is 70 nm thinner than in the optimized flat device

(Figure 4.7a), resulting in improved V_{oc} and FF . The fact that it also exhibits higher J_{sc} and EQE than the optimized flat device, despite an increased ratio of doped to undoped a-Si:H, highlights the power of coupled optical and electrical optimization.

4.5 Optoelectronic effects of changing feature aspect ratio

In order to fully optimize nanophotonic light-trapping structures, the effects of geometrical modifications of a particular design must be considered. In this section we explore how changes in the aspect ratio of light-trapping features based on the “conformal Ag” design described in Section 4.4 affect device performance. An example is shown in Figure 4.8, showing the nonuniform built-in electrostatic field in the nanostructured i-layer. We begin by considering an ideal case and then demonstrate the importance of accounting for local defects in material quality induced by high-aspect-ratio structures.

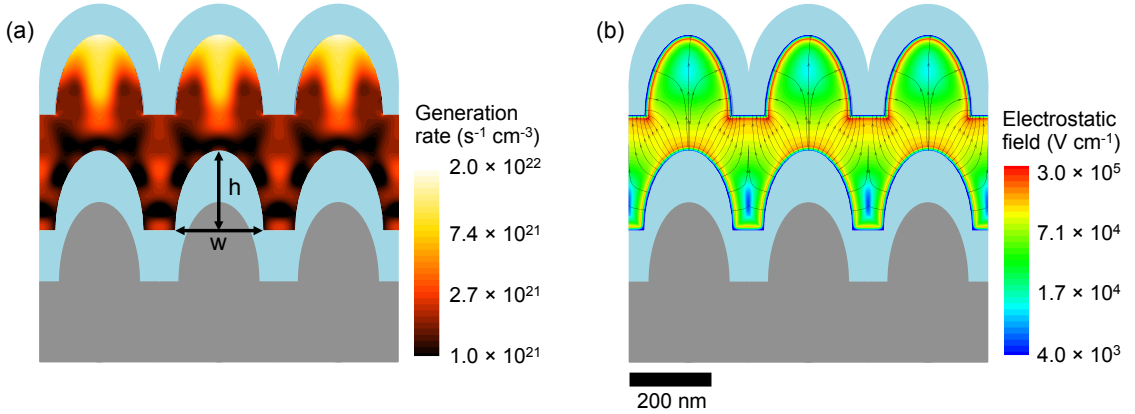


Figure 4.8. Simulation results plotted in the a-Si:H region of a 290 nm thick device with $w = 220$ nm, and $h = 200$ nm. The devices are based on, from bottom to top, 200 nm of Ag, 130 nm of AZO, 290 nm n-i-p a-Si:H, and 80 nm of ITO. (a) The white-light carrier generation profile calculated from FDTD simulations for AM1.5G illumination. (b) The electrostatic field in the a-Si:H region at short circuit under illumination, obtained from finite element device physics simulations which take the generation profile shown in (a) as input in order to simulate the J-V characteristics of the device.

An example of the structure considered in this section is shown in Figure 4.8. For the simulations discussed in this section, we consider a structure in which the

200 nm thick Ag back reflector is over coated with 130 nm of aluminum doped zinc oxide (AZO), an n-i-p active region of variable thickness with 10 nm n- and p- layers (which are not thinned over the curved surfaces), and an 80 nm indium tin oxide (ITO) top contact and anti-reflection coating. We fixed the width of the AZO and a-Si:H features, w , at 220 nm and varied the height h to change the feature aspect ratio ($2h/w$). The Ag feature is 200 nm wide, and the ITO feature is 300 nm wide. The pitch between features was held constant at 300 nm. The height of the features is h for all layers. We did not consider any structure in which h exceeds the a-Si:H thickness to avoid unrealistically thin regions.

4.5.1 Changing aspect ratio: Ideal case

We first consider the effects of changing aspect ratio in an idealized case. We assume that the electronic material quality of the a-Si:H does not change as a result of changing the aspect ratio of features. In this case we assume that the peak dangling bond density in the intrinsic region is $1.6 \times 10^{16} \text{ cm}^{-3} \text{ eV}^{-1}$ [34].

The geometry shown in Figure 4.8 achieves light trapping through several mechanisms including anti-reflection, local and guided optical modes in the various dielectric and semiconducting layers, and plasmonic scattering from the nanostructured Ag back reflector [96, 120, 121]. Increasing the aspect ratio of the light-trapping features reduces reflection by creating a graded refractive index profile. The photocurrent enhancement in the solar cell, however, also depends on resonant absorption in the semiconductor and on the effectiveness of the nanostructures in coupling to waveguide modes, both of which are sensitive functions of the nanostructure geometry.

The relative contributions of the different light-trapping mechanisms vary with wavelength, as shown in Figure 4.9 for a 290 nm thick a-Si:H solar cell. The figure shows the wavelength-dependent absorption in the i-layer of the a-Si:H cell at several different aspect ratios. On the blue side of the spectrum where absorption in a-Si:H is strong, anti-reflection and localized resonances dominate the response. In this spectral regime, the performance improves very slightly with increasing aspect ratio. On the red side of the spectrum where absorption in a-Si:H is weak, light can

be coupled into waveguide modes of the solar cell [91]. The number of supported waveguide modes depends on the thickness of the a-Si:H layer, and their spectral position depends on the pitch and aspect ratio of the nanostructures. In this case the pitch is fixed at 300 nm. The two sharp features in the spectrum, beginning around $\lambda = 620$ nm and $\lambda = 670$ nm, are due to waveguide modes. As the aspect ratio increases, their spectral positions red shift. The overall photocurrent enhancement due to these modes depends on both the absorption response of the device and the illumination spectrum. Thus appropriately tuning the spectral position of the resonances leads to an optimal aspect ratio, here at 1.82 ($h = 200$ nm).

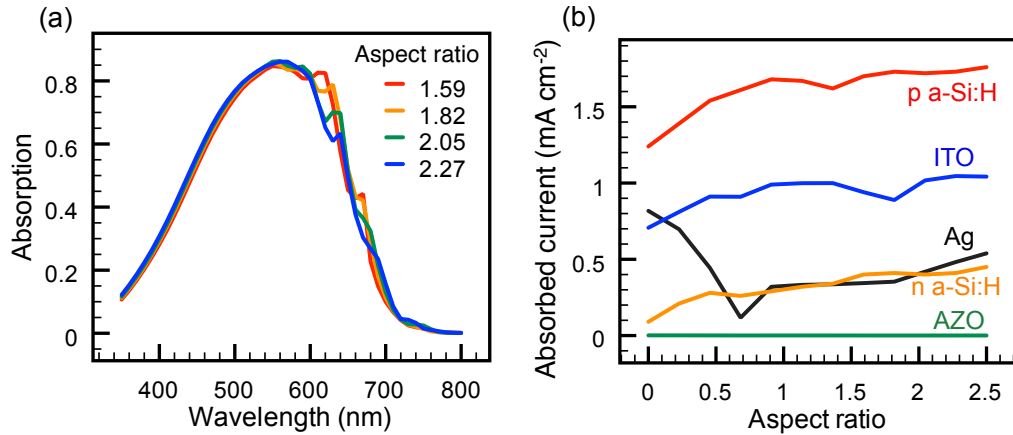


Figure 4.9. (a) The spectral absorption in the i-layer of a 290 nm thick device showing the shifting of waveguide mode as the aspect ratio ($2h/w$) changes. The optimal aspect ratio is ultimately determined by both the absorption and illumination spectrums. (b) The parasitic absorption expressed as an equivalent current density for AM1.5G illumination in layers other than the i-layer of the a-Si:H for a 290 nm thick device calculated from FDTD results.

In the design of nanophotonic light-trapping structures, it is critical to ensure that light is absorbed in the active region of the device. Figure 4.9b quantifies the parasitic absorption losses when weighted across the solar spectrum. They are expressed as current densities under AM1.5G illumination for ease of comparison with the device current. We note that the p-layer contributes most to parasitic absorption, primarily due to absorption of short wavelength light. Similarly, the ITO is also a significant source of loss. Notably, the loss due to Ag is substantially lower, indicating that

the introduction of plasmonic nanostructures does not significantly increase parasitic losses in the device, even with increasing aspect ratio. Overall, while there are slight increases in the parasitic absorption with increased aspect ratio, these losses are offset by larger gains in useful absorption in the intrinsic region as shown Figure 4.10a which shows $J_{opt,i}$ in the a-Si:H i-layer for varying a-Si:H thickness and light-trapping feature aspect ratio.

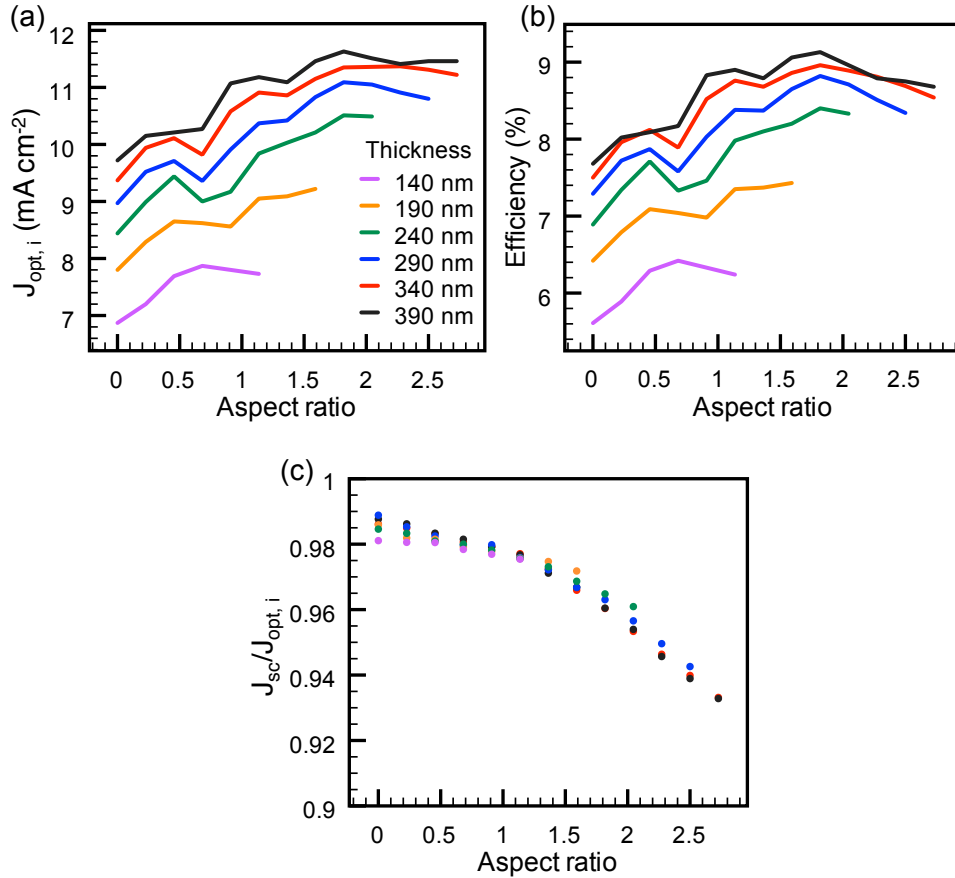


Figure 4.10. (a) The calculated absorption in the i-layer of the a-Si:H expressed as an equivalent current density under AM1.5G illumination for different a-Si:H thickness as the aspect ratio ($2h/w$) of the light-trapping feature is changed. (b) The calculated one-sun conversion efficiency for the same devices. (c) The ratio of the short circuit current to the absorption current in the a-Si:H i-layer as aspect ratio changes.

We used the FEM device physics simulations, which take the optical carrier generation rate calculated from the FDTD simulations as input, to model the electrical

performance of devices for changing feature aspect ratio and a-Si:H thickness. The efficiencies extracted from these calculations are shown in Figure 4.10b. Comparing the trends in Figure 4.10a and 4.10b, we note that efficiency is primarily dictated by the absorption in the a-Si:H i-layer, indicating this as the most important design criterion for these structures in this particular system.

However, we also note a decrease in the carrier collection efficiency at short circuit from the i-layer as aspect ratio is increased. This effect is quantified in Figure 4.10, which shows the ratio of J_{sc} to $J_{opt,i}$ in the a-Si:H i-layer for all the thicknesses studied. We attribute this reduction in carrier collection efficiency to a reduction in the electrostatic field in certain areas of the i-layer as a result of device geometry. This is apparent in Figure 4.8b. In particular, the field is reduced in the area between light-trapping features where the n-regions coating neighboring semi-ellipsoids are nearly parallel, and in the semi-elliptical region centered above the raised feature of the back reflector. Figure 4.8a shows that there is strong optical absorption in the semi-elliptical region, which likely augments the reduction in collection efficiency.

Although this reduction in carrier collection efficiency at high aspect ratio is non-negligible, it does not outweigh the raw absorption enhancement achieved from optimizing the optical design for the geometries studied here. However, both the optical and electrical effects are strongly dependent on device geometry. It is expected that in other light-trapping geometries or solar cell material systems that reduced electrical performance can outweigh optical gains. Thus it is important to consider this trade off between optical and electrical performance on a case-by-case basis.

4.5.2 Accounting for localized material defects

It is important to note that deposition of highly structured active layers can result in localized regions of low material quality, resulting in a trade-off between enhanced optical design and optimized material quality [108, 117, 118, 122, 123]. In order to optimize device efficiency, it is therefore important to consider the effect of morphologically induced local defects when designing and optimizing light-trapping nanostructures [122]. Here, we demonstrate that such local defects can be accounted

for in multidimensional optoelectronic simulations of nanostructured thin-film a-Si:H solar cells. Explicitly accounting for local variations in material quality in these simulations provides physical insight into the microscopic device physics governing operation.

We address the trade-off between optical design and electrical material quality, in the electrical simulation step by including a localized region within the a-Si:H exhibiting increased dangling bond trap density. This region of degraded material represents a recombination active internal surface (RAIS) formed during deposition. Such localized regions of low-density, low-electronic-quality material quality are known to form during PECVD when growing surfaces collide with one another during deposition, a process that is particularly likely in high-aspect-ratio features used for light trapping [108, 117, 118, 122].

In this portion of the study we fix the a-Si:H total thickness to 290 nm (with 10 nm doped regions) and the aspect ratio $2h/w$ to 1.82. To more accurately reproduce experimental FF s we also include a $5 \Omega \text{ cm}^2$ series resistance at the top contact and a shunt resistance (parallel to the device) of $5 \text{ k}\Omega \text{ cm}^2$ with the built-in TCAD circuit simulation capabilities. The structure we investigated is shown in Figure 4.11a. To explicitly account for the effects of RAISs, we include 5 nm wide vertical strips of defective a-Si:H extending through all the active regions of the device. In these RAIS strips we specified an increased peak dangling bond density of $2 \times 10^{20} \text{ cm}^{-3} \text{ eV}^{-1}$. The dashed lines in Figure 4.11a show the location of the RAISs. Our assumption that these low-density regions are characterized by an increased dangling bond density is justified by experiments showing that a-Si:H solar cells with increased concentrations of microvoids showed degraded performance attributed to an increase in dangling bond density [124]. We found that the peak dangling bond density specified in the RAISs results in device performance similar to that obtained by specifying a surface recombination velocity (SRV) of 10^6 cm s^{-1} at the interface between the RAISs and the bulk a-Si:H. Specifying an SRV of 10^6 cm s^{-1} yields a 5.86% efficient device compared to an efficiency of 5.90% with a peak trap density of $2 \times 10^{20} \text{ cm}^{-3} \text{ eV}^{-1}$ in the RAISs region (the value used throughout this study). We prefer the explicit

inclusion of traps in the model because it more closely represents the fundamental physical mechanism underlying the recombination activity of the RAISs.

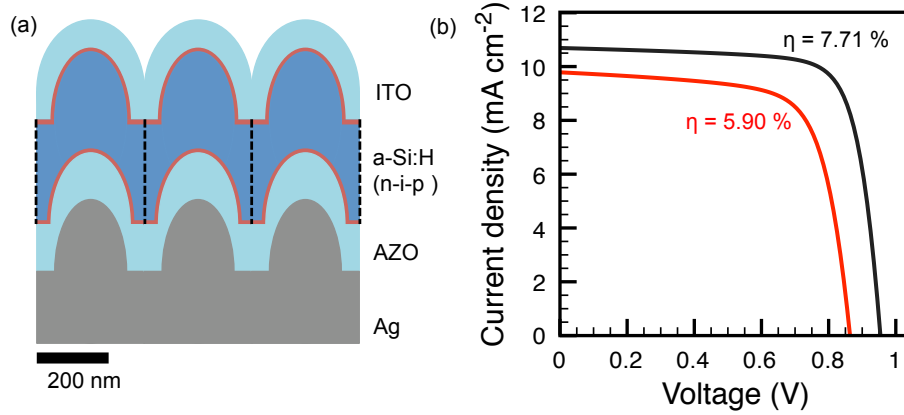


Figure 4.11. (a) Schematic showing the geometry of simulated n-i-p a-Si:H solar cell. The red regions indicate the doped a-Si:H. The dashed lines indicate the location of recombination active internal surfaces (RAISs), which are accounted for in the model as local regions of degraded material quality extending vertically through the device. (b) Current density – voltage curves showing the simulated change in performance between the case in which no material degradation is assumed (black) and the case in which RAISs are included. The conversion efficiencies are noted on the plot. [125]

In agreement with experimental reports [117, 118, 122], the introduction of RAISs is found to adversely affect performance as shown in Figure 4.11. When RAISs are included in the electrical simulation, the AM1.5G energy-conversion efficiency is reduced from 7.71% to 5.90%, the J_{sc} from 10.69 mA cm^{-2} to 9.79 mA cm^{-2} , the V_{oc} from 0.954 V to 0.864 V, and the FF from 76.3 to 70.4. To determine if the reduced V_{oc} is due to the reduced J_{sc} , we also simulated the cell without RAISs and with the generation profile, $G_{opt}(\vec{r})$, uniformly scaled down by a factor of 0.9158. This resulted in a J_{sc} matched to that of the case including RAISs (9.79 mA cm^{-2}). In this case however the V_{oc} was only reduced by 3 mV, to 0.951 V, and the FF remained 76.3. This indicates that the reduction in V_{oc} cannot be directly attributed to the reduced J_{sc} associated with the RAIS.

Studying the simulated spectral response of these devices reveals interactions between the generation profile and the geometry of the device and RAISs themselves.

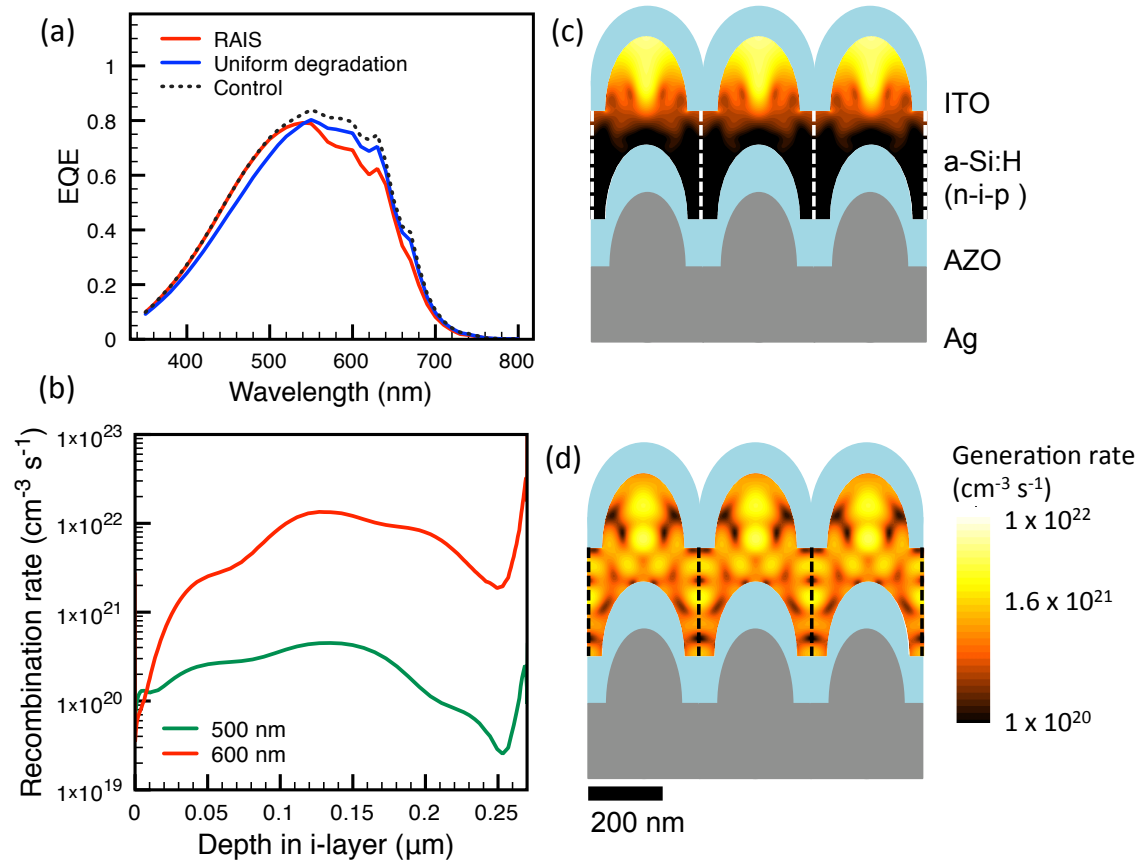


Figure 4.12. Spectral coupling between optics and defect geometry. (a) The simulated external quantum efficiency (EQE) for a device with no assumed material degradation (control), a device with the i-a-Si:H uniformly degraded, and a device with RAISs. We note that the EQE curves for the uniform degradation and RAIS case differ from one another. (b) The recombination rate in the RAIS region plotted as a function of depth in the i-layer (with 0 being the p/i interface) for single-wavelength illumination at 500 and 600 nm. (c) and (d) the generation rate profile for single-wavelength illumination at 500 and 600 nm, respectively. We note that under 500 nm illumination, the EQE for the control and RAIS cases exhibit very small deviations from one another, while at 600 nm, the RAIS EQE is significantly degraded. We attribute this to increased optical generation in the vicinity of the RAISs at 600 nm illumination, leading to more recombination in the RAIS and thus decreased EQE. [125]

Figure 4.12a shows the simulated EQE as a function of wavelength for three cases: a control in which the a-Si:H is assumed to maintain high quality, with a peak dangling bond density in the intrinsic region of $2 \times 10^{17} \text{ cm}^{-3} \text{ eV}^{-1}$, the RAIS case described above, and a device in which the intrinsic a-Si:H has a uniformly degraded material quality without explicitly considering localized defects. In the third case, the peak dangling bond density in the intrinsic region is increased to $1.08 \times 10^{18} \text{ cm}^{-3} \text{ eV}^{-1}$, which was chosen because it results in a white light device efficiency of 5.90%, identical to that obtained in the RAIS case. (The uniformly degraded cell exhibits a J_{sc} of 10.18 mA cm^{-2} , a V_{oc} of 0.880 V and a FF of 66.4 under AM1.5G illumination.) This allows us to compare a case where optical design interacts with a localized defect to a case where the degradation is global throughout the film. Figure 4.12a shows that both the uniform and RAIS cases exhibit degraded spectral response when compared to the control case. However, we also note that the RAIS and uniform degradation EQE curves vary from one another.

To understand this effect, we compare the internal device physics for the RAIS case under two illumination wavelengths: 500 nm, at which there is negligible deviation between the RAIS case and the control, and 600 nm at which the RAIS case exhibits degraded EQE. In both the uniform degradation and RAIS cases, the optical generation profile at each wavelength is identical, so differences are due to electrical properties. Comparing the recombination activity within the RAIS region at these illumination wavelengths as shown in Figure 4.12b, we see that the recombination activity is significantly higher at 600 nm wavelength illumination. Figure 4.12c,d shows that under 600 nm illumination, much more optical generation is taking place in and around the RAIS than at 500 nm illumination. Thus we attribute both the spectral variation in RAIS recombination activity and the deviations between the RAIS and uniform degradation EQE curves to interaction between the geometry of the generation profile and geometry of the RAIS. If there is a large amount of optical generation in and around the RAIS, this leads to an increase in RAIS recombination activity and a corresponding decrease in EQE.

To quantify the effect of this optoelectronic interaction under AM1.5G illumina-

tion, we compare the results of the full white-light simulation of the RAIS case to a case in which we assume a constant uniform optical generation rate of $3.04 \times 10^{21} \text{ cm}^{-3} \text{ s}^{-1}$; this generation level was chosen because it produces the same J_{sc} as the realistic simulation including the nonuniform generation profile associated with the light-trapping nanostructures. While somewhat unphysical, this uniform generation case allows us to understand the effect of the interaction between the RAIS geometry and the optical generation profile. We calculate the optical generation current density in the intrinsic region, $J_{opt,i}$, by spatially integrating the white-light generation profile, $G_{opt}(\vec{r})$, over the intrinsic a-Si:H region. It is well known that carrier collection is poor from the doped regions, making the intrinsic layer the region area of interest as described in Section 4.4. We observe that the ratio $J_{sc}/J_{opt,i}$ changes from 0.88 for the full optoelectronic simulation to 0.80 for the uniform generation simulation. If we carry out the same procedure for the case without the RAISs, the ratio $J_{sc}/J_{opt,i}$ remains high, changing from 0.96 to 0.95. This shows that the interaction between microstructure and optical generation profile is not limited to single-wavelength illumination, but it also affects the internal quantum efficiency of charge collection under full AM1.5G illumination. It is particularly important to account for this interaction in periodic structures such as that studied here since both the generation profile and the defect structure are periodic.

This geometric interaction between the optics and electrical device physics can only be captured with multidimensional modeling. Furthermore, this effect illustrates the importance of accounting for defect geometry, and that approximations involving uniformly degraded active material to account for localized defects do not fully capture the optoelectronic device physics. We note that several 1D device simulation tools have been widely and successfully used to simulate and study solar cell performance in a variety of applications [126–130]. However, this interaction between optics and defect geometry is inherently multidimensional and cannot be captured with a 1D simulation.

This modeling approach also provides insights into the microscopic device physics of the RAIS under 1 sun AM1.5G illumination. Figure 4.13 shows the magnitude of

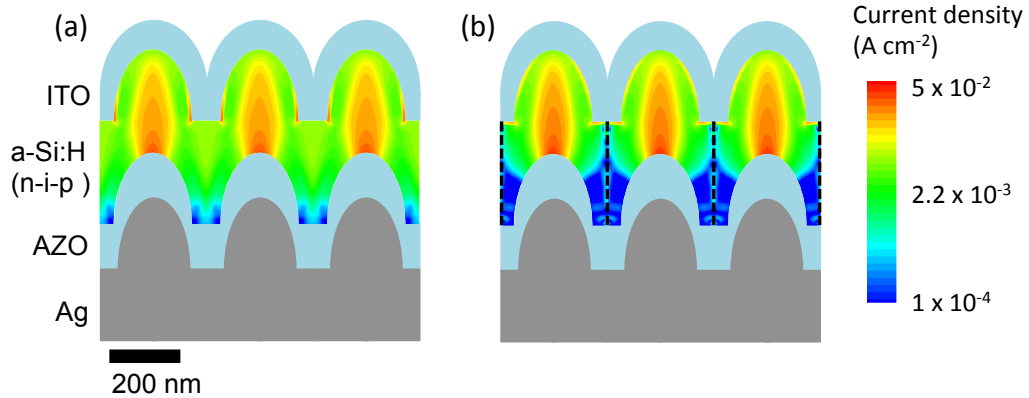


Figure 4.13. Simulated magnitude of the current density within the a-Si:H at the maximum power point operating bias of the respective device under AM1.5G illumination for (a) the control case with no material degradation (operating bias: 792 mV) and (b) the RAIS case (operating bias: 690 mV). We note that current is suppressed near the RAIS itself, while collection from other areas of the device is not significantly impacted. [125]

the current density within the a-Si:H in the device without (Figure 4.13a), and with (Figure 4.13b) RAISs at the respective maximum power point operating voltage. We observe local reduction in current density in the region around the RAIS (Figure 4.13b) when compared to the control case (Figure 4.13a.). This shows that current flow in the bulbous regions (which are assumed to be high-quality a-Si:H) remains largely unperturbed by the addition of the RAISs and that the detrimental effects of the RAISs is localized to the immediate region surrounding them.

Figure 4.14 shows the recombination activity in a RAIS for varying operating bias under AM1.5G illumination. We see that as the device is forward biased, the recombination rate in the defective RAIS region increases. This is expected, since carrier collection from the absorber is necessarily less efficient as the device is forward biased and the built-in electrostatic field driving carrier collection is reduced, enabling more carriers to recombine in the highly defective RAIS region before being collected. It is interesting to note that most of this increase in recombination activity occurs near the front of the device. We emphasize that this is purely a result of the solution to the electrostatic, current, and continuity equations (Equations 4.2-4.6) under the changing contact boundary conditions, and is not due to any assumed change in the

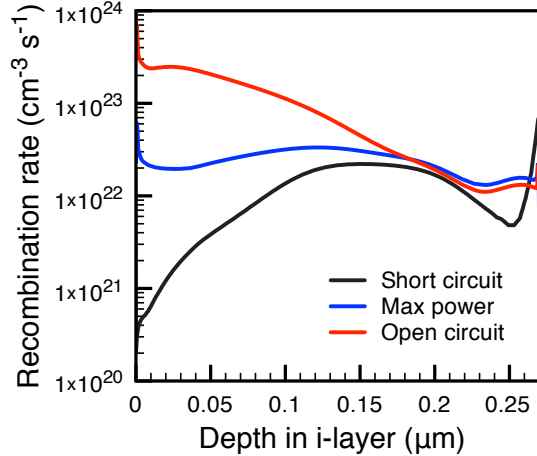


Figure 4.14. Simulated recombination rate in the RAIS region plotted as a function of depth (with 0 being the p/i interface) in the intrinsic a-Si:H layer, at short circuit, maximum power operating point (690 mV), and open circuit (864 mV). The recombination activity in the defective RAIS region is shown to increase as the forward bias is increased. [125]

physical or electronic structure of the RAIS regions themselves under forward bias.

4.6 Conclusion

It is critical to account for trade-offs between optical and electrical performance in the optimization of light-trapping structures for solar cells. This prevents the unconstrained optimization of the optical properties of a device from yielding impractical geometries that suffer severe material quality degradation. In addition to providing a detailed picture of the microscopic device physics affecting carrier collection, our results highlight the importance of accounting for the specific geometry of the defects themselves along with the full optical absorption profile within the device. In particular, we find that interactions between the geometry of the absorption profile and localized recombination active internal surfaces (RAISs) can induce significant variations in carrier collection efficiency in a-Si:H cells. Such effects cannot be fully accounted for without implementing a multidimensional model such as that used here. Furthermore, the results in Section 4.4 demonstrate how optical design can be used to directly benefit the electrical performance of the device.

Such co-optimization is a powerful approach in the design of solar cells. It enables enhancements beyond those that can be achieved by individually optimizing each physical mechanism, and enables the design of devices in which the optics can directly benefit electrical carrier collection.

Chapter 5

Conclusion and outlook

Solar cells are macroscopic devices. A typical photovoltaic cell is tens or hundreds of centimeters in size. They are sold in modules on the scale of meters, and assembled in arrays spanning kilometers. Yet they are governed by physics at the scale of microns and nanometers. Since conversion efficiency is one of the key system cost drivers, it is critical to understand how the microscopic optoelectronic device physics of solar cells affect advanced device design. More importantly, it is imperative that we understand how to harness these governing physical principles to drive solar cell efficiency higher, and drive the associated energy generation costs lower.

5.1 Summary of work

This thesis address three advanced silicon-based solar cell technologies with a focus on understanding their device physics. While these or similar technologies have been commercialized with varying levels of success, optimization at the device scale is often empirical and aided by simplified solar cell models (such as the equivalent circuit). As solar cells continue to evolve to more advanced designs and their efficiencies increase toward their fundamental limits, it becomes more important to take a detailed microscopic view of the physics governing their operation.

In Chapter 2, we considered solar cells based on thin-film crystalline Si absorbers. Such designs are promising because they can leverage the manufacturing benefits of thin-film solar cells, but maintain the performance benefits of a crystalline Si absorber.

We described the experimental development of such absorbers based on the use of low-temperature epitaxial HWCVD. The use of thin crystalline absorbers, for example those fabricated by other methods such as epitaxial lift off of kerf-less wafering, is a key area of research and development in photovoltaics. When absorbers are fabricated by different methods, they are likely to show different microstructures, and it is important to understand how these differences affect not only device performance, but also device design choices. For example, we show that in thin crystalline Si absorber layers featuring recombination-active interfaces, the choice of doping level is important because it enables favorable recombination statistics and electrostatic screening of charged defects.

In Chapter 3, we presented modeling and experiments which show that lateral carrier transport occurs near the interface between a-Si:H and c-Si in silicon heterojunction (SHJ) cells. SHJ cells are an example of a commercialized technology that stands to further benefit from improved understanding of the associated device physics. The majority of successful devices have been quasi-1D in that they are based on a simple layer stack geometry. Current work focuses on the optimization of an interdigitated all back contact design which would inherently involve 2D or 3D carrier transport effects. There still remains significant work to be done to fully understand and characterize the transport physics of the SHJ, and consideration of lateral transport near the heterojunction will be important to consider as SHJ designs advance to more complex device geometries.

Chapter 4 described simulations addressing the link between the optical and electrical design of solar cells. Engineered nanophotonic structures are a promising approach to light trapping, not only because it enables an increase in light absorption in solar cells, but also because it yields an extra degree of control which can be used to guide light absorption within devices. In the context of thin-film a-Si:H solar cells, we developed a model which can fully account for the optical, electrical, and material properties of nanophotonic light-trapping structures and we investigated interactions between all three effects. We showed that when local defects are induced by the light-trapping geometry, the optics can couple to the defect geometry, an effect

that can only be captured with complete optoelectronic device physics simulations. Furthermore we described how nanophotonics can be used to engineer light absorption in a device, reducing parasitic absorption to benefit the electrical quantum efficiency of the cell. This comprehensive optoelectronic approach to device design is generally applicable to other material systems. It represents a powerful design paradigm for future generations of solar cells in that it enables the design of device optics and electronics which actively benefit one another.

5.2 Outlook

The common principle behind the work described in this thesis is that solar cell designs can and should be developed considering the full device structure, material properties, and multidimensional physics of the device. This principle is not limited to the Si-based photovoltaics considered here and can readily be applied to other material systems. Furthermore, it is applicable beyond photovoltaics to other next-generation energy-conversion technologies. For example, this principle applies to the development of semiconductor-based photoelectrochemical fuel generation systems [131]. Such devices need to absorb light and extract charge just like solar cells, but must also be designed taking into account other factors including the effect of heterogeneous catalysis on the band energetics of the semiconductor [132, 133] and transport of the fuel products away from the active device region [134]. While these features have all been studied separately, development of a comprehensive model may yield ways in which different processes can be not only independently optimized, but can also be simultaneously co-optimized at the device level, much like the optical and electrical optimization described in Chapter 4.

While our approach is quite general, the specific design and performance impacts of microscopic device physics are expected to vary greatly between different devices and material systems. For example, it is known that photon management is important in order to realize high efficiency in GaAs solar cells [9, 10]. In such devices, the challenge is not necessarily primary photon absorption. Instead, photon recycling

(the reuse of photons generated from band-to-band recombination) becomes an important process. This will change the governing design principles as the optical design problem no longer focuses on broadband absorption of the solar spectrum, but instead on internal light trapping of spontaneously emitted photons of near band-edge wavelengths. Although device-specific design principles can be suggested for the cells considered in this thesis, we stress that it is the design approach accounting for the full structure and physics of a device, as opposed to system-specific conclusions, which should be implemented to optimize other systems.

There remains significant opportunity to continue the development of more advanced models which would take into account other aspects of cell manufacturing and system performance. For example, in Section 4.5.2 we consider the location of a geometry induced defect for which we assume properties based on experimental observations. However, a more powerful next-generation model would begin by predicting the location and electrical properties of the defect based on the physics and chemistry of material deposition. The resulting structure could then be coupled into optoelectronic simulations such as those described in Chapter 4, yielding a full predictive tool for optimizing not only design, but also cell processing.

Comprehensive modeling is also applicable at the module and system levels. A photovoltaic system consists of many cells operating in many modules under varying environmental conditions for at least two to three decades. Since the ultimate goal of the technology is energy generation, the performance of the system should be the ultimate goal of a comprehensive photovoltaic model. While work has been done to model and understand system performance [135], there is still ample opportunity to connect such approaches back down to the microscopic device physics at the cell level. For example, a microscopic understanding of degradation in thin-film CdTe solar cells [136] could be used to predict how the J-V curves of individual cells will change over time. This could then be fed into a system-level model for performance of the entire array including the behavior of the supporting power electronics. Such an approach could lead to more reliable and robust arrays.

Photovoltaics, and energy-conversion technologies in general, rely on the use of

multiple physical mechanisms working in tandem to convert raw energy resources into electricity or other useful forms. Understanding and considering these mechanisms and their interactions enables powerful co-optimization that will be critical for the efficiency and thus competitiveness of future generations of energy technologies.

Appendix A

Convergence in numerical simulations

The numerical simulation methods implemented in this thesis rely on discretization of the modeled geometry on a simulation mesh or grid. When working with such methods it is important to ensure that the choice of simulation grid does not affect the results of the simulation. Here, we present an example illustrating the importance of this.

Figure A.1, shows the short circuit current calculated for a pyramidally structured SHJ cell, such as those considered in Section 3.4. The FDTD portion of the simulation was carried out with two different simulation tools, Lumerical FDTD Solutions, and Synopsys Sentaurus TCAD. The number of mesh points per simulated wavelength (in the material) was changed in both software tools, and the J_{sc} resulting from subsequent electrical simulation is plotted in Figure 3.4. While this parameter is directly addressable in the Sentaurus implementation, it is modified through the “mesh accuracy” parameter in the Lumerical package. It should be noted that both tools use different mesh generation algorithms, but that the number of points per wavelength is one of the most important parameters for an FDTD simulation mesh. Common wisdom is that 10 points per wavelength offers a reasonable compromise between accuracy and computational demand, and is a good starting point when optimizing a simulation mesh.

The results shown in Figure A.1 indicate that the Lumerical FDTD tool provides a more stable result for this particular simulation. We note that it is possible that

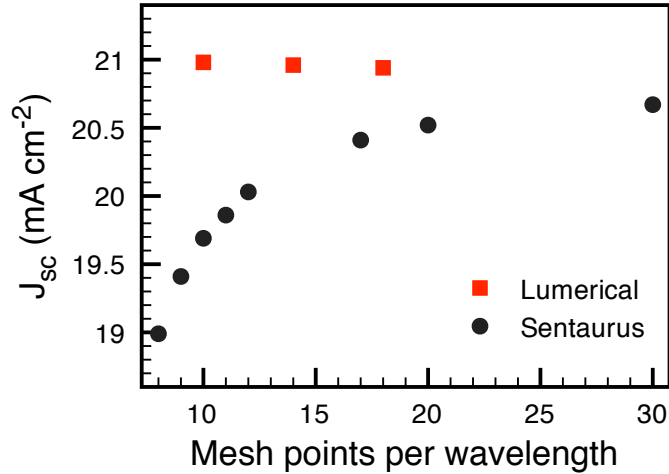


Figure A.1. The short circuit current calculated from optoelectronic simulations of the solar cells described in Section 3.4 with $B = 6 \mu\text{m}$ and $P = 1 \mu\text{m}$, for two different software tools used for the optical portion of the simulation. The results are plotted against the number of mesh points used per wavelength in the optical simulation to show the importance of verifying that simulation results are not sensitive to specific discretization of the modeled structure.

further optimization of the Sentaurus calculation parameters would yield a stable result as well. However, this serves as an example of the importance of verifying that simulation results are physical, and not heavily influenced by artifacts of the numerical simulation or the discretization of the structure. Mesh generation algorithms for both electrical and optical simulation can be complex, and some trial and error is generally required to find a suitable simulation grid. Computational demand can generally be reduced by applying a more refined mesh only to regions or features of interest. It is also important that the mesh be fine at interfaces or other regions where the modeled currents, fields, or carrier concentrations change rapidly.

Bibliography

- [1] W. A. Hermann. Quantifying global exergy resources. *Energy*, 31(12):1685–1702, 2006.
- [2] N. Lewis and D. Nocera. Powering the planet: Chemical challenges in solar energy utilization. *Proceedings of the National Academy of Sciences*, 103(43):15729–15735, 2006.
- [3] M. Hoffert, K. Caldeira, A. Jain, E. Haites, S. Potter, M. Schlesinger, S. Schneider, R. Watts, T. Wigley, and D. Wuebbles. Energy implications of future stabilization of atmospheric CO₂ content. *Nature*, 395(6705):881–884, 1998.
- [4] D. M. Powell, M. T. Winkler, H. J. Choi, C. B. Simmons, D. B. Needleman, and T. Buonassisi. Crystalline silicon photovoltaics: a cost analysis framework for determining technology pathways to reach baseload electricity costs. *Energy Environ. Sci.*, 5:5874–5883, 2012.
- [5] J. Nelson. *The physics of solar cells*. Imperial College Press, London, 2003.
- [6] ASTM G173-03(2012) standard tables for reference solar spectral irradiances: Direct normal and hemispherical on 37° tilted surface. Technical report, ASTM International, 2012.
- [7] W. Shockley and H. J. Queisser. Detailed balance limit of efficiency of p-n junction solar cells. *Journal of Applied Physics*, 32(3):510–519, 1961.
- [8] P. Wurfel. The chemical-potential of radiation. *Journal of Physics C – Solid State Physics*, 15(18):3967–3985, 1982.

- [9] B. Kayes, H. Nie, R. Twist, S. Spruytte, F. Reinhardt, I. Kizilyalli, and G. Higashi. 27.6% conversion efficiency, a new record for single-junction solar cells under 1 sun illumination. In *Photovoltaic Specialists Conference (PVSC), 2011 37th IEEE*, pp. 000004–000008, June 2011.
- [10] O. D. Miller, E. Yablonovitch, and S. R. Kurtz. Strong internal and external luminescence as solar cells approach the Shockley Queisser limit. *IEEE Journal of Photovoltaics*, 2(3):303–311, 2012.
- [11] M. A. Green. Limits on the open-circuit voltage and efficiency of silicon solar cells imposed by intrinsic Auger processes. *IEEE Transactions on Electron Devices*, 31(5): 671–678, 1984.
- [12] F. Pedrotti and L. Pedrotti. *Introduction to optics*. Prentice Hall, 2nd edition, 1993.
- [13] S. Sze and K. Ng. *Physics of semiconductor devices*. Wiley-Interscience, Hoboken, New Jersey, 2007.
- [14] R. F. Pierret. *Advanced semiconductor fundamentals*. Pearson Education, 2 edition, 2003.
- [15] M. A. Green. Limiting efficiency of bulk and thin-film silicon solar cells in the presence of surface recombination. *Progress in Photovoltaics: Research and Applications*, 7(4): 327–330, 1999.
- [16] R. B. Bergmann. Crystalline Si thin-film solar cells: A review. *Applied Physics A: Materials Science and Processing*, 69(2):187–194, 1999.
- [17] M. Mason, C. Richardson, H. Atwater, and R. Ahrenkiel. Microsecond minority carrier lifetimes in HWCVD-grown films and implications for thin film solar cells. *Thin Solid Films*, 501(1–2):288–290, 2006.
- [18] M. S. Mason. *Synthesis of Large-Grained Polycrystalline Silicon by Hot-Wire Chemical Vapor Deposition for Thin Film Photovoltaic Applications*. PhD thesis, California Institute of Technology, January 2004.

- [19] H. M. Branz, C. W. Teplin, M. J. Romero, I. T. Martin, Q. Wang, K. Alberi, D. L. Young, and P. Stradins. Hot-wire chemical vapor deposition of epitaxial film crystal silicon for photovoltaics. *Thin Solid Films*, 519(14):4545–4550, 2011.
- [20] K. S. Langeland. *Thin-Film Silicon Photovoltaics: Characterization of Thin-Film Deposition and Analysis of Enhanced Light Trapping from Scattering Nanoparticle Arrays*. PhD thesis, California Institute of Technology, February 2012.
- [21] C. E. Richardson. *Low-Temperature Hot-Wire Chemical Vapor Deposition of Epitaxial Films for Large-Grained Polycrystalline Photovoltaic Devices*. PhD thesis, California Institute of Technology, June 2006.
- [22] S. Grover, C. W. Teplin, J. V. Li, D. C. Bobela, J. Bornstein, P. Schroeter, S. Johnston, H. Guthrey, P. Stradins, H. M. Branz, and D. L. Young. Device physics of heteroepitaxial film c-Si heterojunction solar cells. *IEEE Journal of Photovoltaics*, 3(1):230–235, 2013.
- [23] C. W. Teplin, B. G. Lee, T. R. Fanning, J. Wang, S. Grover, F. Hasoon, R. Bauer, J. Bornstein, P. Schroeter, and H. M. Branz. Pyramidal light trapping and hydrogen passivation for high-efficiency heteroepitaxial (100) crystal silicon solar cells. *Energy Environ. Sci.*, 5:8193–8198, 2012.
- [24] J. H. Werner, R. Dassow, T. J. Rinke, J. R. Khler, and R. B. Bergmann. From polycrystalline to single crystalline silicon on glass. *Thin Solid Films*, 383(1–2):95–100, 2001.
- [25] P. P. Altermatt and G. Heiser. Predicted electronic properties of polycrystalline silicon from three-dimensional device modeling combined with defect-pool model. *Journal of Applied Physics*, 92(5):2561–2574, 2002.
- [26] S. A. Edmiston, G. Heiser, A. B. Sproul, and M. A. Green. Improved modeling of grain boundary recombination in bulk and p-n junction regions of polycrystalline silicon solar cells. *Journal of Applied Physics*, 80(12):6783–6795, 1996.
- [27] E. Christoffel, M. Rusu, A. Zerga, S. Bourdais, S. Noel, and A. Slaoui. A two-dimensional modeling of the fine-grained polycrystalline silicon thin-film solar cells. *Thin Solid Films*, 403:258–262, 2002.

- [28] T. Fujisaki, A. Yamada, and M. Konagai. Effects of grain boundaries on cell performance of poly-silicon thin film solar cells by 2-D simulation. *Solar Energy Materials and Solar Cells*, 74(1–4):331–337, 2002.
- [29] H. Takakura and Y. Hamakawa. Device simulation and modeling of microcrystalline silicon solar cells. *Solar Energy Materials and Solar Cells*, 74(1–4):479–487, 2002.
- [30] K.-i. Kurobe, Y. Ishikawa, Y. Yamamoto, T. Fuyuki, and H. Matsunami. Effects of grain boundaries in polycrystalline silicon thin-film solar cells based on the two-dimensional model. *Solar Energy Materials and Solar Cells*, 65(1–4):201–209, 2001.
- [31] M. G. Deceglie, M. D. Kelzenberg, and H. A. Atwater. Effects of bulk and grain boundary recombination on the efficiency of columnar-grained crystalline silicon film solar cells. In *35th IEEE Photovoltaic Specialists Conference (PVSC)*, pp. 001487–001490, 2010.
- [32] G. Masetti, M. Severi, and S. Solmi. Modeling of carrier mobility against carrier concentration in arsenic-, phosphorus-, and boron-doped silicon. *IEEE Transactions on Electron Devices*, 30(7):764–769, 1983.
- [33] TCAD Sentaurus, <http://www.synopsys.com>.
- [34] R. E. I. Schropp and M. Zeman. *Amorphous and microcrystalline silicon solar cells: modeling, materials and device technology*. Kluwer Academic Publishers, Norwell, Massachusetts, 1998.
- [35] A. Matsuda. Microcrystalline silicon. Growth and device application. *Journal of Non-Crystalline Solids*, 338–340:1–12, 2004.
- [36] M. Luysberg, P. Hapke, R. Carius, and F. Finger. Structure and growth of hydrogenated microcrystalline silicon: Investigation by transmission electron microscopy and Raman spectroscopy of films grown at different plasma excitation frequencies. *Philosophical Magazine A*, 75(1):31–47, 1997.
- [37] S. Klein, T. Repmann, and T. Brammer. Microcrystalline silicon films and solar cells deposited by PECVD and HWCVD. *Solar Energy*, 77(6):893–908, 2004.

- [38] J. Thiesen, E. Iwaniczko, K. M. Jones, A. Mahan, and R. Crandall. Growth of epitaxial silicon at low temperatures using hot-wire chemical vapor deposition. *Applied Physics Letters*, 75(7):992–994, 1999.
- [39] M. S. Mason, C. M. Chen, and H. A. Atwater. Hot-wire chemical vapor deposition for grained polycrystalline epitaxial silicon growth on large-silicon templates. *Thin Solid Films*, 430(1-2):54–57, 2003.
- [40] M. Tao and L. P. Hunt. Crystal growth in silicon chemical vapor deposition from silane. *Journal of The Electrochemical Society*, 144(6):2221–2225, 1997.
- [41] A. Gallagher. Some physics and chemistry of hot-wire deposition. *Thin Solid Films*, 395(1–2):25–28, 2001.
- [42] C. E. Richardson, M. Mason, and H. A. Atwater. Hot-wire CVD-grown epitaxial Si films on Si (100) substrates and a model of epitaxial breakdown. *Thin Solid Films*, 501(1–2):332–334, 2006.
- [43] J. K. Holt. *Hot-Wire Chemical Vapor Deposition of Silicon and Silicon Nitride for Photovoltaics: Experiments, Simulations, and Applications*. PhD thesis, California Institute of Technology, 2003.
- [44] J. K. Holt, M. Swiatek, D. G. Goodwin, R. P. Muller, W. A. Goddard, III, and H. A. Atwater. Gas phase and surface kinetic processes in polycrystalline silicon hot-wire chemical vapor deposition. *Thin Solid Films*, 395(1–2):29–35, 2001.
- [45] O. P. Karpenko, S. M. Yalisove, and D. J. Eaglesham. Surface roughening during low temperature Si(100) epitaxy. *Journal of Applied Physics*, 82(3):1157–1165, 1997.
- [46] D. K. Schroder. *Semiconductor Material and Device Characterization*. Wiley-Interscience, 3rd edition, 2006.
- [47] M. Schottler and M. J. d. Wild-Scholten. Carbon footprint of PECVD chamber cleaning. *Photovoltaic International*, 2:64–69, 2008.
- [48] W. G. van Sark, L. Korte, and F. Roca, editors. *Physics and technology of amorphous-crystalline heterostructure silicon solar cells*. Springer, 2012.

- [49] C. Ballif, L. Barraud, A. Descoedres, Z. Holman, S. Morel, and S. De Wolf. a-Si:h/c-Si heterojunctions: a future mainstream technology for high-efficiency crystalline silicon solar cells? In *38th IEEE Photovoltaic Specialists Conference (PVSC)*, pp. 001705–001709, 2012.
- [50] M. Tanaka, M. Taguchi, T. Matsuyama, T. Sawada, S. Tsuda, S. Nakano, H. Hanafusa, and Y. Kuwano. Development of new a-Si/c-Si heterojunction solar cells: ACJ-HIT (artificially constructed junction-heterojunction with intrinsic thin-layer). *Japanese Journal of Applied Physics*, 31:3518–3522, 1992.
- [51] T. Mishima, M. Taguchi, H. Sakata, and E. Maruyama. Development status of high-efficiency HIT solar cells. *Solar Energy Materials and Solar Cells*, 95(1):18–21, 2011.
- [52] M. Taguchi, A. Terakawa, E. Maruyama, and M. Tanaka. Obtaining a higher V_{oc} in HIT cells. *Progress in Photovoltaics: Research and Applications*, 13(6):481–488, 2005.
- [53] O. A. Maslova, J. Alvarez, E. V. Gushina, W. Favre, M. E. Gueunier-Farret, A. S. Gudovskikh, A. V. Ankudinov, E. I. Terukov, and J. P. Kleider. Observation by conductive-probe atomic force microscopy of strongly inverted surface layers at the hydrogenated amorphous silicon/crystalline silicon heterojunctions. *Applied Physics Letters*, 97(25):252110, 2010.
- [54] J. P. Kleider, J. Alvarez, A. V. Ankudinov, A. S. Gudovskikh, E. V. Gushina, M. Labrune, O. A. Maslova, W. Favre, M. E. Gueunier-Farret, P. R. I. Cabarrocas, and E. I. Terukov. Characterization of silicon heterojunctions for solar cells. *Nanoscale Research Letters*, 6:152, 2011.
- [55] J. V. Li, R. S. Crandall, D. L. Young, M. R. Page, E. Iwaniczko, and Q. Wang. Capacitance study of inversion at the amorphous-crystalline interface of n-type silicon heterojunction solar cells. *Journal of Applied Physics*, 110(11):114502, 2011.
- [56] J. Kleider, Y. Soro, R. Chouffot, A. Gudovskikh, P. R. i Cabarrocas, J. Damon-Lacoste, D. Eon, and P.-J. Ribeyron. High interfacial conductivity at amorphous silicon/crystalline silicon heterojunctions. *Journal of Non-Crystalline Solids*, 354: 2641–2645, 2008.

- [57] J. P. Kleider, A. S. Gudovskikh, and P. R. i Cabarrocas. Determination of the conduction band offset between hydrogenated amorphous silicon and crystalline silicon from surface inversion layer conductance measurements. *Applied Physics Letters*, 92(16):162101, 2008.
- [58] W. Favre, M. Labrune, F. Dadouche, A. S. Gudovskikh, P. R. i. Cabarrocas, and J. P. Kleider. Study of the interfacial properties of amorphous silicon/n-type crystalline silicon heterojunction through static planar conductance measurements. *Physica Status Solidi (C)*, 7(3-4):1037–1040, 2010.
- [59] R. Varache, W. Favre, L. Korte, and J. Kleider. Influence of the amorphous/crystalline silicon heterostructure properties on planar conductance measurements. *Journal of Non-Crystalline Solids*, 358(17):2236–2240, 2012.
- [60] K. Ghosh, C. Tracy, and S. Bowden. Experimental and theoretical verification of the presence of inversion region in a-Si/c-Si heterojunction solar cells with an intrinsic layer. In *38th IEEE Photovoltaic Specialists Conference (PVSC)*, pp. 001046–001048, 2012.
- [61] D. Diouf, J.-P. Kleider, and C. Longeaud. Two-dimensional simulations of interdigitated back contact silicon heterojunctions solar cells. In W. Sark, L. Korte, and F. Roca, editors, *Physics and Technology of Amorphous-Crystalline Heterostructure Silicon Solar Cells*, pp. 483–519. Springer, 2011.
- [62] M. Lu, S. Bowden, U. Das, and R. Birkmire. Interdigitated back contact silicon heterojunction solar cell and the effect of front surface passivation. *Applied Physics Letters*, 91(6):063507, 2007.
- [63] R. Stangl, J. Haschke, M. Bivour, L. Korte, M. Schmidt, K. Lips, and B. Rech. Planar rear emitter back contact silicon heterojunction solar cells. *Solar Energy Materials and Solar Cells*, 93(10):1900–1903, 2009.
- [64] M. Lu, U. Das, S. Bowden, S. Hegedus, and R. Birkmire. Optimization of interdigitated back contact silicon heterojunction solar cells: tailoring hetero-interface band structures while maintaining surface passivation. *Progress in Photovoltaics: Research and Applications*, 19(3):326–338, 2011.

- [65] T. Desrues, S. De Vecchi, F. Souche, D. Diouf, D. Munoz, M. Gueunier-Farret, J.-P. Kleider, and P.-J. Ribeyron. Development of interdigitated back contact silicon heterojunction (IBC Si-HJ) solar cells. *Energy Procedia*, 8(0):1876–6102, 2011.
- [66] N. Mingirulli, J. Haschke, R. Gogolin, R. Ferré, T. F. Schulze, J. Düsterhöft, N.-P. Harder, L. Korte, R. Brendel, and B. Rech. Efficient interdigitated back-contacted silicon heterojunction solar cells. *Physica Status Solidi (RRL) - Rapid Research Letters*, 5(4):159–161, 2011.
- [67] A. Froitzheim, K. Brendel, L. Elstner, W. Fuhs, K. Kliefoth, and M. Schmidt. Interface recombination in heterojunctions of amorphous and crystalline silicon. *Journal of Non-Crystalline Solids*, 299–302(Part 1):663–667, 2002.
- [68] A. Kanevce and W. K. Metzger. The role of amorphous silicon and tunneling in heterojunction with intrinsic thin layer (HIT) solar cells. *Journal of Applied Physics*, 105(9):094507, 2009.
- [69] M. Nath, P. Chatterjee, J. Damon-Lacoste, and P. Roca i Cabarrocas. Criteria for improved a-Si:H(n)/c-Si(p) front heterojunction with intrinsic thin layer solar cells. *Journal of Applied Physics*, 103(3):034506–034506–9, 2008.
- [70] T. Wang, E. Iwaniczko, M. Page, D. Levi, Y. Yan, H. Branz, and Q. Wang. Effect of emitter deposition temperature on surface passivation in hot-wire chemical vapor deposited silicon heterojunction solar cells. *Thin Solid Films*, 501(1–2):284–287, 2006.
- [71] T. H. Wang, E. Iwaniczko, M. R. Page, D. H. Levi, Y. Yan, V. Yelundur, H. M. Branz, A. Rohatgi, and Q. Wang. Effective interfaces in silicon heterojunction solar cells. In *31st IEEE Photovoltaic Specialists Conference (PVSC)*, pp. 955–958, 2005.
- [72] K.-s. Ji, J. Choi, H. Yang, H.-M. Lee, and D. Kim. A study of crystallinity in amorphous Si thin films for silicon heterojunction solar cells. *Solar Energy Materials and Solar Cells*, 95(1):203–206, 2011.
- [73] S. De Wolf and M. Kondo. Abruptness of a-Si:Hc-Si interface revealed by carrier lifetime measurements. *Applied Physics Letters*, 90(4):042111, 2007.

- [74] M. G. Deceglie and H. A. Atwater. Effect of defect-rich epitaxy on crystalline silicon / amorphous silicon heterojunction solar cells and the use of low-mobility layers to improve performance. In *37th IEEE Photovoltaic Specialists Conference (PVSC)*, pp. 001417–001420, 2011.
- [75] M. Jeong, P. Solomon, S. Laux, H.-S. Wong, and D. Chidambarrao. Comparison of raised and Schottky source/drain MOSFETs using a novel tunneling contact model. In *Electron Devices Meeting, 1998. IEDM '98. Technical Digest., International*, volume 733–736, 1998.
- [76] U. Rau, P. O. Grabitz, and J. H. Werner. Resistive limitations to spatially inhomogeneous electronic losses in solar cells. *Applied Physics Letters*, 85(24):6010, 2004.
- [77] M. Despeisse, G. Bugnon, A. Feltrin, M. Stueckelberger, P. Cuony, F. Meillaud, A. Billet, and C. Ballif. Resistive interlayer for improved performance of thin film silicon solar cells on highly textured substrate. *Applied Physics Letters*, 96(7):073507, 2010.
- [78] P. Cuony, M. Marending, D. T. L. Alexander, M. Boccard, G. Bugnon, M. Despeisse, and C. Ballif. Mixed-phase p-type silicon oxide containing silicon nanocrystals and its role in thin-film silicon solar cells. *Applied Physics Letters*, 97(21):213502, 2010.
- [79] K. Ghosh, S. Bowden, and C. Tracy. Role of hot carriers in the interfacial transport in amorphous silicon/crystalline silicon heterostructure solar cells. *Physica Status Solidi (A)*, 2012.
- [80] R. S. Crandall, E. Iwaniczko, J. V. Li, and M. R. Page. A comprehensive study of hole collection in heterojunction solar cells. *Journal of Applied Physics*, 112(9):093713, 2012.
- [81] A. Descoedres, L. Barraud, S. De Wolf, B. Strahm, D. Lachenal, C. Guerin, Z. C. Holman, F. Zicarelli, B. Demareux, J. Seif, J. Holovsky, and C. Ballif. Improved amorphous/crystalline silicon interface passivation by hydrogen plasma treatment. *Applied Physics Letters*, 99(12):123506, 2011.

- [82] A. Descoedres, Z. Holman, L. Barraud, S. Morel, S. De Wolf, and C. Ballif. >21% efficient silicon heterojunction solar cells on n- and p-type wafers compared. *IEEE Journal of Photovoltaics*, 3(1):83–89, 2013.
- [83] Z. C. Holman, M. Filipic, A. Descoedres, S. De Wolf, F. Smole, M. Topic, and C. Ballif. Infrared light management in high-efficiency silicon heterojunction and rear-passivated solar cells. *Journal of Applied Physics*, 113(1):013107, 2013.
- [84] J. Ziegler and J. Biersack. SRIM—2008, stopping power and range of ions in matter. 2008.
- [85] M. G. Deceglie, H. S. Emmer, Z. C. Holman, A. Descoedres, S. D. Wolf, C. Ballif, and H. A. Atwater. Scanning laser-beam-induced current measurements of lateral transport near junction defects in silicon heterojunction solar cells. *IEEE Journal of Photovoltaics*, 4(1):154–159, 2014.
- [86] M. A. Green and M. J. Keevers. Optical properties of intrinsic silicon at 300 K. *Progress in Photovoltaics: Research and Applications*, 3(3):189–192, 1995.
- [87] FDTD solutions, <http://www.lumerical.com>.
- [88] M. D. Kelzenberg. *Silicon Microwire Photovoltaics*. PhD thesis, California Institute of Technology, 2010.
- [89] R. Hall. Silicon photovoltaic cells. *Solid-State Electronics*, 24(7):595–616, 1981.
- [90] V. E. Ferry, J. N. Munday, and H. A. Atwater. Design considerations for plasmonic photovoltaics. *Adv Mater*, 22(43):4794–808, 2010.
- [91] V. E. Ferry, M. A. Verschuuren, H. B. T. Li, E. Verhagen, R. J. Walters, R. E. I. Schropp, H. A. Atwater, and A. Polman. Light trapping in ultrathin plasmonic solar cells. *Optics Express*, 18(S2):A237–A245, 2010.
- [92] A. V. Shah, H. Schade, M. Vanecek, J. Meier, E. Vallat-Sauvain, N. Wyrsh, U. Kroll, C. Droz, and J. Bailat. Thin-film silicon solar cell technology. *Progress in Photovoltaics: Research and Applications*, 12(23):113–142, 2004.

- [93] H. A. Atwater and A. Polman. Plasmonics for improved photovoltaic devices. *Nat Mater*, 9(3):205–213, 2010.
- [94] J. Müller, B. Rech, J. Springer, and M. Vanecek. TCO and light trapping in silicon thin film solar cells. *Solar Energy*, 77(6):917–930, 2004.
- [95] C. Rockstuhl, S. Fahr, K. Bittkau, T. Beckers, R. Carius, F. J. Haug, T. Söderström, C. Ballif, and F. Lederer. Comparison and optimization of randomly textured surfaces in thin-film solar cells. *Opt. Express*, 18(S3):A335–A341, 2010.
- [96] V. E. Ferry, A. Polman, and H. A. Atwater. Modeling light trapping in nanostructured solar cells. *ACS Nano*, 5(12):10055–10064, 2011.
- [97] M. D. Kelzenberg, M. C. Putnam, D. B. Turner-Evans, N. S. Lewis, and H. A. Atwater. Predicted efficiency of Si wire array solar cells. In *Proceeding of the 34th IEEE Photovoltaics Specialists Conference (PVSC)*, pp. 001948–001953, 2009.
- [98] X. Li, N. P. Hylton, V. Giannini, K.-H. Lee, N. J. Ekins-Daukes, and S. A. Maier. Bridging electromagnetic and carrier transport calculations for three-dimensional modelling of plasmonic solar cells. *Opt. Express*, 19(S4):A888–A896, 2011.
- [99] F. J. Haug, T. Söderström, O. Cubero, V. Terrazzoni-Daudrix, and C. Ballif. Influence of the ZnO buffer on the guided mode structure in Si/ZnO/Ag multilayers. *Journal of Applied Physics*, 106(4):044502, 2009.
- [100] E. Palik and G. Ghosh. *Handbook of optical constants of solids*, volume 3. Academic Press, New York, 1997.
- [101] A. D. Rakic, A. B. Djurišić, J. M. Elazar, and M. L. Majewski. Optical properties of metallic films for vertical-cavity optoelectronic devices. *Appl. Opt.*, 37(22):5271–5283, 1998.
- [102] J. Grandidier, R. A. Weitekamp, M. G. Deceglie, D. M. Callahan, C. Battaglia, C. R. Bukowsky, C. Ballif, R. H. Grubbs, and H. A. Atwater. Solar cell efficiency enhancement via light trapping in printable resonant dielectric nanosphere arrays. *Physica Status Solidi (A)*, 210:255–260, 2012.

- [103] J. Grandidier, D. M. Callahan, J. N. Munday, and H. A. Atwater. Light absorption enhancement in thin-film solar cells using whispering gallery modes in dielectric nanospheres. *Adv Mater*, 23(10):1272–1276, 2011.
- [104] J. Grandidier, M. G. Deceglie, D. M. Callahan, and H. A. Atwater. Simulations of solar cell absorption enhancement using resonant modes of a nanosphere array. *Journal of Photonics for Energy*, 2(1):024502–1–024502–11, 2012.
- [105] O. S. Heavens. *Optical properties of thin solid films*. General Publishing Company, Toronto, 1991.
- [106] R. A. Pala, J. White, E. Barnard, J. Liu, and M. L. Brongersma. Design of plasmonic thin-film solar cells with broadband absorption enhancements. *Advanced Materials*, 21(34):3504–3509, 2009.
- [107] J. Bhattacharya, N. Chakravarty, S. Pattnaik, W. Dennis Slafer, R. Biswas, and V. L. Dalal. A photonic-plasmonic structure for enhancing light absorption in thin film solar cells. *Applied Physics Letters*, 99(13):131114, 2011.
- [108] C. Battaglia, C.-M. Hsu, K. Söderström, J. Escarré, F.-J. Haug, M. Charrière, M. Boccard, M. Despeisse, D. T. L. Alexander, M. Cantoni, Y. Cui, and C. Ballif. Light trapping in solar cells: Can periodic beat random? *ACS Nano*, 6(3):2790–2797, 2012.
- [109] E. A. Schiff. Thermodynamic limit to photonic-plasmonic light-trapping in thin films on metals. *Journal of Applied Physics*, 110(10):104501, 2011.
- [110] Z. F. Yu, A. Raman, and S. H. Fan. Fundamental limit of nanophotonic light trapping in solar cells. *Proceedings of the National Academy of Sciences of the United States of America*, 107(41):17491–17496, 2010.
- [111] F. J. Beck, S. Mookapati, A. Polman, and K. R. Catchpole. Asymmetry in photocurrent enhancement by plasmonic nanoparticle arrays located on the front or on the rear of solar cells. *Applied Physics Letters*, 96(3):033113, 2010.

- [112] M. G. Deceglie, V. E. Ferry, A. P. Alivisatos, and H. A. Atwater. Design of nanostructured solar cells using coupled optical and electrical modeling. *Nano Lett*, 12(6):2894–2900, 2012.
- [113] V. E. Ferry, M. A. Verschuuren, M. C. v. Lare, R. E. I. Schropp, H. A. Atwater, and A. Polman. Optimized spatial correlations for broadband light trapping nanopatterns in high efficiency ultrathin film a-Si:H solar cells. *Nano Letters*, 11(10):4239–4245, 2011.
- [114] R. M. Swanson, S. K. Beckwith, R. A. Crane, W. D. Eades, K. Young Hoon, R. A. Sinton, and S. E. Swirhun. Point-contact silicon solar cells. *IEEE Transactions on Electron Devices*, 31(5):661–664, 1984.
- [115] B. M. Kayes, H. A. Atwater, and N. S. Lewis. Comparison of the device physics principles of planar and radial p-n junction nanorod solar cells. *Journal of Applied Physics*, 97(11):114302, 2005.
- [116] S. W. Boettcher, J. M. Spurgeon, M. C. Putnam, E. L. Warren, D. B. Turner-Evans, M. D. Kelzenberg, J. R. Maiolo, H. A. Atwater, and N. S. Lewis. Energy-conversion properties of vapor-liquid-solid-grown silicon wire-array photocathodes. *Science*, 327(5962):185–187, 2010.
- [117] H. Sakai, T. Yoshida, T. Hama, and Y. Ichikawa. Effects of surface morphology of transparent electrode on the open-circuit voltage in a-Si:H solar cells. *Japanese Journal of Applied Physics*, 29:630–635, 1990.
- [118] H. B. T. Li, R. H. Franken, J. K. Rath, and R. E. I. Schropp. Structural defects caused by a rough substrate and their influence on the performance of hydrogenated nano-crystalline silicon n-i-p solar cells. *Solar Energy Materials and Solar Cells*, 93(3):338–349, 2009.
- [119] P. Spinelli, M. A. Verschuuren, and A. Polman. Broadband omnidirectional antireflection coating based on subwavelength surface Mie resonators. *Nat Commun*, 3:692, 2012.

- [120] P. Spinelli, M. Hebbink, R. de Waele, L. Black, F. Lenzmann, and A. Polman. Optical impedance matching using coupled plasmonic nanoparticle arrays. *Nano Lett*, 11(4):1760–1765, 2011.
- [121] J. Zhu, C.-M. Hsu, Z. Yu, S. Fan, and Y. Cui. Nanodome solar cells with efficient light management and self-cleaning. *Nano Letters*, 10(6):1979–1984, 2010.
- [122] C.-M. Hsu, C. Battaglia, C. Pahud, Z. Ruan, F.-J. Haug, S. Fan, C. Ballif, and Y. Cui. High-efficiency amorphous silicon solar cell on a periodic nanocone back reflector. *Advanced Energy Materials*, pp. 628–633, 2012.
- [123] Y. Nasuno, M. Kondo, and A. Matsuda. Effects of substrate surface morphology on microcrystalline silicon solar cells. *Japanese Journal of Applied Physics*, 40:L303, 2001.
- [124] S. Guha, J. Yang, S. J. Jones, Y. Chen, and D. L. Williamson. Effect of microvoids on initial and light-degraded efficiencies of hydrogenated amorphous silicon alloy solar cells. *Applied Physics Letters*, 61:1444–1446, 1992.
- [125] M. G. Deceglie, V. E. Ferry, A. P. Alivisatos, and H. A. Atwater. Accounting for material quality in the optoelectronic design of thin-film solar cells. *IEEE Journal of Photovoltaics*, 3(2):599–604, 2013.
- [126] AMPS, <http://www.ampsmodeling.org>.
- [127] PC1D, <http://www.pv.unsw.edu.au/info-about/our-school/products-services/pc1d>.
- [128] AFORS-HET, http://www.helmholtz-berlin.de/forschung/enma/si-pv/projekte/asicsi/afors-het/index_en.html.
- [129] SCAPS, <http://users.elis.ugent.be/ELISgroups/solar/projects/scaps.html>.
- [130] ASA, <http://www.ewi.tudelft.nl/en/the-faculty/departments/electrical-sustainable-energy/photovoltaic-materials-and-devices/asa-software/>.
- [131] M. G. Walter, E. L. Warren, J. R. McKone, S. W. Boettcher, Q. Mi, E. A. Santori, and N. S. Lewis. Solar water splitting cells. *Chemical Reviews*, 110(11):6446–6473, 2010.

- [132] R. C. Rossi and N. S. Lewis. Investigation of the size-scaling behavior of spatially nonuniform barrier height contacts to semiconductor surfaces using ordered nanometer-scale nickel arrays on silicon electrodes. *The Journal of Physical Chemistry B*, 105(49):12303–12318, 2001.
- [133] E. L. Warren. *Silicon Microwire Arrays for Photoelectrochemical and Photovoltaic Applications*. PhD thesis, California Institute of Technology, 2012.
- [134] S. Haussener, C. Xiang, J. M. Spurgeon, S. Ardo, N. S. Lewis, and A. Z. Weber. Modeling, simulation, and design criteria for photoelectrochemical water-splitting systems. *Energy Environ. Sci.*, 5:9922–9935, 2012.
- [135] S. MacAlpine, C. Deline, R. Erickson, and M. Brandemuehl. Module mismatch loss and recoverable power in unshaded PV installations. In *38th IEEE Photovoltaic Specialists Conference (PVSC)*, pp. 001388–001392, June 2012.
- [136] K. D. Dobson, I. Visoly-Fisher, G. Hodes, and D. Cahen. Stability of CdTe/CdS thin-film solar cells. *Solar Energy Materials and Solar Cells*, 62(3):295–325, 2000.